THESIS FOR THE DEGREE OF DOCTOR OF PHILOSOPHY

# Corrosion of High-Temperature Alloys in Molten Salts

ESRAA HAMDY MOHAMEDIN

Department of Chemistry and Chemical Engineering

CHALMERS UNIVERSITY OF TECHNOLOGY

Gothenburg, Sweden 2023

Corrosion of High-Temperature Alloys in Molten Salts

ESRAA HAMDY MOHAMEDIN
ISBN 978-91-7905-827-2

© ESRAA HAMDY MOHAMEDIN, 2023.

Doktorsavhandlingar vid Chalmers tekniska högskola
Ny serie nr 5293
ISSN 0346-718X

Department of Chemistry and Chemical Engineering
Chalmers University of Technology
SE-412 96 Gothenburg
Sweden
Telephone + 46 (0)31-772 1000

Cover:
*Top left*: A schematic illustrates the components of a concentrated solar power plant [Ref 15]. *Top right*; A schematic illustration of a hot storage tank and sections of interest. *Bottom left*; XRD patterns of Kanthal® EF 101 before and after exposure to alkali carbonate melt at 800°C, and α- and γ-$LiAlO_2$ thicknesses for the four ferritic FeCrAl alloys. *Bottom centre*: Assembly of top-view and cross-section SEM images of Kanthal® EF 101 after exposure to alkali carbonate melt at 800°C. *Bottom right*; polyhedral visualisation of α- and γ-$LiAlO_2$ crystal structures.

Chalmers Digitaltryck
Gothenburg, Sweden 2023

# Corrosion of High-Temperature Alloys in Molten Salts

Esraa Hamdy Mohamedin
Department of Chemistry and Chemical Engineering
Chalmers University of Technology

## Abstract

Concentrated solar power (CSP) is an interesting technology that involves storing solar energy in the form of heat and subsequently converting it into electricity. The third-generation (Gen3) CSP plants aim to operate at temperatures >700°C, necessitating the deployment of new heat storage materials that can withstand such high operating temperatures. Molten carbonate and chloride salt mixtures are promising candidates for Gen3-CSP plants. Nevertheless, the use of such melts poses a serious corrosion challenge for the metallic materials that contain them.

The work of this thesis focuses on the behaviours of selected high-temperature alloys that are in direct or indirect contact with salt melts. A special experimental set-up was established to mimic hot thermal energy storage (TES) tank conditions. Salt melts containing NaK-nitrate, which is a state-of-the-art TES material, LiNaK-carbonate, and KMg-chloride were employed to study their effects on commercial and experimental alloys. The experiments were conducted at temperatures that exceeded 50–100°C than required in the power plants.

A comparative study of the corrosion resistance profiles of the chromia-forming and alumina-forming alloys in the three above-mentioned salt melts was conducted. Alloys exposed to nitrate melts were found to have the most predictable and highest levels of corrosion resistance compared to those exposed to the other melts. In stark contrast, the chromia-forming alloys in contact with carbonate melts showed catastrophic corrosion behaviours, characterised by a severe internal attack, i.e., carburisation, which progressed throughout the sample. On the other hand, the ferritic alumina-forming alloys showed an interesting and highly beneficial phase transformation of two $LiAlO_2$ polymorphs upon exposure to $(Li,Na,K)_2CO_3$ at 800°C. A dense, protective α-$LiAlO_2$ scale was formed and slowly grew over time despite being thermodynamically unfavourable; moreover, an outer, less-protective γ-$LiAlO_2$ phase formed. A comprehensive approach is adopted to study the microstructure and crystallographic evolution of these α/γ-lithium aluminate polymorphs. In addition, the consequences of pre-oxidation of the tested alloys are studied. Alloys exposed to the chloride melt underwent rapid degradation. The degradation was caused by selective element leaching. A transient Laves phase barrier formed in Kanthal® APMT to delay the selective chromium leaching. However, the aluminium was depleted and with high velocity instead.

One section of this thesis is dedicated to studying and understanding better the corrosion of evaporated salt species on the metallic materials of hot storage tanks. Interestingly, it was found that evaporated salt species caused more-severe corrosion than direct contact between the alloy and molten salt. Thus, metallic materials immersed in salt melts have not experienced the most-corrosive conditions in terms of salt/impurity mixtures. This conclusion is valid for the vessel set-up configuration used in this thesis, which includes the cover gas, salt melt and cover gas impurities.

Keywords: Concentrated solar power; Thermal energy storage; High-temperature corrosion; Molten salts; Alumina-forming alloys; Chromia-forming alloys; Alkali transition metalates, Alkali aluminate; Carburisation; Phase transition; Pre-oxidation; Alumina.

# List of Papers

This thesis is based on the following studies, which are referred to in the text by their Roman numerals:

**Paper I (a)**: *Perspectives on selected alloys in contact with eutectic melts for thermal storage: Nitrates, carbonates and chlorides*
Esraa Hamdy, Johanna Nockert Olovsjö, Christine Geers, **Solar Energy**. Vol. 224, p. 1210-1221 – Published 2021.

**Paper I (b)**: *Additional data and experimental setups, for a comparative study of alloys in contact to eutectic melts for thermal storage*
Esraa Hamdy, Johanna Nockert Olovsjö, Christine Geers, **Data in Brief**. Vol. 38., p. 107446 – Published 2021

**Paper II**: *Evaporated Alkali Carbonate Effect on an Aluminum Diffusion Coated 253MA Vessel after 4000 h Discontinuous Operation— Lessons Learned*
Esraa Hamdy, Angelina Wagné, Christine Geers, **Energies**. Vol. 15 (9), p. 3241 – Published 2022.

**Paper III**: *Direct and indirect contact of an austenitic high-temperature alloy to eutectic chloride melts with possible consequences for inhibitor strategies*
Esraa Hamdy, Antoine Pochi, Christine Geers – Manuscript under review.

**Paper IV**: *Differentiation in corrosion performance of alumina forming alloys in alkali carbonate melts*
Esraa Hamdy, Michal Strach, Johanna Nockert Olovsjö, Christine Geers, **Corrosion Science**. Vol. 192, p. 109857 – Published 2021.

**Paper V**: *Superior protection by α-$Al_2O_3$/α-$LiAlO_2$ double oxide scales against alkali carbonate corrosion*
Esraa Hamdy, Fang Liu, Christine Geers – Manuscript under review.

# Statement of the authors' contributions

## **Paper I (a)** and **(b)**

**Esraa Hamdy**: the principal author, conducted most of the exposure experiments, sample analyses, and improved set-up design; **Johanna Nockert Olovsjö**: sample material advisor and supplier of Kanthal® APMT, co-authored these articles; **Christine Geers**: conducted some of the exposure experiments and sample analyses, improved set-up design, performed the thermodynamic calculations, co-authored these articles.

## **Paper II**

**Esraa Hamdy**: data analysis, writing original draft; **Angelina Wagné**: data analysis; **Christine Geers**: data analysis, thermodynamic calculations, supervision, writing, reviewing and editing.

## **Paper III**

**Esraa Hamdy**: data analysis, writing original draft; **Antoine Pochi**: data analysis; **Christine Geers**: data analysis, thermodynamic calculations, writing, reviewing and editing.

## **Paper IV**

**Esraa Hamdy**: the principal author, carried out the experimental work and sample analyses; **Johanna Nockert Olovsjö**: Sample material advisor and main project partner for materials supplying, co-authored this article; **Michal Strach**: used Rietveld refinement method, TOPAS V6 software, α/γ-$LiAlO_2$ phase fraction calculations, co-authored the article. **Christine Geers**: conducted some of the sample analyses and co-authored the article.

## **Paper V**

**Esraa Hamdy**: conducted exposure experiments, sample analyses, the main author of this article. **Fang Liu**: sample analyses, co-authoring, reviewing and editing this article. **Christine Geers**: sample analyses, co-authoring, reviewing and editing this article.

# List of Abbreviations

| | |
|---|---|
| BIB | Broad Ion Beam |
| BSE | Backscattered Electrons |
| CSP | Concentrated Solar Power |
| DOE | Department of Energy |
| EDX | Energy Dispersive X-Ray |
| Gen3 | Third Generation |
| GHGs | Greenhouse Gases |
| HTF | Heat Transfer Fluid |
| IEA | International Energy Agency |
| IGC | Intergranular Corrosion |
| IPCC | Intergovernmental Panel on Climate Change |
| PV | Photovoltaic |
| RE | Reactive Elements |
| $sCO_2$ | Supercritical Carbon Dioxide |
| SE | Secondary Electrons |
| SEM | Scanning Electron Microscopy |
| TES | Thermal Energy Storage |
| XRD | X-Ray Diffraction |

# List of Symbols

| | |
|---|---|
| $a$ | Activity of Products and Reactants |
| $AMO_x$ | Alkali Oxide Scale |
| $G$ | Gibbs Free Energy |
| $H$ | Enthalpy |
| $k_p$ | Parabolic Rate Constant |
| $p(O_2)$ | Oxygen Partial Pressure |
| $R$ | Universal Gas Constant |
| $S$ | Entropy |
| $T$ | Absolute Temperature |
| $t$ | Exposure Time |
| $X$ | Oxide Scale Thickness |
| $Z$ | Atomic Number |

# Acknowledgements

On a beautiful sunny, snowy day, I am excited to be writing these "Acknowledgements". I thought that it would require no effort to write this last part of my thesis. However, with many pauses whilst trying to write, I realised it is not an easy task to acknowledge the innumerable individuals who have helped me not only during the past 4.5 years but also throughout my life to make this work possible.

In April 2018, a PhD position was announced at Chalmers University of Technology on the topic of corrosion in molten salts for thermal storage applications. In my diary back then, I wrote: *"There is a fantastic PhD position that I applied to, and it would be like a dream coming true if I got it!"*.

Words are inadequate to thank my main supervisor, Associate Prof. *Christine Geers*, for so many things, starting from my first interview until the present moment. I do not know where to begin, and I know well that she does not like being thanked. Still, I am deeply grateful for her meticulous supervision, patience, passion, eagerness, and support during my PhD journey. From all the amusing whiteboard discussions to the interesting philosophical talks about life, thank you for giving me the opportunity to learn, grow and be a part of the team.

I am immensely thankful to my co-supervisor, Associate Prof. *Fang Liu*, for all the keen and passionate discussions, thorough revisions, valuable comments, suggestions, and, finally, your kindness and understanding. I feel so lucky to have such a fantastic supervisory team.

I gratefully acknowledge my former and current directors of studies, Prof. *Jan Froitzheim* and Prof. *Itai Panas*, for their enormous support and guidance.

I also convey my respectable thanks to my examiner, Prof. *Lars Öhrström*, for his valuable advice and guidance.

I sincerely thank our administrators, *Sandra Nayeri* and *Anna Oskarsson*, for their continuous assistance since I moved to Sweden. I would also like to thank our financial administrator, *Christina Anderson*, for her support and advice concerning financial aspects.

Special thanks go to *Esa Väänänen*, our talented research engineer who built the experimental set-ups used in this work. I want to thank him for his enthusiasm and instant readiness to solve the challenges posed by the molten salt experiments. Also, I would like to thank *Torbjörn Jönsson*, who subsequently took over *Esa*'s role – thank you for your help with my experimental set-up upgrades.

I am thankful to my Master's degree students *Angelina Wagné* and *Antoine Pochi* for their passion, thorough work and all the results and data that they produced during their project course and internship.

I highly appreciate the cordial collaborations with dear colleagues in our team, *Dogac Tari* and *Aida Nikbakht*; working and discussing with you has been a great pleasure.

To my former and current officemates Dr. *Özgür Gündüz*, Dr. *Claudia Göbel*, *Esraa Darwish*, *Camilla Cossu*, and *Hampus Lindmark* – my thanks for your infinite support, advice, and amazing talks. My PhD journey would not have been the same without sharing the office with you.

I also wish to express my deepest gratitude to *Mareddy Reddy*, Dr. *Alberto Visibile*, Dr. *Duygu Yilmaz*, *Luca Gagliani* and *Elena Naumovska* for their continuous motivation, endless cooperation, and genuine concern for accomplishing this work.

For *everyone* at the Division of Energy and Materials, if I had the chance to choose my co-workers, I would never have found better people. Thanks for being welcoming and supportive and for all the nice talks and interesting discussions. Without you, it would not have been such a positive working environment.

I am thankful to our caretakers, *Fatima Joof* and *Kent Johansson*, for their helpful advice about life in Sweden and for very nice conversations.

I would like to thank the Swedish Energy Agency for funding this work through the thermal storage for SOLEL initiative under contract number 44653-1 and as a partner in the High-Temperature Corrosion Competence Centre.

For *Moufida, Rosa, Muwada, Amal, Zeinab, Lujain, Hanaa, Alaa, Yasmeen, Sheetal* and all my dear friends in Sweden, thanks for being my surrogate family and always being there for me whenever I need you.

For my *old and close friends*, for whom distances and time differences make it difficult to meet or talk in person, although we still manage to do so, it feels like we were together yesterday. I am very grateful to have you all in my life.

To my family, especially my sweet parents, *Fayza* & *Hamdy*, I want to thank you for your unconditioned love and guidance in whatever I pursue and for your substantial moral support and infinite warmth and tenderness. Words cannot fully express my enormous humble gratitude to you.

I am very thankful to my sister and best friend, *Eman*, for your continuous support since we were little kids. Despite your super busy schedule, your willingness to find time to talk and cheer me up has always melted my heart.

Even though we are on three different continents, my amazing brothers, *Sherif*, *Al-Hassan* and *Al-Hussein*, have always been supportive – my feelings that you are there for me have never changed.

For *everyone* I met, regardless of where, when and why, whether you gifted me a smile, a greeting nodding head, waving "hi", little talks in elevators, corridors, labs, conferences or meeting breaks, shared a tear or laughter, had deep conversions over lunch or funny conversations during a trip. I am grateful for all those memorable, beautiful moments that always made me smile and will continue to be the most precious gifts that I have received in my life. Thank you all!

*Esraa H. Mohamedin*

*March 2023, Gothenburg*

# Table of Contents


Abstract ..... iii

List of Papers ..... v

Statement of the authors' contributions ..... vi

List of Abbreviations ..... vii

List of Symbols ..... vii

Acknowledgements ..... ix

Table of Contents ..... xi

1 Introduction ..... 1

*1.1 Background ..... 1*

*1.2 Concentrated Solar Power Plant Technology ..... 2*

2 High-Temperature Corrosion and Oxidation ..... 5

3 Corrosion by Salt Melts ..... 13

*3.1 Corrosion in Chloride Melts ..... 15*

*3.2 Corrosion in Nitrate and Carbonate Melts ..... 18*

4 Experimental Layout ..... 23

*4.1 Materials ..... 24*

*4.1.1 Salt Melts ..... 24*

*4.1.2 Alloys ..... 26*

*4.2 Experimental Set-up ..... 27*

*4.3 Corrosion Experiments ..... 28*

*4.3.1 Immersed Isothermal Corrosion Experiments ..... 28*

*4.3.2 Specimens Taken from Alloy 253MA "Vessel Material" ..... 29*

*4.4 Analytical Methods ..... 34*

*4.4.1 Surface Analysis ..... 35*

*4.4.2 Metallographic Analysis ..... 36*

*4.4.3 Thermodynamic Calculations ..... 36*

5 Results and Discussion ..... 37

*5.1 Part I: Comparative Study of the Corrosion Performances of Chromia- and Alumina-Forming Alloys in Three Different Salt Melts ..... 38*

*5.2 Part II: Effects of Evaporated Salt Species on the Corrosion Behaviours of the Set-up Vessels 45*

*5.2.1 Vessel Hosting $(Li,Na,K)_2CO_3$-Exposure Experiments under $CO_2$ ..... 45*

*5.2.2 Vessel Hosting $MgCl_2$-KCl-Exposure Experiments under Argon ..... 49*

*5.3 Part III: Comprehensive Analysis of the Microstructural Evolution of Lithium Aluminate Formed on Selected FeCrAl Alloys Immersed in Carbonate Melt* ..... *52*

*5.3.1 Differentiation of Four FeCrAl Alloys and One FeNiCrAl Alloy Immersed in Carbonate Melt in the Absence of Pre-oxidation* ..... 54

*5.3.2 Corrosion Behaviours of Four Pre-oxidised FeCrAl alloys in Carbonate Melt* ..... 61

6 Summary ..... 67

7 Outlook ..... 69

References ..... 71

# 1 Introduction

## 1.1 Background

In 2021, the Intergovernmental Panel on Climate Change (IPCC) published the first part of the *Sixth Assessment Report on Climate Change.* This report summarises the current climate situation and the role of humans in climate change. Since the year 1750, human activities have been primarily responsible for the observed increase in the atmospheric concentrations of greenhouse gases (GHGs). This increase in GHGs, especially over the last four decades, has increased global temperatures at a rate that has not been witnessed for at least 2,000 years, according to the IPCC *Climate Change Assessment Report* [1]. Human-induced climate change has most likely caused changes in the weather patterns in almost all regions of the world, leading to droughts, heat waves, and tropical cyclones [1]. Therefore, it has become necessary to reduce the levels of these harmful GHGs. In the Year 2015, 196 countries agreed at the UN Climate Change Conference (COP21) in Paris to limit global warming by taking serious steps and adopting strategies to reduce GHG emissions [2].

Most of the world's energy supply is provided by fossil fuel combustion. During the 20$^{th}$ Century, the burning of fossil fuels increased dramatically, resulting in high $CO_2$ emissions [1, 3]. In contrast, renewable energy sources, such as solar and wind, cause almost no $CO_2$ emissions during production. Therefore, switching to renewable energy to supply power provides a solution for reducing GHG emissions [3]. Concentrated solar power (CSP) is an interesting technology that utilises the sun, a clean, abundant, and inexhaustible energy source [4]. Two major solar energy technologies with high potential can be used for electrical power generation: photovoltaics (PVs) and CSP. Since both technologies utilise the same energy sources, studies have compared their potential and competitiveness levels. The main criteria for deciding which technology is better to implement are: land use restrictions and land cover types. For instance, CSP technology is used at remote sites that have high-level, direct solar radiance, e.g., South America, South Africa and the USA.

In comparison, PV technology is recommended for use in regions with humid atmospheres, in the north-temperate zone, and in urban environments. However, at other locations, there is no clear winner, although other assessments need to be considered [5]. In addition, CSP is superior to PV due to its longer storage duration and the greater magnitude of its large-scale dispatchable base-load electricity, even though PV can be combined with batteries, in which electrical energy is stored as chemical energy [5, 6]. There is a growing need to increase the efficiency levels of CSP plants so as to make them cost-competitive and have higher energy market penetration.

Third-generation (Gen3) CSP plants are designed to increase the efficiency of the process by using supercritical carbon dioxide ($sCO_2$) instead of steam for the Brayton cycle gas turbines, and this requires an operating temperature >700°C. The higher operating temperature of the $sCO_2$ Brayton cycle demands a minimum thermal energy storage (TES) material temperature of 750°C [7-11]. The higher operating temperature also entails serious challenges in terms of the thermal stability of the respective heat transport

medium and the resilience of the metal components to high-temperature corrosion. Thus, corrosion is a major obstacle to be overcome on the road to commissioning the first $sCO_2$ Brayton cycle-operated CSP plant [12, 13].

The work conducted for this thesis focuses on studying the compatibility between different molten salts used as TES materials and the metallic components that contain them. Corrosion by salt species at high temperatures is certainly not a new issue in the field. However, depending on the choice of commercial or experimental alloy, the longevity and safety of a plant module can be substantially impacted. A deeper understanding of underlying chemical processes would support and guide the alloy selection process.

## 1.2 Concentrated Solar Power Plant Technology

Although the CSP technology dates back to the 1970s, most commercial CSP plants have been established only in the last decade [2–4]. In the International Energy Agency (IEA) report, it is stated the CSP technology could contribute 11.3% of the world's electricity by the Year 2050, assuming appropriate support measures [14]. However, the CSP technology is still not cost-competitive with other power generation technologies. To remedy this, the US Department of Energy (DOE) launched the SunShot Initiative roadmap in 2011, with a cost target of 6 ¢/kWh for electricity from CSP plants [15]. Reaching this goal necessitates increasing the efficiency levels of CSP plants, thereby improving the performances of different CSP plant components. Before discussing the approaches proposed by the SunShot Initiative to achieve the 6 ¢/kWh cost target, an overview of how a CSP plant works is provided below.

The CSP plant is schematically illustrated in Figure 1.1. The CSP system comprises thousands of mirrors (heliostats) that track, concentrate, and reflect the solar radiation to a focal point at the top of a tower receiver, where the solar radiation is converted into thermal energy. A heat transfer fluid (HTF), which is also a TES material, is pumped into the top of the tower receiver to capture the solar radiation and collect it in the form of heat. The heat collected by the HTF is then either used directly to generate electricity by heating steam to run a turbine or is transported and stored in the hot TES tank until electricity is required. When there is a demand for electrical power, the stored heat in the hot tank is used to power a turbine, using steam or $sCO_2$, so as to drive a generator and produce electricity [4].

Since heat storage is one of the distinct advantages of CSP technology, considerable efforts have been exerted to study materials that can act as the HTF or TES medium. The different TES storage media are classified as: (i) *sensible heat storage*, where the amount of stored heat depends on the temperature, quantity of the employed TES material, and its specific heat capacity without any phase change; (ii) *latent heat or phase-change materials*, where thermal energy is stored during a phase change; and (iii) *thermochemical heat storage*, where energy is stored/dispatched via a reversible thermochemical reaction. Despite the high storage capacity of the latent heat and thermochemical TES forms, active commercial plants currently employ sensible storage capacity due to its easier conditions of operation and the lower complexity level of the system [16].

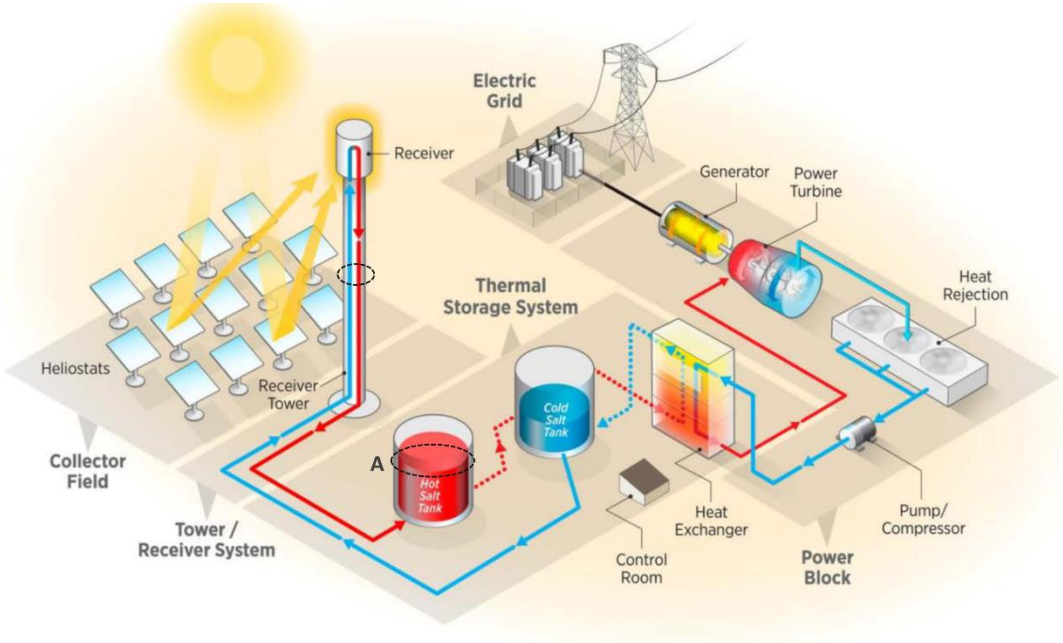


*Figure 1.1 Schematic illustrating the components of a concentrated solar power plant [15, 17].*
*Source: US Department of Energy Report: The Year of Concentrating Solar Power, DOE/EE-1101, May 2014.*

Numerous studies have investigated TES materials for their potentials to operate at such high temperatures (for reviews, see [16, 18-20]). The TES materials employed in the currently active commercial CSP plants include nitrate melts and other commercial mixtures. A eutectic salt mixture (60 wt% $NaNO_3$, 40 wt% $KNO_3$), which is known as "Solar Salt", is utilised in the current CSP plants [15, 21].

A eutectic system is a homogeneous mixture of two or more components that has a lower melting point than the respective pure substances at a particular mix ratio of the components. This temperature is called "the eutectic temperature", *E* (see Figure 1.2) [22]. For instance, the $T_m$ value of pure $KNO_3$ is 334°C, and that for pure $NaNO_3$ is 308°C, while their eutectic mixture melts have a $T_m$ of 230°C [15].

Due to the lower melting temperature of the eutectic salt, mixtures are commonly utilised in TES applications in which it is essential to maintain the TES materials and HTFs in their molten states and to avoid freezing, particularly in the pipes.

Solar salt has been selected for its favourable thermo-physical properties, e.g., melting temperature, thermal storage capacity, thermal conductivity, thermal stability, density, vapour pressure, and comparatively mild corrosiveness. However, due to thermal decomposition, alkali nitrates are unsuitable for utilisation at temperatures >550°C. Alloys that have recently been applied in alkali nitrate-operated CSP plants are: low carbon steel-A1045 and stainless steel grades 304 and 316 for TES tanks, and the nickel alloy Inconel 600 for the tower receiver [23]. The choice of metallic materials used in the tanks depends on the operating temperatures. For instance, the Andasol 1 parabolic trough CSP plant in Spain operates at low temperatures (293°–393°C), while the Gemasolar CSP plant in Spain operates at higher temperatures (290–565°C) [24].

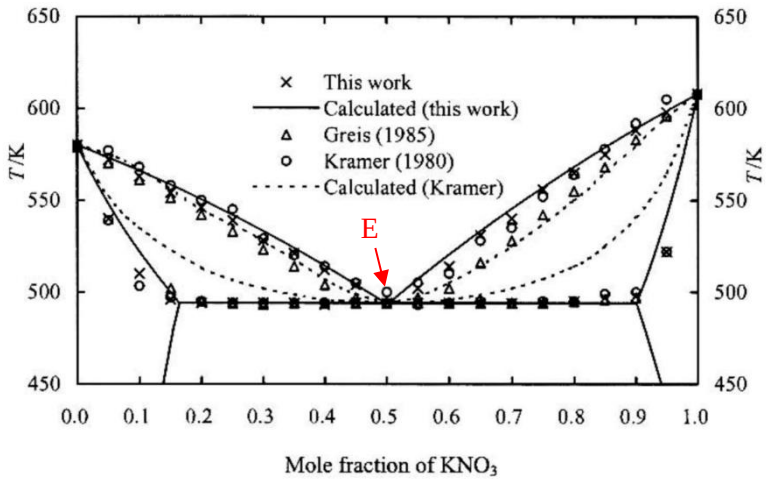


*Figure 1.2 Schematic phase diagram of a binary $NaNO_3$-$KNO_3$ eutectic system* [25]*, where E is the eutectic temperature.*
*Source: Zhang, X., et al., Thermodynamic evaluation of phase equilibria in $NaNO_3$-$KNO_3$ system, 2003. Reproduced with permission from the Journal of Phase Equilibria.*

Since Gen3 CSP plants require higher operating temperatures, other TES materials that can withstand the increased target temperature have been investigated. The two most-frequently proposed TES candidates are: i) a ternary carbonate mixture (32.1 wt% $Li_2CO_3$, 33.4 wt% $Na_2CO_3$, 34.5 wt% $K_2CO_3$) and; ii) a binary chloride mixture (64.4 wt% KCl, 35.6 wt% $MgCl_2$). These salt mixtures differ with respect to cost, abundance, thermal stability, liquid temperature range, and corrosiveness level [12, 15, 18].

Increasing the temperature of salt melts increases their corrosivity towards metallic materials. Therefore, a significant improvement in compatibility between the container material (tanks/pipes/heat exchangers) and the TES medium is necessary [13, 15]. Corrosion of the metallic materials in contact with the storage medium can lead to catastrophic failure of an entire CSP plant due to material loss or embrittlement. Alloys currently operated in contact with the Solar Salt material do not have sufficient high-performance levels to allow them to be used in contact with alternative high-temperature melts. This will be a reference case in this thesis.

This work aims to study the corrosion behaviours of metallic components employed in the hot storage tank, focusing on their compatibilities with salt melts that might be used in Gen3-CSP plants. This work is divided into three parts. The first part compares the compatibility profiles of the current and potential molten salts and alloys that could be deployed in hot storage tanks. The second part investigates the behaviours of the alloys in indirect contact with salt melts, for instance, the metallic components exposed to evaporated salt species in the tank. The third section is dedicated to deepening our knowledge regarding an interesting observation made for ferritic FeCrAl alloys immersed in a $(Li,Na,K)_2CO_3$ melt. The $\alpha/\gamma$-$LiAlO_2$ phase transition was thoroughly studied, and microstructural and crystallographic analyses were conducted.

# 2 High-Temperature Corrosion and Oxidation

High-temperature corrosion is defined as the thermodynamically driven degradation of materials at temperatures ≥400°C. At high temperatures, metallic materials are susceptible to degradation processes, such as oxidation, nitridation, carburisation, chlorination, and hot corrosion [26]. The inclusion of high-temperature oxidation in this context of corrosion has an important exception: the formation of protective oxide layers used to prevent the uncontrolled reactions of other corrosive species on alloys.

The term "oxidation of metals" is mostly used to describe the interactions of a metal with the surrounding oxygen in the environment, to form a metal oxide scale. As shown in Figure 2.1, the oxide scale is initially formed by oxygen adsorption to the metal surface and oxygen reduction by electrons from the alloy elements to form $O^{2-}$. When oxide ions and metal cations occupy their respective lattice positions at the metal/gas interface, the oxide scale nucleates and grows laterally until it covers the entire metal surface. Oxide scale growth can proceed either outwards through metal ion transport to cationic vacancies that lie adjacent to the adsorbed oxygen ions or inwards when oxygen ions occupy the oxygen vacancies formed at the alloy/oxide interface [27]. These principles have been described and established by Carl Wagner [28].

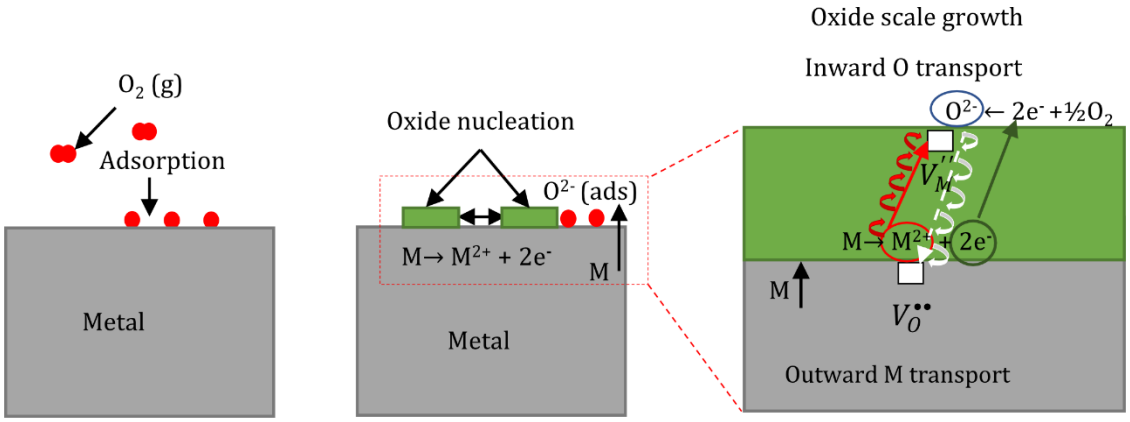


*Figure 2.1 Oxide scale formation process, where $V_O^{\bullet\bullet}$ is an oxygen vacancy and $V_M''$ is a metal vacancy.*

The oxide scale can be considered beneficial if it acts as a corrosion-resistant barrier that prevents the surrounding environment from interacting with the metal. For an oxide scale to be protective, it needs to have the following characteristics: slow-growing, dense, continuous, well-adherent, and inert to reactions with the environment, such as dissolution [29].

Understanding which types of corrosion products can form as a result of high-temperature oxidation of the alloy is essential. These products include an outer scale that acts as a protective barrier against the corrosive environment. In several studies, pre-oxidation has been applied to alloys so as to create a protective layer against more-aggressive chemical species, such as molten salts [30-33].

The following sections present an overview of the thermodynamics, kinetics, and growth of the oxide scale. The fundamental concepts that apply to all high-temperature corrosion processes are: a sequence of spontaneous processes; electrochemical coupling between the metal and the environment; and increasing entropy with increasing temperature [26, 29, 34].

Equation (2.1) describes the oxidation of a single metal when exposed to oxygen:

$$xM(s) + \frac{y}{2}\, O_2(g) \leftrightharpoons M_xO_y(\boldsymbol{s}, l, g) \quad (2.1)$$

where *M* is the exposed metal, and *x* and *y* are the stoichiometric constants. Only solid oxides are relevant for the formation of an oxide scale.

Many factors influence oxide scale formation, such as temperature, alloy chemistry, exposure time, and the oxygen partial pressure $p(O_2)$ in the environment. To determine the comparative stabilities of metal oxide species at different temperatures, the second law of thermodynamics is used in terms of the Gibbs free energy, assuming that the temperature and pressure are constant. It is important to stress that there is a minimum value of $p(O_2)$ for oxidation at each temperature. If this value is not reached, the metal remains in metallic form.

$$\Delta G = \Delta H - T\Delta S \quad (2.2)$$

where *G* is the Gibbs free energy of the system, *H* is the enthalpy, *T* is the absolute temperature, and *S* is the entropy. When the ΔG value of a reaction of a metal with oxygen, in our case, is <0, the reaction is thermodynamically favourable and occurs spontaneously, i.e., the oxide is stable. Whereas, when the ΔG value of the system is >0, the reaction is thermodynamically unfavourable, and the metal remains metallic. If ΔG=0, the system is at equilibrium.

The Gibbs free energy for Eq. (2.2) per mole of oxygen can be written as follows:

$$\Delta G = \Delta G° + RTIn\left(\frac{a\,(MxOy)}{a_M^x \cdot p_{O2}^{y/2}}\right) \quad (2.3)$$

where $\Delta G°$ is the standard Gibbs free energy, *R* is the universal gas constant, and *a* is the activity of the products and reactants.

Since the activity of the solid materials equals one, the activity of the gases corresponds to their partial pressure. Equation (2.3) can be simplified as follows when the system is at equilibrium ($\Delta G = 0$):

$$\Delta G° = RTIn\left(p_{O_2}^{y/2}\right) \quad (2.4)$$

As can be concluded from Eq. (2.4), the formation or dissociation of an oxide scale depends on the temperature and equilibrium $pO_2$. Ellingham-Richardson diagrams illustrate by normalising all the reactions to 1 mole $O_2$ the relative stability of oxides as a function of temperature and $pO_2$ (see Figure 2.2). The lower the line at which an element is positioned in the Ellingham diagram, the more negative Gibbs free energy it has and the greater the stability of the oxide [35].

$Al_2O_3$ is among the most-stable oxides. Other relevant oxides are iron oxide and chromium oxide.

Iron requires higher oxygen partial pressures to form its oxides than aluminium. Three iron oxide phases are depicted in Figure 2.2: wüstite, FeO; magnetite, $Fe_3O_4$; and hematite, $Fe_2O_3$. Wüstite has the poorest corrosion resistance, followed by magnetite, while hematite, which has a corundum-type structure, is the most-protective of the three oxides.

*Eskolaite* ($Cr_2O_3$) has a corundum-type crystal structure. In this structure, oxygen anions form a hexagonal closed-packed lattice within which the metal cations fill two-thirds of the octahedral holes. Chromium oxide forms a dense, slow-growing scale with a high degree of stoichiometry, enabling it to act as a protective barrier against corrosion.

Aluminium oxide has several allotropic forms, of which $\alpha$-$Al_2O_3$ is the most-desirable and thermodynamically stable with a corundum-type structure. Other meta-stable forms of alumina, such as $\gamma$-$Al_2O_3$, offer less corrosion protection than $\alpha$-$Al_2O_3$.

The corundum-type oxides, such as hematite, eskolaite and α-alumina, can form solid solutions.

It is important to point out that the pure oxides described above can only be formed as an inner oxide scale. Due to the incorporation of alkali species from the melt into outward-growing oxides, an alkali transition metal oxide ($AMO_x$) is produced, as discussed in Chapter 3.

The Ellingham-Richardson diagram visualises the temperature and oxygen partial pressure-dependencies of the Gibbs free energy for individual element oxidation reactions. However, due to differences in reaction rates, it is not always the oxide with the highest thermodynamic stability that forms first, but instead, rapidly nucleated metastable phases. Therefore, kinetic considerations are important for a better understanding of the corrosion process. Knowing the rates of reactions helps towards understanding the corrosion mechanism, and this is also essential for estimating the lifetime of an alloy implemented in certain applications and under specific conditions.

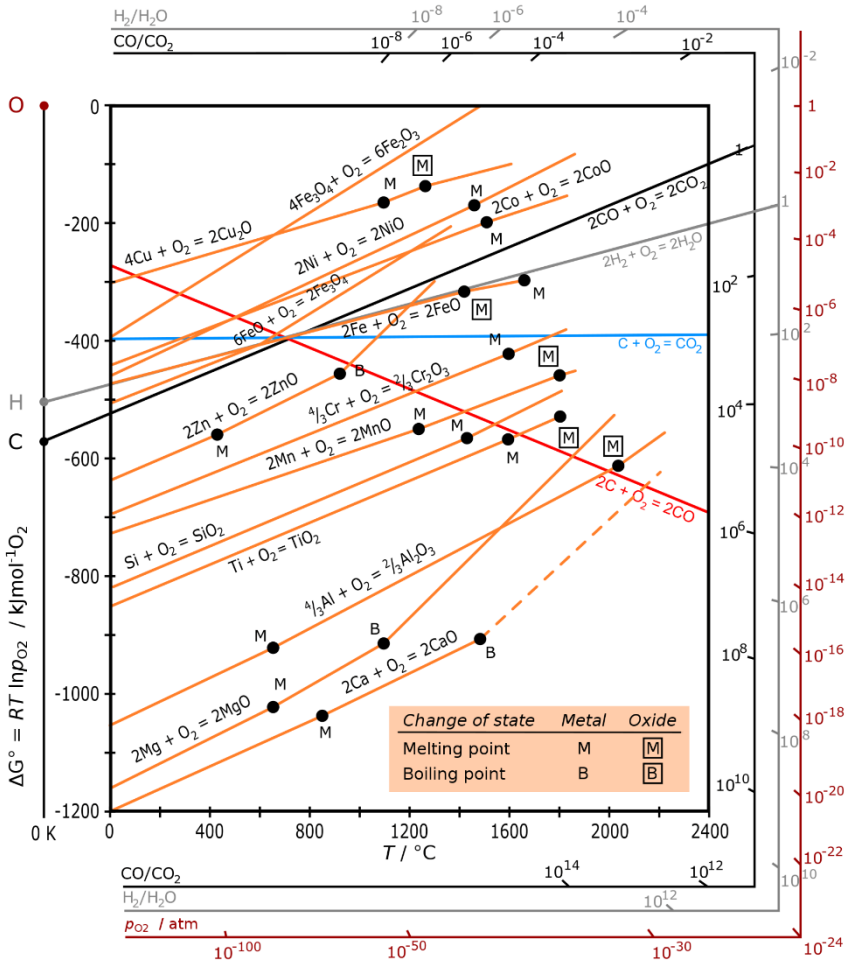


*Figure 2.2 Ellingham-Richardson diagram showing the Gibbs enthalpies of the oxidation reactions as a function of temperature for different elements and, thereby, their relative oxide stabilities.*
*Source: Ellingham-Richardson diagram from Wikimedia Commons. Available at commons.wikimedia.org [35, 36].*

Oxidation kinetics are generally determined by measuring the corroded metal's mass change as a function of time. However, in some cases, and particularly in the present work, it is difficult to obtain accurate mass change measurements for the exposed samples due to the yet-unquantified dissolution of alloy elements into the liquid phase, as well as the intense surface cleaning methods. In addition, the mass change values might not always relate to scale growth. Oxidation kinetics are commonly defined in terms of ideal rate laws and used to evaluate oxide scale growth. As depicted in Figure 2.3, kinetic laws of scale growth are often expressed by a low number of ideal behaviours: logarithmic, parabolic and combinations thereof.

Logarithmic corrosion behaviour is present when an initial rapid increase in mass change is detected, and subsequently, the mass gain rate declines significantly. Initially, relatively fast oxidation forms a thin oxide scale, which decelerates with time, obeying Eq. (2.5):

$$X = k_{log} \log\ (t + t_0) + A \quad (2.5)$$

where $X$ is the oxide scale thickness, which can also be replaced by the measured mass gain Δm, $k_{log}$ is the logarithmic rate constant, $t$ is the exposure time, and $A$ is a constant. This behaviour expresses very efficient passivation of a metal surface through oxide scale formation. At high temperatures, α-$Al_2O_3$ presents similarly excellent oxidation behaviours due to the large band gap characteristic suppressing the transport of charge carriers across the oxide scale [37].

Most oxide scales formed during high-temperature oxidation are described according to the parabolic kinetics reported by Carl Wagner [28], as shown in Eq. (2.6). In this process, scale growth relies on the diffusion of ions and electrons through the formed oxide scale. Thus, the thicker the scale, the longer the paths for the charged species travelling through the scale (see Figure 2.1).

$$X^2 = k_p\ t + C \quad (2.6)$$

where $X$ is the oxide thickness, $k_p$ is the parabolic rate constant, $t$ is the exposure time, and $C$ is the integration constant. The mass change $\Delta m$ can be employed instead of the scale thickness $X$.

Breakaway oxidation, which can be distinguished from the alloy's kinetic behaviour, is described as a transition from a slow-growing scale to a thick, non-protective, fast-growing scale, as reflected by high mass gain values. For this study, the mass change diagram (Figure 2.3) has been extended with a mass loss curve, which occurs in a special case discussed in Chapter 5.1. In this case, mass loss occurs in the absence of oxidation, nitridation or carburisation, where metal leaching from alloys through, for example, chloride attack occurs instead.

The exponentially accelerating behaviour of the dissolution process can be attributed to the increase of contact area with time, which is linked to the increased accessibility levels of grain boundaries and cavities, among others.

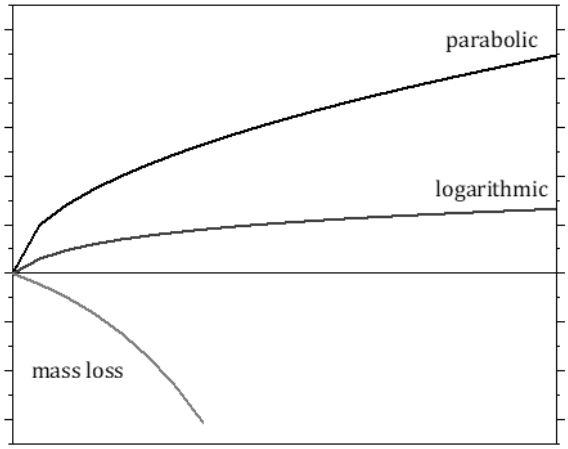


*Figure 2.3 High-temperature oxidation kinetics: positive mass change values represent the kinetic behaviour for oxide scale growth [27]. Negative mass change values are attributed to mass loss due to leaching as a result of chloride attack in the absence of an oxide scale.*

Following the initial rapid formation of a thin oxide scale, the thickness increases progressively through the transport of charge carriers across the scale. As shown in Figure 2.1 and described by Carl Wagner [28], scale growth requires the transport of metal cations, oxide ions, electrons, and oxygen or metal vacancies. We can distinguish between inward- and outward-growing oxide scales. Outward-growing oxide scales grow by outward cation diffusion, while inward-growing scales grow due to inward diffusion of anions, e.g., $O^{2-}$. These charged species can travel through the oxide scale lattice using solid-state diffusion, depending on the grain size or crystal defect concentration. Crystal imperfections can be classified as: point defects (0D), such as vacancies and interstitials; line (1D) and plane (2D) defects, such as dislocations and grain boundaries; and volume imperfections, such as precipitates and voids.

A point defect is found when a crystal lattice is missing an atom, thereby creating a vacancy or the presence of an interstitial atom in an irregular site. A Schottky imperfection is a point defect where a vacancy is generated in a crystal lattice due to an atom migrating from its regular site in the interior through successive steps until it reaches and settles at the crystal surface. Another type of point defect is a Frenkel imperfection. It occurs when an atom is freed and leaves its regular site, forming a vacancy and then moving to another interstitial site within the crystal (see crystal imperfections illustrated schematically in Figure 2.4) [38].

In Schottky defects, a cationic vacancy is a charge balanced by an anionic vacancy. A Frenkel defect comprises a cation or an anion vacancy electrically balanced by an interstitial cation or an anion, respectively.

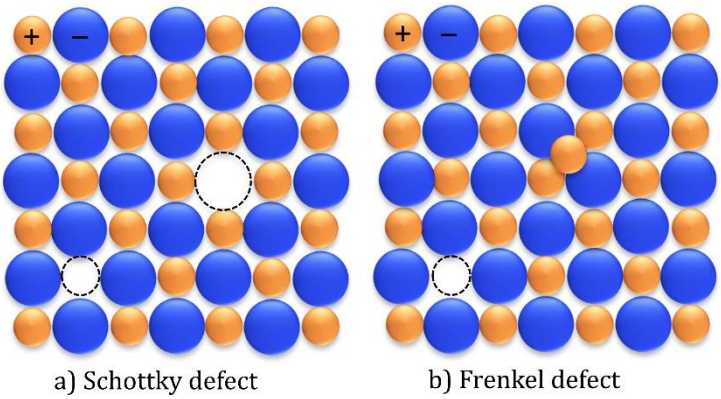


*Figure 2.4 Schematic illustrations of Schottky and Frenkel defects in ionic solids [38].*

The diffusion paths that ions, electrons, and vacancies occupy across oxide scales can be distinguished as lattice-defect diffusion and short-circuit diffusion pathways.

In lattice diffusion, ions travel through the most common types of crystal defects, i.e., vacancies. Since lattice-defect diffusion typically requires higher activation energies than short-circuit diffusion, it usually predominates at relatively high temperatures.

Short-circuit diffusion relies on extended microscopic defects, such as grain boundaries, dislocations, or segregated phases with higher conductivity. These are relatively easy paths, and since they require lower activation energies, these paths facilitate oxide growth even at lower temperatures.

# 3 Corrosion by Salt Melts

This chapter focuses on corrosion in a more complex environment; namely salt melts. An overview of the corrosion processes that occur in nitrate, carbonate, and chloride melts is provided, covering the thermodynamics, corrosion products, kinetic processes, and the roles of impurities in such corrosive environments. As discussed in Chapter 2, most high-temperature alloys form a protective oxide scale that is dictated by the alloy composition and specific exposure conditions. High-temperature corrosion in molten salts is not that different from oxidation in a gas environment in terms of the basic anodic process [Eq. (3.1)] and the reduction of oxidising species [Eq. (3.2)], which results in metal oxide formation.

$$M \rightarrow M^{n+} + ne^{-} \quad (3.1)$$

$$O_2 + 4e^{-} \rightarrow 2O^{2-} \quad (3.2)$$

Nevertheless, the level of complexity is increased by the presence of more than one potentially oxidising species, more than one reacting cation at the melt/oxide interface, and reactions that can occur within the melt or melt/gas interface [39]. Gas environments that cause high-temperature corrosion commonly comprise more than one gas species, with each species having a partial pressure <1. The salt melts considered in this study are mixtures of nitrate, carbonate, and chloride salts. In these mixtures, the activity is one for all the cationic and anionic species.

Molten salts are electrolytes, and they support electrochemical reactions. At the metal/melt interface, alloy elements can be oxidised, and salt species and impurities can be reduced. The identification of the decisive redox pairs allows us to apply, in this case, basic assumptions regarding the salt melt reactions with alloy species.

The ionic salt species play significant roles in the corrosion process. The anionic species can be categorised as: *oxyanions*, such as sulphate $SO_4^{2-}$, nitrate $NO_3^{-}$, and carbonate $CO_3^{2-}$; and *halide-based salts*, such as chloride $Cl^{-}$ [39].

Compared to corrosion that occurs in aqueous solutions (where the pH value plays a significant role since the solubility of the corrosion products depends on the acidity or basicity of the solution), corrosion in molten salts follows a similar concept [40]. Even though salt melts do not contain protons, the acid-base concept proposed by Lux and Flood *et al.* is still valid [41, 42]. A Lewis acid is an electron pair acceptor with available empty valence orbitals. In turn, a Lewis base is an electron pair donor. In the molten salts, the acid-base concept is proposed as follows in Eq. (3.3):

$$base = acid + O^{2-} \quad (3.3)$$

From Eq. (3.3), bases are $O^{2-}$ donors and acids are $O^{2-}$ acceptors; by applying this concept to molten salts, a nitrate or a carbonate melt is considered a base, as shown in Eqs. (3.4) and (3.5):

$$NO_3^- = NO_2 + O^{2-} \quad (3.4)$$

$$CO_3^{2-} = CO_2 + O^{2-} \quad (3.5)$$

Since the oxyanion $O^{2-}$ in a molten salt solution acts similarly to $H_3O^+$ion in an aqueous solution, a p$O^{2-}$ value can be calculated using Eq. (3.6):

$$\mathrm{p}O^{2-} = -\log a_{O^{2-}} \quad (3.6)$$

where $a_{O^{2-}}$ is the oxyanion activity in the salt melt. It is important to stress that the *oxyanion* acid-base concept is only valid for reactions that occur in molten salt solutions [40].

The *oxyanion* acid-base concept cannot be applied to molten salt systems that do not contain oxygen ions. Therefore, another definition must be adopted in this case. For instance, a salt melt with a low level of self-dissociation, e.g., for the $AlCl_3$ melt, a substance that produces $AlCl_2^+$ *is* an acid, whereas if it releases $AlCl_4^-$, then it is a base; see Eq. (3.7):

$$2AlCl_3 = AlCl_2^+ + AlCl_4^- \quad (3.7)$$

As discussed in Chapter 2, corrosion is an electrochemical reaction in which the metal is oxidised upon interaction with its environment. Similar to corrosion in aqueous solutions, molten salts are not any different due to their excellent ionic conductivities. It is essential to stress that corrosion caused by metal dissolution is a good example of a process that involves two electrochemical partial reactions: anodic with metal dissolution; and cathodic through the reduction of an oxidant. The rate, if not transport-dependent, of each partial reaction is dependent upon the electrode potential.

It is also important to emphasise that metal dissolution is only one of the reactions that can occur in such an environment. For instance, reactions with the alloy can be anodic, cathodic or chemical. A detailed scheme of the possible reactions in a salt melts environment has been presented by Rahmel [40].

It is important to differentiate between a reaction that causes corrosion and one that determines the corrosion rate. The latter depends on the diffusivity of ions (charge carriers) within the molten salt. In comparison, the rate-determining step is the charge transfer reaction in aqueous solutions.

Another difference between corrosion in aqueous solutions and molten salts is electrical conductivity. Aqueous media only display ionic conductivity, while some molten salts have both ionic and electric conductivities, e.g., alkali-chloride melts. For salt melts with electric conductivity, oxidant reduction can occur in the melt or at the metal-gas interface instead of only occurring at the metal-melt interface. Consequently, electric conductivity increases the oxidant reduction reaction, leading to a significant difference, especially if the solubility of the oxidant (usually oxygen) is low in the melt [40].

The following sections summarise the most-relevant corrosion mechanisms in chloride, nitrate, and carbonate melts.

## 3.1 Corrosion in Chloride Melts

Chloride melts are candidate HTF and TES media for Gen3-CSP plants due to their superior thermal stabilities and favourable thermal properties [15]. Considering the standard electrochemical series of elements, alkali chlorides are theoretically good candidates for high-temperature corrosion since neither $A^+$ nor $Cl^-$ions can be reduced by metal species from the alloy, which means that there is no corrosion [39].

$$M(alloy) + A^+ + Cl^- \nrightarrow M^+ + A(metallic) + Cl^- \quad (3.8)$$

Indacochea *et al.* have studied the corrosion profiles of low-alloy steel and different stainless-steel alloys that were exposed to LiCl melt at 725°C for 30 days in argon under extremely pure and dry conditions; it has been reported previously that corrosion is successfully suppressed under these conditions. However, after replacing argon with Ar-10% $O_2$, the alloys underwent severe corrosion, forming non-protective oxides [43, 44]. Thus, alloy constituents can reduce oxygen or water, and one can conclude that oxidising impurities drive high-temperature corrosion in alkali chloride melts [24, 40, 45].

Common impurities, such as oxygen and moisture, can oxidise metal components and bring them to the salt flux in an ionic form [24, 45]. Consequently, the alloy suffers a rapid metal loss, which is accelerated by the absence of passivating oxide scales. In addition to their reactions with metallic components, chloride melts react with oxygen and moisture, producing $Cl_2$ and HCl [45-47], as depicted in Eqs. (3.9) and (3.10):

$$4\,Cl^- + O_2 = 2\,Cl_2 + 2\,O^{2-} \quad (3.9)$$

$$H_2O + Cl^- = HCl + OH^- \quad (3.10)$$

Different aspects must be taken into account to comprehend the corrosive effects of molten chlorides on metallic materials. Ding *et al.* and Patel *et al.* have extensively reviewed the corrosion behaviours of various alloys when in contact with chloride melts [48, 49]. In their review, Ding *et al.* classified the corrosion processes caused by a chloride melt into three distinct categories: (i) interactions between the salt and the environment/cover gas; (ii) reactions that take place within the salt melt itself, such as decomposition or hydrolysis; and (iii) the interactions of the metallic components of the alloy with the salt melts or salt-containing environment [49]. The review concluded that the corrosion caused by chloride melts could be attributed to different mechanisms owing to these three distinct processes. Furthermore, additional factors, such as the operating temperature, chemistry of the employed salt melt, alloy composition, and gas environment, play roles in determining the degree to which the corrosion progresses.

The corrosion resistances of alloys are highly dependent upon their chemical compositions. Ni-based superalloys exhibit superior corrosion resistances to chloride melts, as compared to stainless steel [50]. However, no definite conclusion can be drawn with regard to the significance of the Ni-content, as there are reported cases in which alloys with a high percentage of Ni have failed to resist corrosion, as highlighted in the review paper of Ding *et al.* [49]. Nonetheless, it has been reported that there is a direct correlation between the oxygen partial pressure and corrosion rate, which means that oxygen transport to the metal/melt interface is the rate-determining step in such an environment [51, 52].

Multiple studies have investigated the corrosion behaviours of several alloys in contact with chloride melts under different conditions [30, 39, 53-58]. The key finding from these studies is that corrosion in chloride melts is impurity-driven.

Various research studies have investigated the corrosiveness levels of chloride melts for iron-based, nickel-based, and model alloys at temperatures in the range of 500°–650°C [57, 59-61]. It has been reported that, in the presence of oxygen or moisture, chloride salts severely attack alloys that have excessive chromium leaching, particularly along grain boundaries [40, 62, 63]. Laboratory tests have confirmed the presence of defect-rich porous scales, selective element leaching, pore formation in bulk materials, and inter-granular attack [31, 40, 48, 57, 64]. Equations (3.11) and (3.12) represent two possible exothermic reactions that can destabilise the chromia scale at high temperatures. Chromia reacts with potassium chloride in an oxygen-rich environment to form soluble alkali chromate, volatile chromium chloride, and oxy-chloride species [40].

$$24\ \mathrm{KCl\ (g,s,l)} + 10\ \mathrm{Cr_2O_3(s)} + 9\ \mathrm{O_2\ (g)} \rightarrow 12\ \mathrm{K_2CrO_4(l)} + 8\ \mathrm{CrCl_3}(g) \quad (3.11)$$

$$8\ \mathrm{KCl\ (g,s,l)} + 6\ \mathrm{Cr_2O_3(s)} + 3\ \mathrm{O_2}(g) \rightarrow 4\ \mathrm{K_2CrO_4\ (l)} + 8\ \mathrm{CrOCl\ (s)} \quad (3.12)$$

Intensive efforts have been made to reduce the concentrations of oxygen and other impurities in the chloride melt environment due to their effects on the corrosion rate.

$MgCl_2$ is commonly used in chloride eutectic melts to lower the melting temperature. Due to the highly hygroscopic nature of $MgCl_2$, many efforts have been made to reduce its content of impurities and to implement salt purification methods for improved corrosion resistance [24, 65-69]. In general, alloys that are in contact with $MgCl_2$-containing melts tend to precipitate MgO onto their surfaces and deplete the metals, e.g., Cr, beneath the surface [50, 58].

Highly hygroscopic $MgCl_2$ reacts with water impurities to produce MgOHCl and HCl at temperatures >300°C. At temperatures >550°C, this reaction further breaks down to yield MgO and HCl [68], as in Eqs. (3.13), (3.14) and (3.15) [70]:

$$\mathrm{MgCl_2 \cdot 2\ H_2O} \rightarrow \mathrm{MgOHCl} + \mathrm{HCl(g)} + \mathrm{H_2O} \quad (3.13)$$

$$\mathrm{MgCl_2 \cdot H_2O} \rightarrow \mathrm{MgOHCl} + \mathrm{HCl\ (g)} \quad (3.14)$$

$$\mathrm{MgOHCl} \rightarrow \mathrm{MgO} + \mathrm{HCl(g)} \quad (3.15)$$

The reactions of $MgCl_2$ can be a major concern for TES systems, particularly in terms of producing corrosive gaseous HCl. These reactions pose serious challenges due to changing the thermo-physical properties of the melt, e.g., melting/freezing point, heat capacity and density. Such changes can place CSP plants at risk of unsafe operation and power-generation failure. Furthermore, MgO particulates can block the primary heat exchanger and erode the salt pumps. Therefore, it is essential to purify $MgCl_2$-containing chloride salts properly [65].

One approach to minimising the concentrations of impurities in $MgCl_2$-containing mixtures, e.g., $MgCl_2 \cdot 6\ H_2O$, is step-wise heating and sweeping away the volatile side-products by flowing inert gas.

This method reduces the formation of corrosive species such as MgOHCl. Even though the step-wise heating procedure lowers the corrosivity of the melt, it does not eliminate all the hydroxide impurities [70, 71].

Another approach is the addition of Mg metal to $MgCl_2$-containing mixtures [69, 72-77] or metallic Be to lithium-beryllium fluorides [78]. In this method, the Mg metal acts as a sacrificial anode, reacting with MgOHCl and producing MgO and $MgCl_2$ and $H_2$, as expressed in Eq. (3.16) [65]:

$$2MgOHCl + Mg \rightarrow MgO + MgCl_2 + H_2 \quad (3.16)$$

However, it is important to consider the massive amounts of salt (thousands of tonnes) required as TES material in a CSP plant. Thus, the purification process will entail additional costs for the power plant. In this context, many studies have been conducted to identify a cost-effective way to purify salts [65, 68, 79].

Localised or pitting corrosion is a common type of corrosion mediated by chloride melts. Localised corrosion observed in TES tanks can be described as *"deep indentations (pitting corrosion) or preferential degradation of metals around the confined volume of electrolyte (crevice corrosion)"* [12]. Pitting corrosion is initiated by aggressive anion species such as $Cl^-$ or $NO_3^-$, leading to the breakdown of the protective oxide scale. This degradation process occurs via one or a combination of the following steps. First, corrosive anion species compete with the scale-forming species for adsorption onto the alloy surface. A complex soluble corrosion product forms if the aggressive anion species wins this competition. The aggressive anions diffuse through the oxide scale by occupying oxygen vacancies, negatively affecting its adhesion. Lastly, oxide scale breakdown can occur due to the adsorption of these aggressive ions to the oxide scale, which builds ups mechanical stress, in addition to the change in the concentration of cation vacancies [80, 81].

It is worth mentioning that grain boundaries (micro-cracks) and holes are the preferred sites for pits because they have lower resistance, making them susceptible to such attacks. Nevertheless, the initiation stage of the pitting may take a long time, spanning months or years, making the process unpredictable. However, once a break in a non-soluble protective scale is achieved, the pits propagate rapidly. The pits will not stop growing until the alloy finds a way to restructure a protective scale or form an insoluble corrosion product that prevents further propagation [12].

Another common corrosion feature in chloride melts is intergranular corrosion (IGC), a form of localised corrosion defined as a preferential attack along the grain boundaries. IGC is considered a type of galvanic corrosion where some heterogeneity is observed at the grain boundary region. According to a previous report [82], in the case of IGC, *"the grain boundary is considered anodic to the bulk or adjacent alloy microstructure"*. In IGC, one of the alloying elements is depleted due to its interactions with oxidising species and further precipitation at the grain boundary [12].

Interestingly, while intensive studies have been conducted to understand the corrosion resistances of different alloys in direct contact with chloride melts, the corrosion behaviours of metallic components exposed to evaporated salt species have not, to the best of our knowledge, been investigated. Therefore, part of the *Results* is dedicated to understanding better the corrosion behaviour of a vessel material composed of alloy 253MA upon exposure to evaporated salt species. In addition, corrosion behaviours

when in direct contact with chloride melts are studied and compared for the current state-of-the-art alloys, e.g., alloy 304L and a FeCrAl alloy that is a possible candidate for a Gen3 CSP.

## 3.2 Corrosion in Nitrate and Carbonate Melts

Since nitrate melts, mainly Solar Salt, are utilised as HTF and TES materials for commercial CSP plants, the corrosion behaviours in these melts have been extensively studied at both laboratory and industrial scales [12]. As discussed earlier, the corrosion of metals by salt melts depends mainly on the salt's chemistry, the gas environment, and the exposure temperature.

Nitrates spontaneously decompose at high temperatures, as shown in Eqs. (3.17) and (3.18) [39].

The thermodynamics of the nitrate melts can be described in terms of the equilibrium reached with the oxide ion and appropriate gas species [39, 53].

$$NO_3^- \leftrightharpoons NO_2^- + \frac{1}{2}O_2 \qquad (3.17)$$

$$2NO_3^- \leftrightharpoons O^{2-} + 2NO + \frac{3}{2}O_2 \qquad (3.18)$$

Besides the spontaneous decomposition of salt species, metal surfaces can act as an electron source for reduction, as illustrated in Figure 3.1, resulting in reduced anionic species, e.g., $NO_3^-$, which can take up two electrons to form $NO_2^-$ and release an $O^{2-}$ ion instead of oxygen [*cf.* Eq. (3.17)].

Alkali oxide scale formation in nitrate/carbonate melts can be summarised as follows. The first step involves the adsorption of the salt species to the metal surface. Anions are reduced by electrons to form oxide ions. Alkali cations are attracted to the reduced anions and participate in the scale formation process, given that the resulting $AMO_x$ compound cannot be dissolved in the melt. The alkali oxide scale nucleates when the reduced anions and metal cations occupy their respective sites at the metal/melt interface. Thereafter, the scale grows laterally until it covers the entire metal surface. The scale grows either outwards through metal ion transport by cationic vacancies adjacent to the adsorbed oxygen ions or inwards when oxygen ions occupy the oxygen vacancies formed at the alloy/oxide interface, as illustrated in Figure 3.1.

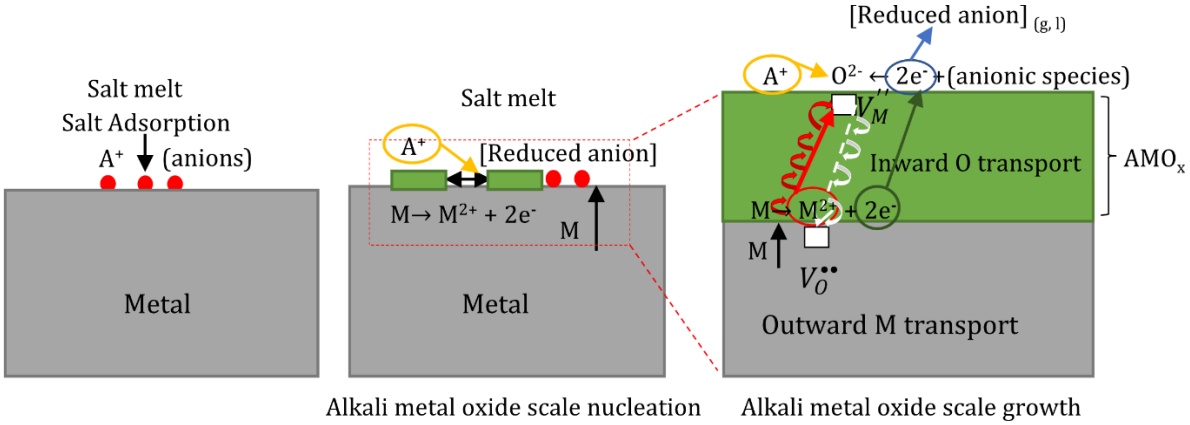


*Figure 3.1 Alkali oxide scale formation when an alloy is exposed to an alkali salt melt, where $V_O^{\bullet\bullet}$ is an oxygen vacancy, $V_M''$ is a metal vacancy, $A^+$ is an alkali cation, and $M^{n+}$ is a metal ion.*

Theoretical and experimental viewpoints have been adopted to study the corrosion potentials of the above-described melts. The extent of corrosion of an alloy in a nitrate melt depends on the acidity/basicity of the melt, which is defined by Eq. (3.6) [39].

The formation of corrosion products can be predicted using the $pO^{2-}$ of the melt, in combination with electrochemical measurements, such that the conditions for oxide scale stability and dissolution into the melt can be defined according to the exposure conditions [39].

Picard *et al.* used another approach to adjusting the activity of $O^{2-}$ using different $NO_3^-$ and $NO_2^-$ ratios to construct a predominance diagram, with iron (III) at 420°–500°C [83, 84] (Figure 3.2). In their studies, the $pO^{2-}$ diagrams predicted mainly three solid corrosion products based on the basicity of the medium. $Na_4Fe_2O_5$(s) was expected to form in strongly basic media, whereas alkali ferrites, $NaFeO_2$(s), and iron oxide, $Fe_2O_3$(s), were expected to form in moderately basic and acidic media, respectively [83, 84]. These diagrams failed to predict the potential nitride formation, which occurs at very low oxygen partial pressures beneath the oxide scale, as described in the *Results* (Section *5.1.1*).

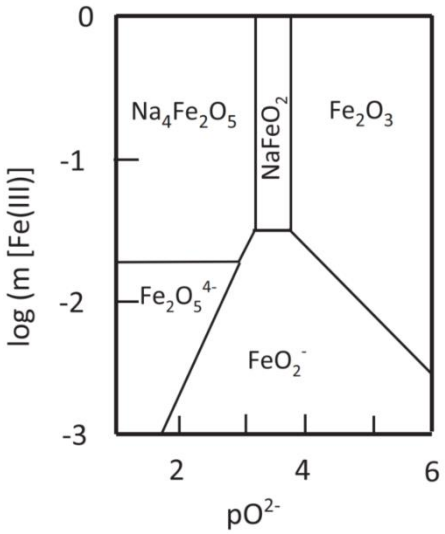


*Figure 3.2 Stability diagram for iron species in nitrate-nitrite melts as a function of basicity at 500°C [39, 84]. Source: Picard, G.S., H.M. Lefebvre, and B.L. Trémillon, 1987. Reproduced with permission from the Electrochemical Society [84].*

Various studies have employed theoretical or experimental approaches, or a combination of both, to study the corrosion performances of alloys in nitrate melts. The metallic materials investigated in nitrate melts can be classified as carbon and low-alloy steels, stainless steel, and FeCrAl alloys [9, 12, 69, 85-96].

The main insoluble corrosion products formed when in contact with nitrate melts (and related to this thesis work) are summarised as follows: an inner scale of $(Fe,Cr)_3O_4$ [89], or an outer $NaFeO_2$ scale and inner $Fe_3O_4$, $Fe_2O_3$ scales [9, 92]. The corrosion products detected depend on the chemical composition of the alloy and the exposure conditions used.

Another class of potential candidates for Gen3 CSP plants are carbonate salt mixtures. However, corrosion in this melt environment has not been studied as intensively as for nitrate melts. Nevertheless, corrosion behaviours have been investigated for metals used in molten carbonate fuel cell (MCFC) applications since carbonate salts are used as electrolytes. Following a temperature increase, the carbonate salt decomposes into the cationic alkali species ($A^+$), oxyanions, and $CO_2$. The basicity of the melts, measured according to Eq. (3.19), depends on the equilibrium with the oxide ion and $CO_2$ [39]:

$$A_2CO_3 \leftrightharpoons 2A^+ + O^{2-} + CO_2 \quad (3.19)$$

Since carbonate oxide-melt interactions are acid-base reactions, their products are expected to be similar to those produced in nitrate melts [39]. The corrosion products' stability mainly depends upon the salt's chemistry, acidic/basic fluxing in the melts, and temperature [97].

Oxygen fluxing has been discussed extensively among the different corrosion mechanisms for salt melts. The fluxing process in an oxidising environment can be defined as accelerated corrosion through the dissolution and re-precipitation of metal oxides into the salt melts. The oxide fluxing process depends on the metal/metal oxide and the salt basicity/acidity [98]. The diffusion processes in liquid salts are very rapid compared to solid-state diffusion in an alloy or oxide. The activation energies for the dissolution of ionic species into a melt are generally lower than those for the evaporation of molecular species into a gas stream.

In the present study, alkali carbonates in contact with alloys have been investigated under $CO_2$ gas, in contrast to the cases of the alkali nitrates, which were operated in air. Conducting carbonate melt exposures under $CO_2$ means that we have two sources of $CO_2$: one that arises from the spontaneous decomposition of alkali carbonate at the metal surface and the other in the form of $CO_2$ dissolved into the melt from the gas phase. Both sources of $CO_2$ can be reduced by alloy species to form carbon monoxide (gas evolution), as shown in Eq. (3.20), or even inwards diffusing carbon at the metal/oxide interface, which can cause carburisation underneath the oxide zone [Eq. (3.20)].

$$2M + nCO_2 \longrightarrow 2M^{n+} + nCO(g) + nO^{2-} \text{ (gas evolution) (3.20)}$$

or

$$4M + nCO_2 \longrightarrow 4M^{n+} + nC + 2nO^{2-} \text{ (carburising) (3.21)}$$

Carburisation involves an internal corrosion attack when a scale-forming alloy component such as chromium is selectively bound to carbon in the alloy interior. Internal carbide precipitation suppresses the migration of, for example, chromium to the oxide/metal interface to form an oxide scale. Initial internal carburisation occurs as precipitates along the grain boundaries. Carburisation is undesirable because it compromises the alloy's chemistry and changes its mechanical integrity [99, 100].

Many studies have been dedicated to understanding the corrosion of metallic materials in carbonate melts under various conditions [98, 101-109]. The primary corrosion products detected relevant to this thesis are: (i) insoluble corrosion products, such as $LiFeO_2$ [98], $LiCrO_2$, and $FeCr_2O_4$ [40]. In addition to $Al_2O_3$, $Fe_2O_3$ or $NiFe_2O_4$ and $CrFe_2O_4$ [110]; and (ii) soluble corrosion products, such as $K_2CrO_4$ [40]. The types of corrosion products detected depend on the alloy's chemistry and the type of exposure [98, 101-109].

All the publications to date concerning alkali carbonate melts point out that chromia-forming alloys at high operating temperatures do not resist the rapid formation of an alkali oxide scale and internal attack [111]. In stark contrast, alumina-forming alloys show superior corrosion resistance to molten carbonate attack through slow growth of an alkali aluminate scale and limited or no internal carburisation.

In summary, previous studies on the corrosion resistance of chromia-forming stainless steel alloys highlight the need to identify alternative alloys or to utilise corrosion mitigation methods for the metallic components considered for use in Gen3 CSP plants [39, 85, 110-115]. Therefore, in this thesis, the corrosion resistance levels of several FeCrAl and FeNiCrAl alloys are studied as possible candidates for Gen3 CSP and compared to the state-of-the-art chromia-forming alloys, e.g., alloy 304L. Similar to research on corrosion caused by chloride melts, data on evaporated carbonate corrosion in conjunction with thermal storage tank materials are lacking. To remedy this, a systematic study is conducted in this work to understand the corrosion behaviour of an alloy 253MA vessel material exposed to evaporated alkali carbonates.

# 4 Experimental Layout

The flow chart depicted in Figure 4.1 provides an overview of the experimental work conducted in this thesis. The figure shows that three primary studies have been conducted. The following sections describe the salts, alloys, experimental set-ups, and analytical methods.

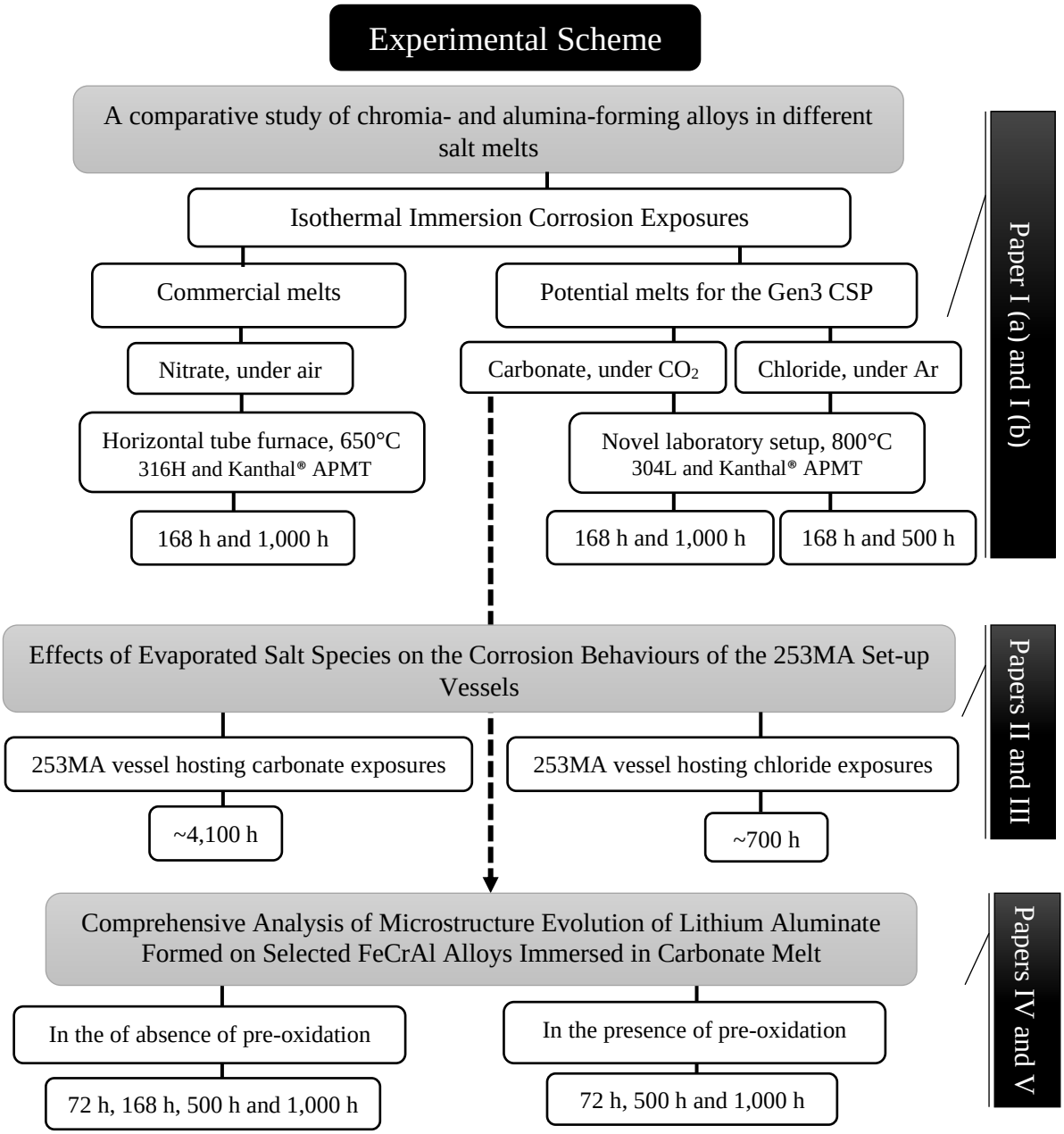


*Figure 4.1 Flow chart illustrating the experimental layout for the thesis.*

## 4.1 Materials

### *4.1.1 Salt Melts*

As described in Chapter 1, the eutectic salt melts were selected based on their favourable thermo-physical properties and cost, as well as other factors that recommend their potential usage in commercial CSP plants [15].

In this work, the following eutectic salts were chosen: a binary nitrate salt mixture, which is also known as Solar Salt (60 wt% $NaNO_3$, 40 wt% $KNO_3$); a ternary carbonate salt (32.1 wt% $Li_2CO_3$, 33.4 wt% $Na_2CO_3$, 34.5 wt% $K_2CO_3$); and a binary chloride mixture (64.4 wt% KCl, 35.6 wt% $MgCl_2$). The thermo-physical properties of these salt mixtures have been discussed in several articles [58, 116, 117].

The salts were purchased from the following suppliers: $NaNO_3$ (Alfa Aesar, 99.0% pure); $KNO_3$ (Alfa Aesar, 99.0%); $Li_2CO_3$ (VWR Chemicals, 99.0%); $Na_2CO_3$ (EMSURE, anhydrous, 99.9%); $K_2CO_3$ (ThermoFisher Scientific, 99.8%); KCl (Alfa Aesar, 99.0%); and $MgCl_2$ (Alfa Aesar, anhydrous, 99.0%). Since impurities play a vital role in the corrosion process [12, 54, 117, 118], the concentrations of impurities in each salt are listed in Table 4.1 The tabulated impurity values were obtained from the chemical datasheets for the salts.

*Table 4.1 Concentrations of impurities in the salts used, as reported by the suppliers.*

| Salt | Moisture | Chloride ($Cl^-$) | Phosphate ($PO_4^{3-}$) | Silicate (as $SiO_2$) | Total Sulphur (as $SO_4^{2-}$) | Calcium ($Ca^{2+}$) | Magnesium ($Mg^{2+}$) | Others |
|---|---|---|---|---|---|---|---|---|
| $NaNO_3$ | Detected | 0.0006% | 1.2 ppm | - | 0.0020% | 0.0008% | 0.0005% | Heavy metals (e.g., $Pb^{2+/4+}$) and $Fe^{2+/3+}$, 1 ppm for each |
| $KNO_3$ | Detected | 0.002% | 5 ppm | - | 0.003% | 0.005% | 0.002% | Heavy metals 5 ppm, $Fe^{2+/3+}$ 3 ppm, $IO_3^-$ 5 ppm, $NO_2$ 0.001%, $Na^+$ 0.005% |
| $Li_2CO_3$ | Detected | ≤0.02% | - | - | ≤ 0.05% | 0.01% | | Heavy metals (e.g., $Pb^{2+/4+}$) ≤20 ppm, $Fe^{2+/3+}$ 3 ppm |
| $Na_2CO_3$ | Loss on drying ≤1.0% | ≤0.002% | ≤ 0.001% | ≤ 0.002% | ≤ 0.005% | ≤0.005% | ≤ 0.0005% | Heavy metals (e.g., $Pb^{2+/4+}$), $Fe^{2+/3+}$, $N^{3-/3+/5+}$, $Al^{3+}$, $K^+$ |
| $K_2CO_3$ | 0.113% | KCl, 0.0043% | - | - | $K_2SO_4$, 12 ppm | - | - | KOH 0.106%, $Na^+$ 0.20%, $Fe^{2+/3+}$ 0.40 ppm |
| KCl | Detected | Chlorate and Nitrate ≤0.003% | ≤5 ppm | | ≤0.001% | ≤0.002% | ≤0.001% | $Ba^{2+}$ ≥ 0.001%, $Br^-$ ≤0.01%, $I^-$ ≤ 0.002%, $Fe^{2+/3+}$ ≤3 ppm, $Na^+$ ≤0.005%, Heavy metals (e.g., $Pb^{2+/4+}$) ≤5 ppm |
| $MgCl_2$ | Detected, 0.97% | NaCl 36 ppm, $CaCl_2$ 47 ppm | - | - | - | - | - | MgO (100 ppm) |

The experiments in this study were conducted at about 100°C above the anticipated operational temperature in thermal storage facilities for two reasons. First, when wetted with salt melts, the metallic parts in a large CSP plant experience temporary overheating. Second, the accelerated corrosion provides relevant results within the time-frame of this study.

The eutectic mixtures were prepared according to the following procedure. In 100-g batches, the salts were weighed and mixed to the correct ratio, then ground using a mortar and pestle. Then, the salts were furnace-dried at 110°C for at least 24 h.

Since the water content is critical for the corrosion experiments, chloride mixtures were prepared using an Ar purification process to reduce the moisture content of the salts [24, 30].

Based on previous studies [24, 30], the chloride mixtures were purified using a step-wise thermal purification process. The purification process starts with drying the salt mixture at 110°C for at least 5 hours under an Ar flow. Then, the temperature is raised to 200°C and held for a 2-hour dwell time. The temperature is increased again to 300°C for 2 hours. Thereafter, the set-up is allowed to cool to room temperature under an Ar flow. In the final step, an alloy sample is dipped into a salt-filled crucible before initialising the corrosion experiment. The vessels that contain the salt-filled crucible are purged with Ar for

12 h, then heated to 120°C for at least 12 h. Lastly, the temperature is raised to 750°C and held for 1 hour before the corrosion experiment starts, as described later in this chapter.

### *4.1.2 Alloys*

Table 4.2 summarises the nominal compositions of the alloys investigated.

The following procedure describes how the samples were prepared. First, metal coupons with initial dimensions (15×15×2) mm were ground using up to 1200-grit SiC abrasive paper, then polished with suspensions that contained 3-µm and 1-µm diamonds until a mirror-like finish was obtained. The polished samples were cleaned in three steps with deionised water, acetone, and ethanol using an ultrasonic bath at room temperature. Finally, the coupons were dried using an air gun and dipped into salt-filled alumina crucibles.

*Table 4.2 Nominal alloy compositions (in weight percent). RE refers to reactive elements, e.g., Y, Zr, Ce.*

| **Alloy (publication)** | **Fe** | **Ni** | **Cr** | **Al** | **Si** | **Mn** | **Mo** | **Others** |
|---|---|---|---|---|---|---|---|---|
| 316H [**Paper I** (a and b)] | balance | 11.5 | 17 | - | 0.6 | 1.5 | 2.1 | C 0.05 |
| 304L [**Paper I** (a and b)] | balance | 9.5 | 18.5 | - | 0.4 | 1.3 | - | C 0.02 |
| Kanthal® APMT [**Paper I (a** and **b), Papers IV** and **V**] | balance | - | 21 | - | 0.7 | 0.4 | 3 | RE; C 0.08 |
| 253MA [**Paper II** and **III**] | balance | 10.6 | 20.9 | - | ≤1.97 | ≤0.55 | - | C 0.08; P; S; Ce; V |
| Kanthal® AF [**Papers IV** and **V**] | balance | - | 21 | 5.3 | 0.7 | X | - | RE; C 0.08 |
| Kanthal® EF101 [**Papers IV** and **V**] | balance | <0.5 | 11–14 | 3.2–4.2 | 1.2 | <0.7 | - | RE; C 0.08 |
| Kanthal® EF100 [**Papers IV** and **V**] | balance | <0.5 | 9.5–13 | 3.8–4.2 | <0.5 | <0.7 | - | RE; C 0.08 |
| Nikrothal® PM58 [**Paper IV**] | 18 | balance | 19 | 5 | 0.4 | - | - | RE |

## 4.2 Experimental Set-up

In this work, two set-ups were used. Initially, a horizontal tube furnace was utilised for corrosion exposures with the nitrate melts. Subsequently, a novel vertical set-up was designed and implemented for the exposures involving carbonate and chloride melts. Table 4.3 summarises the experimental parameters and corrosion conditions in the different environments.

*Table 4.3 A summary of eutectic melting points, the decomposition temperature of different salt mixtures, and experimental parameters for the corrosion experiments.*

| Eutectic salt mixture | *Nitrates* (60 wt% $NaNO_3$, 40 wt% $KNO_3$) | *Carbonates* (32.1 wt% $Li_2CO_3$, 33.4 wt% $Na_2CO_3$, 34.5 wt% $K_2CO_3$) | *Chlorides* (65 wt% KCl, 35% wt% $MgCl_2$) |
|---|---|---|---|
| $T_{eutectic}$ (°C) | 230 [15] | 398 [119] | 423 [120] |
| $T_{max}$ (°C) | 530–565 [15] | >650* [117] | >800 [120] |
| Gas | filtered air | $CO_2$ | argon |
| Exposure temperature | 650°C (isothermal) (72 h cyclic refilling of the salt) [**Paper I (a and b)**] | 800°C (isothermal) (336 h cyclic refilling of the salt) [**Paper I (a and b)**, **Papers IV** and **V**]) | 800°C (isothermal) (336 h cyclic refilling of the salt) [**Paper I (a and b)**]) |
| Total exposure time | 168 h & 1,000 h [**Paper I (a and b)**] | 168 h & 1000 h [**Paper I (a and b)**] 72 h, 168 h, 500 h and 1,000 h [**Papers IV** and **V**] | 168 & 500 h [**Paper I (a and b)**] |

** The decomposition temperature varies with the atmosphere. The actual temperatures were 1,000°C, 700°C and 670°C for the $CO_2$, argon, and air exposures, respectively [117].*

## 4.3 Corrosion Experiments

### *4.3.1 Immersed Isothermal Corrosion Experiments*

The schematic in Figure 4.2 describes the first set-up employed. The horizontal tube furnace was used for the corrosion experiments conducted in nitrate melts and was equipped with a quartz tube (50-mm diameter). The exposures were conducted isothermally at 650°C±5°C with filtered air at a 20 ml/min flow rate.

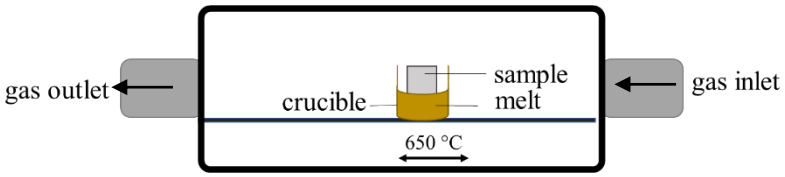


*Figure 4.2 Experimental set-up for the horizontal tube furnace nitrate exposures.*

Among the reasons for building a new set-up was the partial immersion of the coupons in the melts in the horizontal tube furnace. This novel laboratory vertical set-up was designed for complete immersion experiments. A top-loader furnace (Nabertherm Top 60 model) was purchased and re-designed in the workshop by Esa Väänänen to be suitable for carbonate and chloride exposures in controlled gas environments. The detailed procedure for designing and building the vertical set-up is provided in **Paper I (b)** [121], and a schematic of the cylinder vessel is shown in Figure 4.3. The corrosion experiments were conducted isothermally at 800°C±5°C. The temperature was calibrated at the crucibles' lowest point, with a gas (Ar or $CO_2$) at a flow rate of 50 ml/min for each vessel. Each exposure was carried out at least twice to guarantee reproducibility.

The novel laboratory set-up is superior to the tube furnace because it allows the testing of six coupons in each vessel and provides duplicate samples. The new set-up allows the removal of coupons directly from the melts before they solidify [**Paper I (b)**, Section A5]. Otherwise, the solidified melts must be washed off the tested coupons, and the washing procedure changes the alloy surface chemistry. One of the duplicate samples goes through washing for mass change measurements according to the standard methods [122] and as followed and described in the literature [23, 87, 123-127]. The second sample is dedicated to the cross-section analyses in unwashed form.

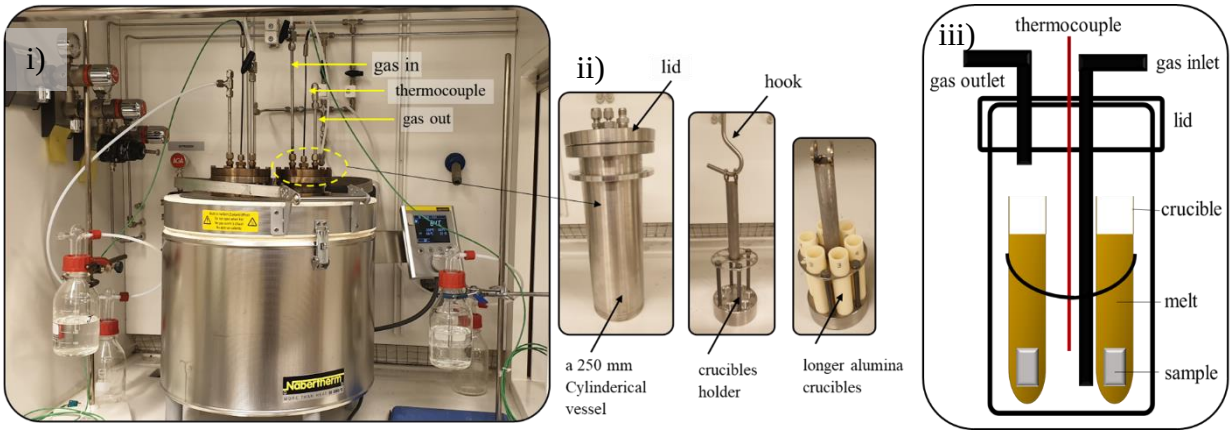


*Figure 4.3 i) Novel laboratory vertical set-up built for the carbonate and chloride exposures. ii) Cylindrical vessel components. iii) Schematic of the cylindrical vessel. Reproduced with permission from Elsevier [121].*

### 4.3.2 *Specimens Taken from Alloy 253MA "Vessel Material"*

As described in Section 4.3.1, a new set-up was designed to mimic the conditions in a hot TES tank, even though the main focus of our studies was on corrosion that occurs in direct contact with salt melts. The observed damage to the alloy 253MA vessels that hosted the immersion isothermal corrosion experiments prompted us to decommission the vessels. Analysing the corroded vessels provided another perspective on the compatibility between the melts and metallic components, namely the effects of evaporated species on metals following a temperature gradient.

Vessels that hosted exposures to carbonate and chloride melts were chosen for this investigation. The 253MA vessel material was selected due to its high strength and improved corrosion resistance in air at high temperatures due to the formation of a protective chromia scale that was supported by silicon and cerium additions [128]. Moreover, having the 253MA material readily available with a 5-mm wall thickness made it a suitable choice for our prototype set-up.

Figure 4.4a illustrates the furnace set-up, which consists of three heating elements embedded in the insulating wall material at three different heights. The lid was re-designed to secure the placement of two identical alloy 253MA cylindrical vessels. Each vessel extended 23 cm into the furnace and was equipped with a lid fitted with a gas inlet, gas outlet, and thermocouple inlet. The gas inlet was positioned at the lowest point of the vessel. In addition, a retractable stand was placed to support six long alumina crucibles in each vessel, with each crucible being loaded with approximately 10 g of the desired eutectic mixture. This ensured that the set-up was complete and ready for operation.
Alumina crucibles are the only molten salt reservoirs into which alloy sample coupons are immersed during experimentation. The alloy 253MA vessel is not in contact with the melt itself. Alloy 253MA has been developed and optimised to provide superior strength and resilience in high-temperature corrosive environments due to its high chromium content, which forms a protective chromia scale. A comparative study of stainless steels that was conducted to evaluate the performance of alloy 253MA concluded that it

performs excellently in $CO_2$ at high temperatures during isothermal experiments and performs adequately during thermal cycling [129].

It has been predicted that chromia formation is not very protective in a molten salt environment, e.g., in the presence of alkali carbonates [107]. To improve the corrosion resistance of the vessel, a powder pack diffusion coating was applied to create an aluminium reservoir. This coating was applied using the recipe published by Oskay *et al.* [130], with aluminium metal powder as the diffusion element, $NH_4Cl$ as the activator, and $Al_2O_3$ as filler. The diffusion coating was prepared in two steps at high temperatures (900°C) under argon. It is expected to form aluminium-rich inter-metallic layers, which act as reservoirs for alumina formation on the alloy surface, thereby providing a corrosion barrier. The coating was applied by filling the vessel (up to 14 cm) with a powder mixture of 96.5 wt% $Al_2O_3$, 3 wt% Al, and 0.5 wt% $NH_4Cl$. The vessel was then purged with argon for several hours before heating to 500°C for 1 h, then raising the temperature to 900°C, followed by maintenance of this temperature level for 3 h. Then, the powder was carefully removed, and the vessel was pre-oxidised at 900°C for 4 h in air.

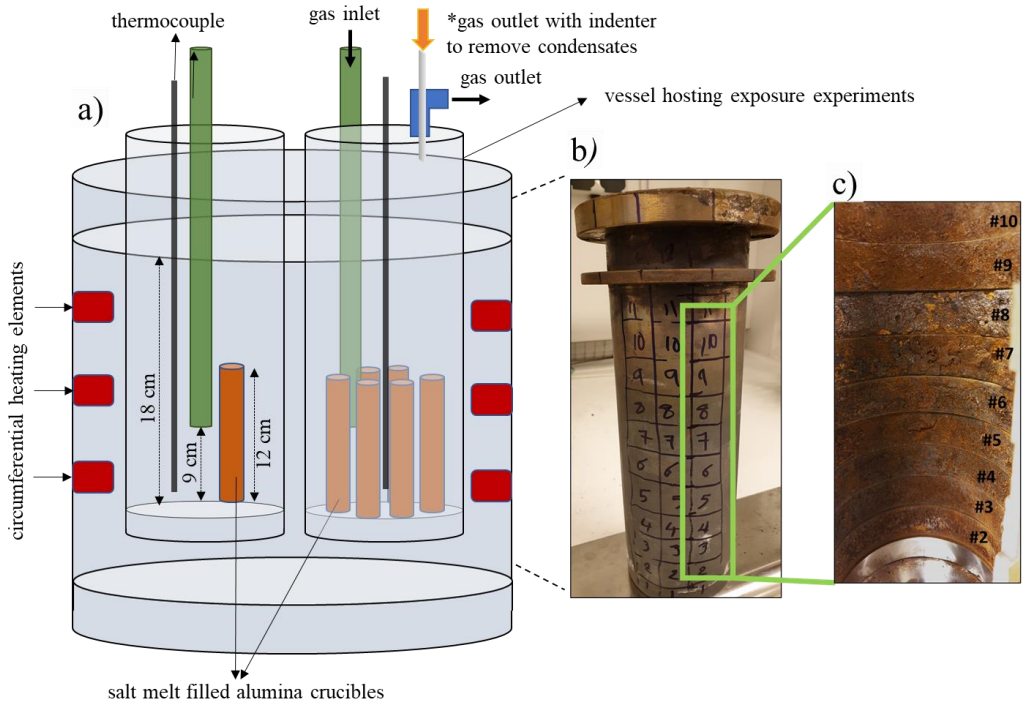


*Figure 4.4 a) Schematic illustration of the experimental set-up showing two vessels hosting six crucibles each. b) The vessel before and after partitioning. c) The vessel interior was scrubbed before decommissioning, the brushed corrosion products were collected for analysis, and the vessel was sectioned into horizontal rings for investigation.*
**Gas outlet was modified only for the vessels hosting chloride exposures.*

The inward diffusion of aluminium and the outward diffusion of iron determine the chemical composition of the aluminide layers. When oxidised, aluminium diffuses outwards to create an alumina scale that protects the 253MA samples.

The cover gas, $CO_2$, was selected for these exposures based on Le Châtelier's principle [131], which states that the $CO_2$-rich atmosphere suppresses the decomposition of carbonate salts. It is important to emphasise here that there was no direct contact between the salt and vessel material. Thus, the corrosion was exclusively caused by the $CO_2$ and evaporating alkali carbonate species.

The interior temperature of the vessels was calibrated to 800°C at the position where normally the coupon specimens are located during the immersion tests. However, a temperature gradient was detected due to the positioning of the heating elements in the furnace set-up. The temperature in the lowest vessel segment (#2) was significantly higher (by ~150°C) than the temperature in the highest vessel segment (#10).

A diary of the vessel life cycle was documented and is summarised in Table 4.4 (for a detailed description, see **Paper II**).

The vessel was decommissioned after hosting the carbonate experiments for more than 4,000 hours. It was then cut into ten sections using a water-cooled diamond blade. These sections were numbered from 1 (the bottom, which was the hottest zone) to 10 (the top, which was the coldest zone). Before the partitioning process began, the vessel's interior was brushed with a four-row steel wire brush. Afterwards, the vessel was cut into rings, with each ring representing one of the ten marked zones. Finally, coupons with dimensions of 20×20×5 mm were cut from each ring (see Figure 4.4, b and c).

*Table 4.4 Life-cycle of the investigated alloy 253MA vessel after >4,000 h of discontinuous operation hosting the $(Li,Na,K)_2CO_3$ corrosion experiments.*

| **Operational Conditions** / **Process** | **Duration (h)** | **Reheating Cycle (Every 336 h)** | **Duration of Vessel Opening (Pouring the melt off, Air, 500°C) (min)** |
|---|---|---|---|
| Aluminium-diffusion coating | | | |
| Step I (at 500°C), Ar | 1 | - | - |
| Step II (at 900°C), Ar | 3 | - | - |
| Pre-oxidation step (at 900°C), air | 24 | - | - |
| Exposures to alkali carbonate melts ($CO_2$, 800°C) | | | |
| Experiment no. 1 | 72 | - | 75 |
| Experiment no. 2 | 500 | Once | 75 |
| Experiment no. 3 | 500 | Once | 60 |
| Experiment no. 4 | 168 | - | 45 |
| Experiment no. 5 | 1,000 | Thrice | 45 |
| Experiment no. 6 | 72 | - | 50 |
| Experiment no. 7 | 1,000 | Thrice | 45 |
| Experiment no. 8 | 168 | - | 60 |
| Experiment no. 9 | 72 | - | 60 |
| Experiment no. 10 | 72 | - | 55 |
| Experiment no. 11 | 500 | Once | 60 |

The vessels that hosted the carbonate and chloride corrosion experiments had similar set-ups and decommissioning processes. However, no coating was applied to the alloy 253MA vessels deployed for the chloride exposures. Instead, a pre-oxidation step was implemented for 24 h at 900°C under air prior to the

exposure being conducted. A modification to the gas outlet line was another difference introduced into the vessel set-up in such an environment. As mentioned earlier, there is a temperature gradient along the vessel wall, which means that the vessel lid has a lower temperature. In Table 4.3, the KCl-$MgCl_2$ mixture shows a relatively high eutectic melting temperature, leading to salt condensation at the vessel lid and clogging of the gas outlet. Therefore, a movable anti-clogging metal rod was installed within the gas outlet line that could be mechanically adjusted frequently to push down any accumulations of condensed salt species (see Figure 4.4a).

Unlike the long total exposure time in the carbonate-hosting vessels, which operated for more than 4,100 h, the chloride-hosting vessels were decommissioned after only 700 h, with two rounds of vessel venting at 600°C. In addition, as discussed in Section 4.1.1, the vessels were used for the $MgCl_2$-KCl salt purification procedure documented and listed in Table 4.5, which illustrates the detailed lifecycle of the investigated alloy 253MA vessels.

*Table 4.5 Lifecycle of the investigated 253MA vessel after ~700 h of discontinuous operation with $MgCl_2$-KCl corrosion exposures.*

| **Operational Conditions** / **Process** | **Temperature (**°C) | **Duration** | **Atmosphere** |
|---|---|---|---|
| Prior to chloride melt exposure | | | |
| Pre-oxidation step (at 900°C), air | | 24 h | - |
| Exposures to KCl-$MgCl_2$ melt (Ar, 800°C) | | | |
| ***Experiment no. 1*** | | | |
| Salt purification | 110 | 24 h | Ar |
| | 200 | 2 h | |
| | 300 | 2 h | |
| | 750 | 1 h | |
| Exposure | 800 | 168 h (paused after 96 h) | |
| **Evaporated salts clogging the gas outlet after 96 h, vessel opening at room temperature, cleaning up the exhaust line, drying procedure** | | | |
| Exposure | 800 | 168 h (resumed after 96 h) | Ar |
| Vessel Opening (Pouring the Melt Out) | 600 | ~70 min. | Air |
| The vessel was cleaned and brushed after the experiment | | | |
| ***Experiment no. 2*** | | | |
| Salt purification | 110 | 24 h | Ar |
| | 200 | 2 h | |
| | 300 | 2 h | |
| | 750 | 1 h | |
| Exposure | 800 | 336 h (paused after 96 h) | |
| Vessel Opening at room temperature, refilling crucibles (half-filled) with new dried salts, purging under Ar for 24 h at 110°C, then salt purification | | | |
| Exposure continuation | 800 | 168 h | |
| Vessel Opening (Pouring the melt out) | 600 | ~75 min. | Air |

## 4.4 Analytical Methods

As mentioned earlier, high-temperature corrosion of metallic materials in contact with molten salts is highly complex. Different analytical techniques have been employed to understand better the corrosion behaviours of the selected alloys by identifying key phases. Duplicate samples allowed post-exposure analyses that required different sample preparation methods (Figure 4.5).

One sample was washed for mass change measurements and the x-ray diffraction (XRD) analysis. A duplicate sample was not rinsed with water and was used for the cross-section preparation, including salt remnants.

After completion of the exposure experiment, the "unwashed" sample was extracted from the crucible filled with molten salt using the following procedure. After the required exposure, the temperature was reduced to 50°C above the mixture's eutectic melting point. This enabled the pouring off of salts from the coupons while in their molten state. Only a small amount of the salts remained on the sample surface. Afterwards, the salts were collected for further analysis.

Following the standard cleaning method, the duplicate sample was washed to remove all residual salts and solvable corrosion products from the sample surface [122]. At room temperature, the samples were sonicated and brushed softly until the cleaning was completed. If any salt remained, the sonication was interrupted, and the coupon was brushed to remove the salt. Thereafter, the sonication procedure was re-started to ensure that the salts were dissolved entirely. It is worth noting that the results involving washed samples, such as the XRD analysis and weight change values, need to be considered cautiously. Weight change measurements were not considered reliable data for corrosion evaluation but rather supplementary data that showed indications in the context of other characterisation techniques.

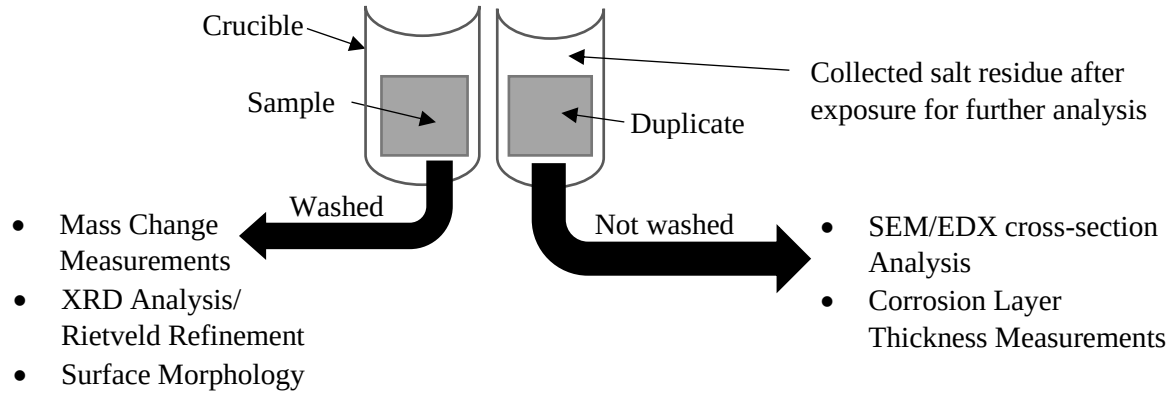


*Figure 4.5 Schematic illustration showing the procedures used for sample evaluation after the exposures.*

For the corrosion evaluations of the tested samples, different analyses were conducted. In this work, the characterisation techniques are classified into surface analysis, metallographic analyses, and thermodynamic calculations.

### 4.4.1 Surface Analysis

X-ray diffraction (XRD) is a non-destructive analytical technique that allows for the phase identification of a crystalline sample, in addition to providing information about lattice parameters and, to some extent, granularity. The XRD technique is based on constructive interference of a mono-chromatic and coherent x-ray beam with the sample, where interaction occurs between the x-rays and the sample's crystal structure. X-rays are diffracted when conditions satisfy Bragg's Law, as stated in Eq. (4.1) (see Figure 4.6) [132].

$$n\lambda = 2d_{hkl}\, sin\theta \quad (4.1)$$

where *n* is the order of "reflection" (an integer number), $\lambda$ is the wavelength of the x-rays, $d_{hkl}$ is the inter-planar spacing of the lattice planes, and $\theta$ is the angle between the diffracted beam and the crystal plane. Reflection is used as a simplified concept of the scattering process.

XRD analysis is used to identify the crystalline corrosion products that are formed. In addition to providing information about crystal structures, XRD analysis is the only tool used in this study that is capable of detecting Li-containing corrosion products.

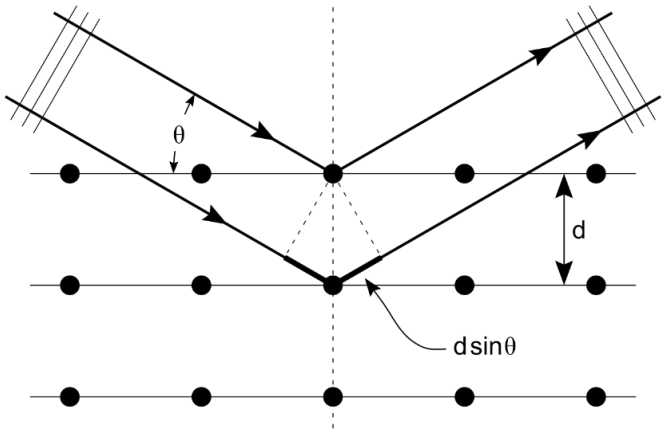


*Figure 4.6 Schematic illustration of Braggs' law. An incident beam is "reflected" by a crystal plane at an angle θ. Source: Bragg, W.H.S.,* X-rays and crystal structure *ed. L.S. Bragg, 1915 [133].*

The Siemens D5000 grazing-incidence XRD equipped with a Cu source, a secondary Si mono-chromator, and a point detector was employed to analyse the corrosion products. The grazing-incidence XRD technique uses a low incidence angle of the x-ray beam, limiting the penetration to the bulk material and, thereby, identifying the crystalline phases in thin oxide scales.

The flow chart illustrated in Figure 4.1 shows an interesting observation regarding the α-$LiAlO_2$ to γ-$LiAlO_2$ phase transition that was detected for Kanthal APMT exposed to a carbonate melt at 800°C. To understand this phase transformation, it is essential to quantify these crystalline phases on the sample surface with respect to the exposure time. The Rietveld refinement technique was used to quantify the crystalline phase in the materials by implementing their XRD patterns.

The Rietveld refinement analysis is based on comparing the XRD patterns of a sample with a calculated diffraction pattern based on crystallographic data, such as the crystalline system and atomic positions [134]. In the Rietveld method, *refinement* refers to the process of fine-tuning the model of cell parameters and relative intensities used to re-calculate a diffraction pattern approaching the observed values. In this work, the Rietveld refinement is more complex for a metal sample with a duplex oxide scale than for a homogeneous powder sample. In the samples studied, a coupon is covered by a thin oxide scale ($\alpha$-$LiAlO_2$), with a randomly growing crystal on top of the formed oxide scale ($\gamma$-$LiAlO_2$). In addition to the signals detected from the bulk, $\gamma$-$LiAlO_2$ crystals randomly nucleate and grow over the $\alpha$-$LiAlO_2$. A collaboration with Dr Michal Strach (Chalmers Materials Analysis Laboratory, Physics Department) allowed us to interpret the quantification results and their errors accurately. The Rietveld refinement method with the acquired XRD patterns was employed using the TOPAS ver. 6 software to calculate the $\alpha/\gamma$-$LiAlO_2$ phase fraction ratios. Crystal structures of $\alpha$- and $\gamma$-$LiAlO_2$ crystals were acquired from the Springer Materials Database [135, 136]. More details about the parameters used in this method can be found in **Paper IV**.

### *4.4.2 Metallographic Analysis*

Scanning electron microscopy (SEM) was used to investigate the microstructures of corroded samples by probing the surface with a focussed electron beam, which interacts with targets and generates signals that are translated further to produce an image or a spectrum. Among these signals: (i) secondary electrons (SE) are emitted upon electron interactions close to the sample surface, depending on the acceleration voltage. Accordingly, they are generally used to reveal the surface topography; and (ii) back-scattered electrons (BSE) are often emitted vertically to the normal surface. The quantity of the generated BSE is influenced by the sample's density and chemical composition, apart from the operating parameters, such as the accelerating voltage of the electrons. For instance, phases with higher atomic numbers appear brighter in the BSE image than phases with lower atomic numbers (Z-contrast) [137].

As illustrated in Figure 4.5, washed samples were subjected to surface morphology inspection. At the same time, unwashed samples were used to investigate cross-sections. The cross-section preparation procedure for the samples was as follows: (i) samples underwent dry cutting with a low-speed diamond saw and were then sputter-coated with gold; (ii) three methods were used before the cross-sectional microscopy analysis: cold embedding in epoxy resin, hot mounting in Bakelite or utilising broad ion beam (BIB) milling with the Leica TIC 3X instrument; and (iii) before BIB milling, a thin polished silicon wafer was applied to the sample's surface to protect the oxide scale. Details of the milling parameters are provided in **Paper I (b)**.

The surface and cross-section inspections were conducted using the JEOL JSM-7800F Prime or Phenom ProX Desktop SEM equipped with an energy-dispersive x-ray (EDX) detector. The EDX spectra were collected using an electron beam with an accelerating voltage of 15 kV.

### *4.4.3 Thermodynamic Calculations*

For **Papers I (a)**, **II** and **III**, Associate Professor Christine Geers utilised the Thermo-Calc Software and FactSage to calculate single-point equilibria and the Gibbs free energy. The Thermo-Calc software package and the TCS Steels and Fe-alloys database (TCFE) ver. 9.1 [138]. Factsage 7.3 databases were used to generate the data [139].

# 5 Results and Discussion

Chapter 1 discussed the necessity of utilising new metallic materials for heat storage tanks compatible with molten salts for next-generation CSP plants.

Despite the numerous studies that have investigated different alloys in contact with salt melts, as presented in Chapter 3, there is a lack of studies comparing the extent to which potential metallic materials and currently employed materials interact with different melts. The current state-of-the-art system involves the use of molten nitrates as HTF/TES operating at temperatures of <565°C. Various chromia-forming alloys are employed in the currently operating CSP plants. The SunShot initiative launched by the US DOE proposed using molten carbonates or chlorides for Gen3-CSP. Therefore, the first part of this chapter is dedicated to a comparative study of the corrosion behaviours of chromia-forming alloys and alumina-forming alloys when in direct contact with currently utilised and candidate salt melts.

The second part deviates from the classical approach to corrosion studies conducted in direct contact with molten salts. Despite the many publications on the degradation of alloys immersed in salt melts, there is a lack of knowledge regarding the behaviours of metals that are located above the molten salts in a hot storage tank. Part II of this chapter focuses on the corrosion resistance of alloy 253MA when exposed to evaporated salt species.

While conducting our comparative study (Part I), a phase transformation of the growing alkali oxides was observed on selected AFA in contact with the carbonate melt. This interesting finding motivated us to pursue a detailed study to understand this behaviour better. Thus, in the third part, a holistic-comprehensive approach is adopted to study the microstructure and crystallographic evolution of lithium aluminate formed on AFA that is in contact with $(Li,Na,K)_2CO_3$.

Figure 5.1 shows a schematic illustration of the sections of a CSP plant that are of interest in this work.

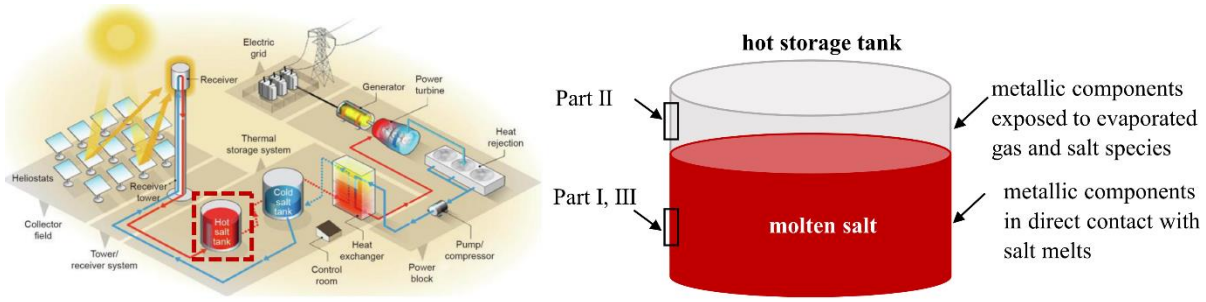


*Figure 5.1 Schematic illustration of a hot storage tank in a concentrated solar power plant, highlighting the sections in focus in this thesis. Source of the image on the left, schematic illustration of concentrated solar power plant components: US Department of Energy Report: The Year of Concentrating Solar Power, DOE/EE-1101, May 2014 [15, 17].*

## 5.1 Part I: Comparative Study of the Corrosion Performances of Chromia- and Alumina-Forming Alloys in Three Different Salt Melts

In this study, an alumina-forming alloy (Kanthal® APMT) and chromia-forming alloys (316H/304L) were immersed in nitrate, carbonate, and chloride melts. As discussed in Chapter 3, some corrosion products might dissolve in water during the coupon rinsing procedure. Consequently, the corrosion of the tested alloys was evaluated based on corrosion zone thickness. Using this method, the performances of materials are distinguished by three main features: outward growing zone; inward growing zone; and internal oxidation, see (Figure 5.2).

In Figure 5.2, significant differences in corrosion behaviour are evident between the chromia-forming and alumina-forming alloys, particularly with respect to the internal attack.

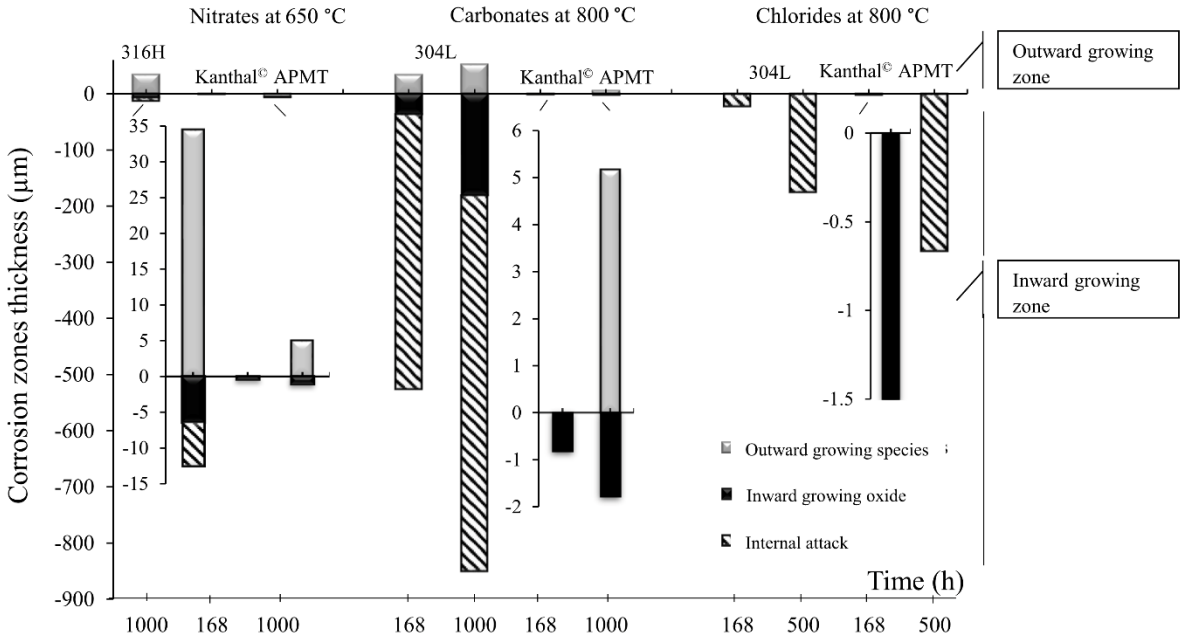


*Figure 5.2 Comparisons of all the corrosion layer thickness measurements listed in Paper I. The differences between the outward-growing and inward-growing zones are distinguished. The horizontal axis is placed at the apparent initial material surface. Reproduced with permission from Elsevier* [107].

To illustrate the severity of the corrosion attack, the results shown in Figure 5.2 are linearly extrapolated for one year and mapped in Figure 5.3.

Figure 5.3 compares the metal thickness remaining after exposure to salt melts, thereby ranking the corrosion performances of the tested alloys. It is clear that both the chromia-forming and alumina-forming alloys in contact with nitrate melts have sufficiently high corrosion resistance at 650°C after 1,000 h. Interestingly, the chromia-forming alloys immersed in alkali carbonate melts showed the poorest behaviours in terms of corrosion among all the investigated alloys. As shown in Figure 5.2, the internal attack in the form of carburisation penetrated deep into the alloy, compromising the alloy's chemistry. In comparison, corrosion testing in chloride melts followed a different pathway since the exposures were

conducted under Ar, and the oxides could only scarcely be formed through interactions with the oxygen impurity.

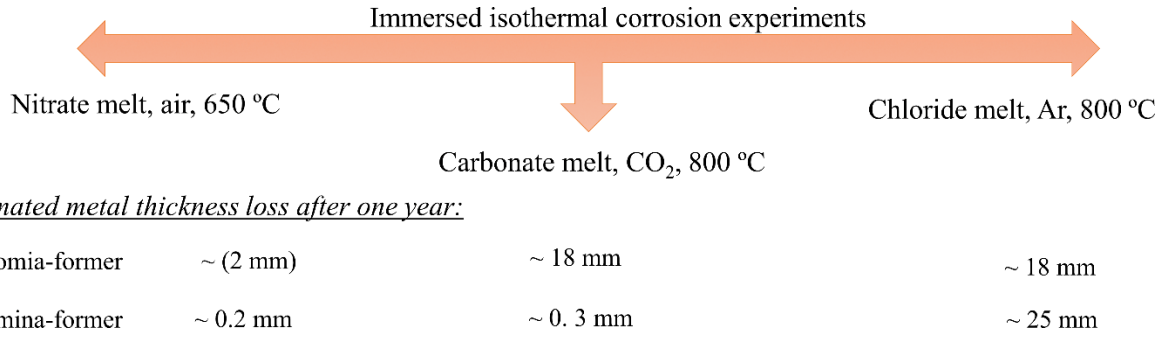


*Figure 5.3 Estimated metal thickness losses for the chromia-forming and alumina-forming alloys immersed in three salt melts, extrapolated linearly for one year. Values are calculated based on scale growth and internal attack depth reported in Figure 5.2.*

As discussed in the introductory chapters, high-temperature corrosion of metallic materials in contact with salt melts is a highly complex phenomenon. While Chapter 3 gives an overview of the corrosion mechanisms related to salt melts, Figure 5.4 (Path A) summarises the corrosion propagation steps identified for the nitrate and carbonate exposures. Figure 5.4 (Path B) describes the corrosion behaviours observed for alloys in contact with chloride melts under Ar as the cover gas.

Path A comprises alkali oxide nucleation at the metal/melt interface and forming an alkali metal oxide scale. This path can progress in the absence of internal corrosion following Cases I and II, i.e., $AMO_x$ scale for $A=Li^+$ growth and eventually $\alpha \rightarrow \gamma$-$LiAlO_2$ phase transformation, as will be discussed in detail in Section 5.3. Alternatively, an internal attack can occur following Cases III and IV, caused by inward diffusion of oxidising species concomitant with $AMO_x$ growth.

Path B accounts exclusively for the observations made for alloys in contact with chloride melts under the Ar cover gas. This path comprises Case V, with no oxide scale formation, and Case VI, which describes the formation of cavities due to selective leaching and environmentally induced inter-metallic precipitation.

In Path A, during oxide scale growth, a depletion zone is created adjacent to the growing oxide scale, depending on whether or not the oxidising alloy element is replenished rapidly. Furthermore, the bulk diffusion of, for example, Al can be compromised by the precipitation of AlN (internal attack). The scale-forming elements derived from the alloys are Al and Cr in this section. The availabilities of Al and Cr at the metal/melt interface define the elemental composition of the oxide scale. Thus, the diffusivities of elements through the bulk and along the grain boundaries are decisive for the formation process.

Notably, if a melt interacts with an alloy and forms a covering insoluble corrosion product, the corrosion product can act as a barrier against further reactions [140].

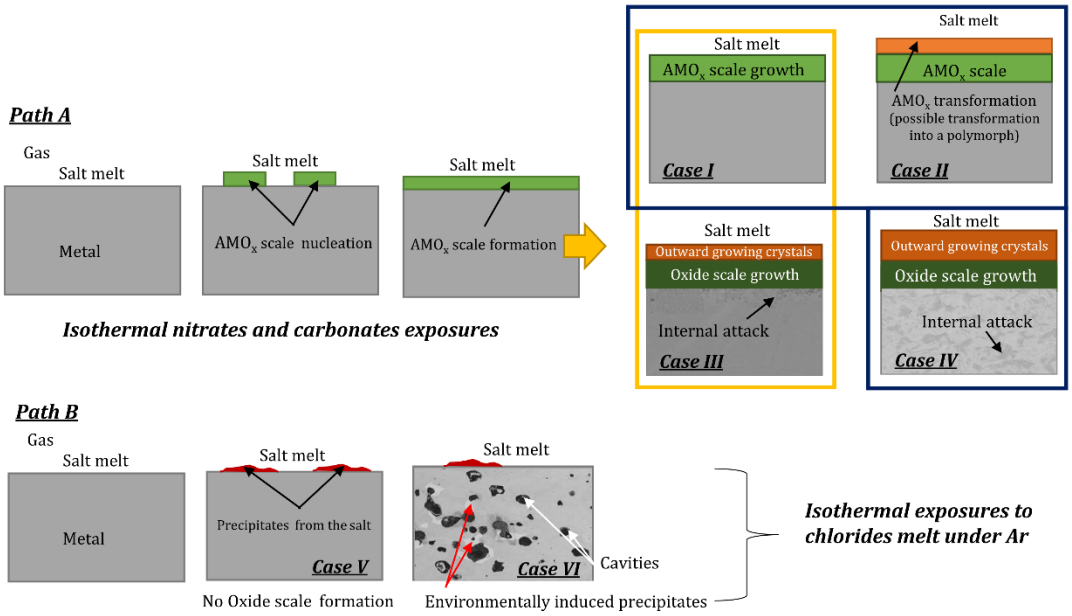


*Figure 5.4 Schematic illustration of the different paths for scale growth, formation, and transformation. The orange and navy markings highlight possible cases of corrosion caused by nitrate and carbonate melts, respectively.*

In this work, the corrosion assessments of the tested alloys exposed to salt melts were made by adopting a combination of quantitative and qualitative approaches. Weight change and scale thickness measurements of the exposed samples provide a quantitative overview. Compositional and microstructural investigations provide a qualitative analysis. As described in Chapter 4, mass change was measured after rinsing the samples with water, entailing the loss and dissolution of soluble corrosion products. Therefore, the evaluation of corrosion is based mainly on top-view and cross-sectional microscopy, while the mass change values are used as complementary data.

### *a) Isothermal immersion in a nitrate melt*

Based on the SEM/EDX investigations and the XRD analysis, the corrosion propagation profiles of alloys immersed in molten alkali nitrate at 650°C can be schematically depicted, as in Figure 5.4 Path A (Case I) for Kanthal® APMT and (Case III) for 316H, respectively. Both the 316H and Kanthal® APMT alloys formed an $AMO_x$ scale at the alloy/melt interface. The oxide scale comprised an outward-growing alkali-bearing species, either sodium aluminate or sodium ferrite, and an inner oxide zone, which is protective in the case of Kanthal® APMT and is a permeable chromia layer in the case of 316H. Finally, internal nitridation was noted in the case of 316H. However, the degree of protection provided by each alloy differed markedly. Exposing 316H to Solar Salt for at least 1,000 h resulted in four corrosion zones [see **Paper I (a)**].

Figure 5.5 compares the corrosion behaviours of 316H (a) and Kanthal® APMT (b) alloys immersed in Solar Salt. Kanthal® APMT exhibited higher corrosion resistance compared to 316H, with a smooth, thin, dense sodium aluminate scale covering the surface after exposure to Solar Salt at 650°C for at least 1,000 h.

After 1,000 h of exposure, local nodules of sodium ferrite were detected, in agreement with the XRD findings. However, the presence of an alumina scale beneath these nodules indicated an early stage of sodium ferrite formation and the inability of these nodules to grow further. Unlike the 316H samples, internal nitridation was not detected in the Kanthal® APMT samples. However, it is important to point out that AlN formation is thermodynamically spontaneous, and when there are defects in the outer scale, nitrogen ingress could cause internal AlN formation. This means that the aluminium activity in bulk may decrease through AlN formation upon scale failure. Therefore, sustaining the aluminium oxide scale at the surface is paramount. See Table C1 in **Paper I (b)** for the thermodynamic calculations for the relevant Gibb's free reaction energies at 650°C.

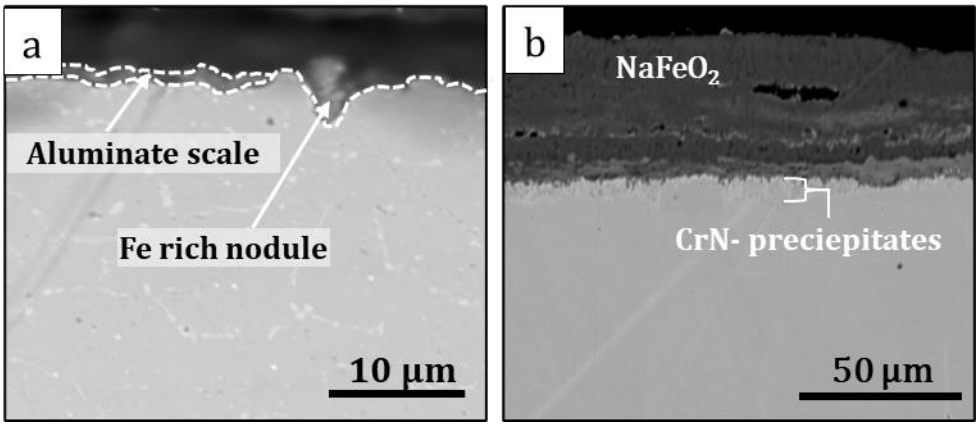


*Figure 5.5 Back-scatter electron microscopy cross-section images of a) Kanthal® APMT and b) 316H samples after exposure to solar salt for 1,000 h. Reproduced with permission from Elsevier [107].*

### *b) Isothermal immersion in a carbonate melt*

Alloys in contact with the $(Li,Na,K)_2CO_3$ melt formed predominantly lithium-containing metal oxides. Alloy 304L showed the formation of spinel oxide and lithium-containing oxides, in agreement with the findings in the literature [141, 142]. The diffractograms of Kanthal® APMT showed only a single crystal structure after 168 h of exposure, which was identified as α-lithium aluminate. After exposure for 1,000 h, an additional crystal structure pattern emerged, which was identified as γ-lithium aluminate [see **Paper I (a)**, Figure 6].

Figure 5.6 (a, b) shows the smooth surface of Kanthal® APMT after exposure to the $(Li,Na,K)_2CO_3$ melt at 800°C for 1,000 h, with the alloy covered by a film of small crystals. For comparison, the surface of alloy 304L shows complete coverage with large octahedral crystallites after 1,000 h of exposure to the carbonate melt [Figure 5.6 (c, d)]. The non-protective, fast-growing $LiFeO_2$ phase has formed. The $LiFeO_2$ crystals formation was expected due to their reaction energies tabulated in [**Paper I (b)**, Section C]. Beneath the $LiFeO_2$ crystals, a mixture of iron and iron-nickel oxides zone is formed; this thick heterogeneous corrosion zone provides no protection to the alloy. Figure 5.6 (e) shows that the carbon originating from the carbonate melt or $CO_2$ cover gas permeates these non-protective oxides and captures chromium in the form of chromium carbide precipitates within the bulk of alloy 304L. Precipitation of chromium carbides is critical for the resistance of the sample to corrosion. It lowers the chromium activity in the alloy, thereby hindering

the outward diffusion of chromium to the metal oxide interface and, consequently, disallowing the formation of a protective chromia oxide scale. In addition, these chromium carbide precipitates change the alloy's microstructure and mechanical properties [143].

The severe internal attack observed for 304L after exposure to the carbonate melt would lead us to expect a high mass gain. However, the mass change is stagnant [see **Paper I (a)**; Figure 2]. This finding indicates the dissolution of metal ions into the carbonate melt. This is substantiated by the salt melt colour observed after the exposures. In addition, thermodynamic calculations show that the chromia reacts exothermically with lithium carbonate and $CO_2$ at 800°C to form lithium chromate [see **Paper I (b)**, Section C]. These findings are in agreement with those of a previous study [144].

The corrosion propagation of alloy 304L in carbonate melt after 1,000 h is schematically illustrated in Figure 5.4 (Case IV). For a detailed analysis of the corrosion products' microstructures, topographies, and chemistries [see **Paper I (a)**].

The Gibb's free reaction energy for lithium ferrite formation through reacting iron with lithium carbonate was found to be exothermic, whereas the reaction with sodium carbonate $NaFeO_2$ is endothermic at 800°C, considering the same reactants apart from the alkali ion species. This also explains the absence of $NaFeO_2$ in the corrosion products. For detailed calculations, [see **Paper I (b)**, Section C, Eqs. (7) and (8)].

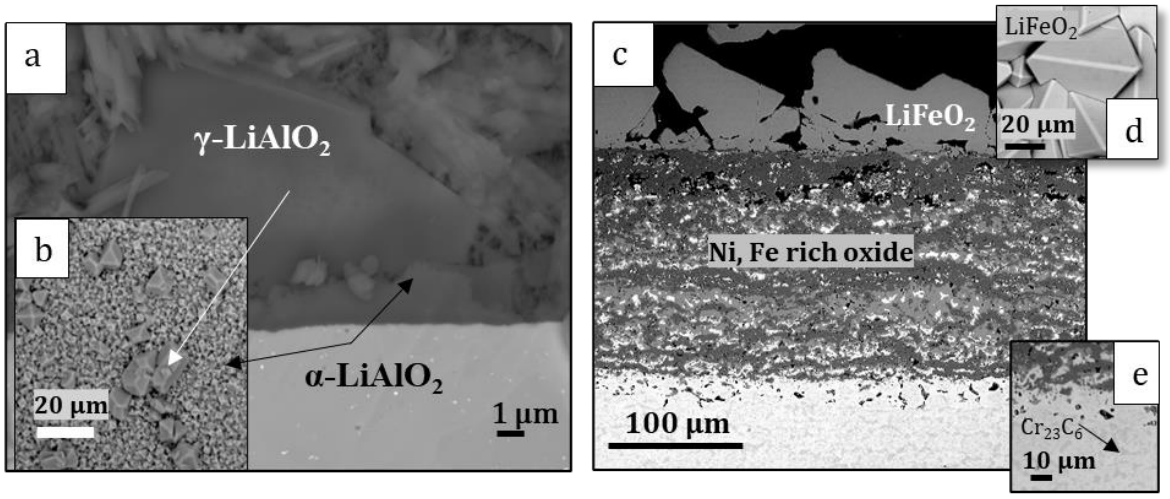


*Figure 5.6 Overview back-scatter electron microscopy image of a) a cross-section and b) a top-view image of Kanthal® APMT exposed to molten carbonate salt mixture at 800°C for 1,000 h.*
*Back-scatter electron microscopy image of c) a cross-section of 304L exposed to molten carbonate salt mixture at 800°C for 1,000 h. d) Top-view image of the surface, and e) internal attack of the bulk and formation of $Cr_{23}C_6$. Reproduced with permission from Elsevier [107].*

### *c) Isothermal immersion in chloride melt*

For alloys that are immersed in the $MgCl_2$-KCl melt, it is important to emphasise that the oxidation reactions that occur during the exposure to the chloride melt are limited by oxygen impurities in the Ar gas stream and residual humidity in the molten salt, as explained in Chapter 3. The only oxides that can form under these extreme conditions have a very high level of thermodynamic stability. Magnesium oxide and magnesium aluminate are among these oxides, as detected and reported in [**Paper I (a)**, Figure 9].

Recalling the mass change data presented in [**Paper I (a)**, Figure 2], both of the tested alloys underwent accelerating mass loss, with a more-pronounced effect seen for 304L compared to Kanthal® APMT. In addition, the overall coupon thickness decreased, as presented in Figure 5.3 and documented in [**Paper I (b)**, Section B]. The dissolution processes of alloy elements have also been reported in previous studies [123].

The microstructural analyses of the 304L samples revealed that the chloride melt immediately leached the alloy elements [see **Paper I (a)**, Figure 10]. EDX elemental mapping detected alloy species, such as chromium and nickel, in the salt residue covering the top of the sample, which is in agreement with the paper of Ding *et al.*, who reported chromium dissolution into molten chlorides [50]. As these metals leached from the bulk alloy, cavities were formed that reached a depth of ~150 µm into the alloy's microstructure after 500 h of exposure.

The $MgCl_2$/KCl eutectic melt reacted with oxygen impurities to induce MgO precipitation on the alloy surface. The SEM/EDX analyses revealed the presence of MgO precipitates over the entire surfaces of the 304L samples after 168 h of exposure. MgO also filled the cavities in the alloy, together with traces of chlorides. These findings are similar to those of a previous study [50] and may indicate the presence of a three-dimensional cavity network within the specimen.

The corrosion propagation patterns of 304L and Kanthal® APMT in chloride melts after 168 h, and 500 h are schematically illustrated in Figure 5.4, Path B (Case V). No oxide scale was formed; instead, cavities and environmentally induced precipitates were formed, as shown in Figure 5.4 (Case VI).

The XRD spectra and cross-sectional analysis of Kanthal® APMT after 168 h exposure to molten chlorides revealed the presence of $MgAl_2O_4$ at the sample surface and a molybdenum-rich inter-metallic phase in the sub-surface region. EDX cross-sectional spot analysis confirmed the presence of alumina particles at the top surface of the sample [see **Paper I (a)**, Figure 11 (a, b)]. Interestingly the bright Z-contrast of the sub-surface region back-scatter image was due to molybdenum enrichment. This enrichment was sufficient to stabilise Laves-phase precipitates.

Detailed thermodynamic calculations regarding the stability of the Laves phase are provided in [**Paper I (b)**, Section D]. The thermodynamic calculations confirm the presence of a two-phase regime at 800°C, comprising BCC and C14 Laves phases with the approximate composition of $(Fe_{0.75}Cr_{0.25})_2Mo$ for the latter.
After 168 h of exposure, the Kanthal® APMT had not yet suffered an internal attack. However, after 500 h, the chloride melt succeeded in attacking the alloy internally and changing its integrity by selectively leaching aluminium, creating a cavity network to a depth of ~280 µm.

Representative images of Kanthal® APMT after 500 h exposure are compiled [see **Paper I (a)**, Figure 11 (c–e)]. Only fragments of alumina remained at the surface. In addition, a pattern of pores was detected at the alloy surface. The line-scan in [**Paper I (a)**, Figure 11 h)] shows the depth of depletion of the aluminium in a cross-sectional analysis of the attacked sample. Similar to what was observed for alloy 304L, these cavities were filled with MgO and traces of chlorides. Aluminium was leached most efficiently through the cavity network, leaving a molybdenum-rich Laves-phase rim around several individual cavities. After 500 h, these Laves-phase rims around the cavities were at a minimum distance of ~100 µm from the metal/salt interface. In conclusion, the Laves-phase precipitates appeared transiently during the overall leaching process. It was observed that these precipitates had already disappeared from the upper region of the sample, indicating delayed chromium leaching from and through the Laves phase.

The overall mass loss for Kanthal® APMT was lower than that for 304L [see **Paper I (a)**, Figure 2]. This difference in mass loss between the two alloys can be attributed to the lower degree of chromium leaching from Kanthal® APMT. However, the Kanthal® APMT suffered a deeper internal attack, which compromised the integrity of the alloy. Gomez-Vidal *et al.* have studied the corrosion performance of a pre-oxidised Kanthal® APMT in contact with a chloride melt and shown that this procedure does not result in Laves-phase precipitates [58].

In summary, both the chromia-forming and alumina-forming alloys that were in contact with the nitrate melt had the highest levels of corrosion resistance, particularly in the case of Kanthal® APMT. Alumina-forming alloys immersed in alkali carbonates showed very promising performances, together with an interesting α- to γ-$LiAlO_2$ phase transformation. The exposures to $MgCl_2$-KCl melts caused the most serious damage to the tested alloys. However, molybdenum showed potential for influencing corrosion resistance, given that it formed a Laves phase barrier to chromium leaching. However, this did not prevent the rapid dissolution of aluminium from the alloy.

## 5.2 Part II: Effects of Evaporated Salt Species on the Corrosion Behaviours of the Set-up Vessels

As described in Chapter 4, studying the corrosion behaviours of metallic materials in salt melts necessitates the establishment of a suitable set-up that mimics the conditions in TES tanks. Even though our experimental set-up fulfilled the requirements it was built for, part of the set-up, the vessels hosting molten salt exposures, underwent a strong corrosion attack, despite not being in direct contact with the melt.

Even though studying the corrosiveness of evaporated salt species for the 253MA vessel materials was not initially planned, we were curious to analyse the corroded vessels and understand the reasons behind their failure. Moreover, to the best of our knowledge, the corrosivity of evaporated salt species in the context of TES applications has not been reported, even though we can always expect to find such conditions in a tank with fluctuating TES filling levels. The vessels seemed to provide a good example for a corrosion case study, as they suffered an attack from evaporated salt species for a relatively long duration, in addition to the effects of the temperature gradient along the vessel wall.

The most striking result from this part of the thesis is that the evaporated salt species caused more-severe corrosion than direct contact between the alloy and molten salt. Thus, metallic materials immersed in salt melts have not experienced the most-corrosive conditions. This statement is valid for the vessel set-up configuration used in this study, which includes a cover gas and salt melt impurities.

This part describes the corrosion of the 253MA vessels exposed to two different evaporated salt species. The first section concerns a vessel that hosted $(Li,Na,K)_2CO_3$ melt exposures, while the second concerns a vessel that hosted $MgCl_2$-KCl melt exposures.

### *5.2.1 Vessel Hosting $(Li,Na,K)_2CO_3$-Exposure Experiments under $CO_2$*

The vessels used for carbonate melt exposures underwent more than 4,000 h of intermittent operation before decommissioning; thus, the vessel material had the longest exposure time tested in this thesis. It is worth recalling that there is a temperature gradient along the vessel wall, as described in Chapter 4. Therefore, we assumed that we would find a correlation between the temperature and the observed corrosion attack. Since the vessel material could not be treated as a classical coupon in terms of evaluating the mass change, we opted for a "remaining metal thickness method" for an overall assessment of corrosion [see **Paper I (b)**]. This method provides a viable alternative to finding out how much metal was lost, particularly since the vessel was brushed several times during its lifetime.

Figure 5.7 depicts: a) the temperature profile along the vessel wall; and b) the residual metal thickness after >4,000 h of operation. Surprisingly, the samples that suffered the strongest corrosion attack were not those that experienced the highest temperature, which might seem counterintuitive at first glance. Instead, those samples were exposed closest to the source of the evaporating gas species and, thereby, the highest concentration of corrosive species in the cover gas stream.

The cover gas utilised for this exposure was 100% $CO_2$ to suppress the decomposition of carbonates in the melt. It should be kept in mind that $CO_2$ itself causes corrosion at high temperatures.

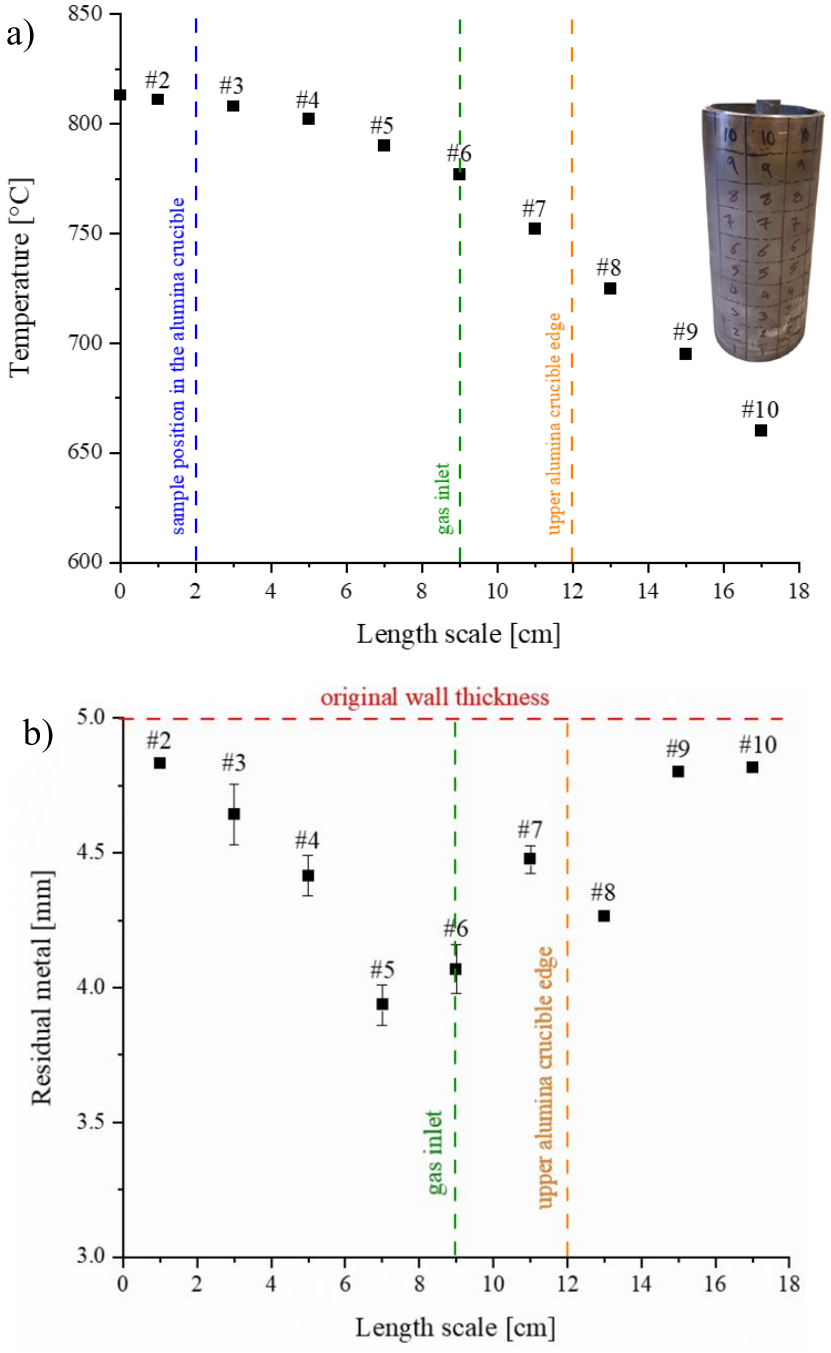


*Figure 5.7 a) Temperature profile within the vessel during operation at 800°C; at the top right is an image of the decommissioned vessel marked with the sample numbers. b) Average residual metal wall thickness measured for samples taken at different heights in the vessel. Reproduced with permission from MPDI (energies)* [145].

As discussed in Chapter 4, an aluminium diffusion coating was initially applied to the 253MA vessels to prolong their lifetime and enhance their resistance to the anticipated highly corrosive environment. Based on our coating procedure, we would expect the "hottest zone" to be coated with an alumina scale. However, after >4,000 h of operation, no coating remained. It is worth highlighting that a few locations still had isolated aluminium-rich precipitates within the oxide scale in the form of potassium aluminate particles. Interestingly, the wall thicknesses at locations with aluminium enrichment recorded lower metal losses than most surfaces that withstood the corrosion without any coating remnants [see **Paper II**]. It needs to be stressed that the "hottest zone" had the highest level of corrosion resistance of all the locations along the vessel.

Let us now turn to the zone that suffered the most from the evaporated salt species in this study: the middle-temperature zone. It showed a thick, heterogeneous, defect-rich, mixed oxide zone that did not protect the alloy. In addition, sodium and potassium salt species were detected within the porous scale in the EDX point analysis, as shown in Figure 5.8 (c). The absence of lithium species was unexpected since lithium was the most-active alkali species when 253MA was in direct contact with the melts [146].

One last aspect clearly shows the failure of 253MA to resist the evaporated salt species attack in terms of internal carburisation and precipitation, which were detected at depths of several hundred micrometres within the alloy; Case IV (Figure 5.4). The reason for the carburisation is two-fold: 1) the reaction with condensing carbonates; and 2) the carbon dioxide cover gas acting as a carbon source. From the position with the highest level of corrosion, the synergy between the corrosion attack by evaporated carbonates and $CO_2$ is greatest with increasing carbonate level closest to the melt/gas interface.

In conclusion, despite the failure of the 253MA alloy to form a protective scale against evaporated salt species in the $CO_2$ cover gas, the alloy forms an ~2 µm-dense adherent protective Fe-Cr spinel oxide on the air side of the vessel.

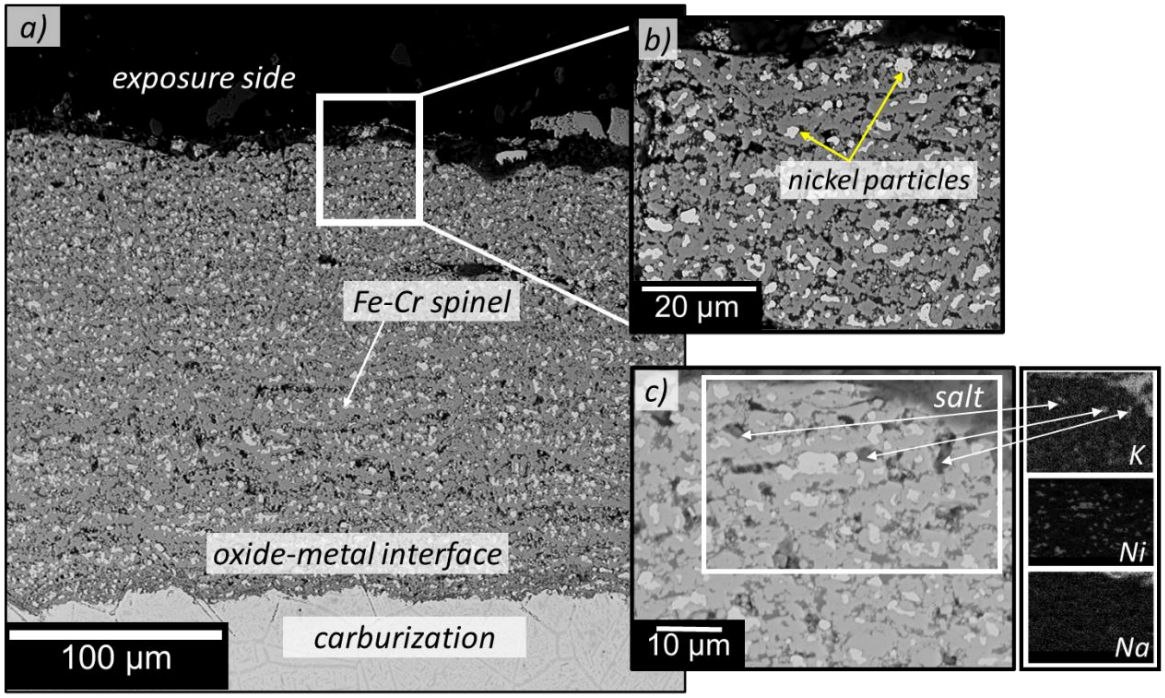


*Figure 5.8 a) Low-magnification back-scattered electron micrographs of sample #7 showing the oxide layer and carburisation beneath the oxide-metal interface. (c) High-magnification of image (a) presenting the oxide scale on sample #7, which comprises a Fe-Cr spinel and nickel particles. (c) K, Ni, and Na EDS elemental maps showing potassium species incorporated in the heterogeneous oxide scale. Reproduced with permission from MPDI (energies)* [145].

### 5.2.2 Vessel Hosting $MgCl_2$-KCl-Exposure Experiments under Argon

Similar to the previous section, the following pages briefly describe the corrosion behaviour of 253MA when exposed to the $MgCl_2$-KCl melt. Unlike the vessels hosting the carbonate melt exposures, vessels exposed to the chloride melt had much shorter lifetimes. These vessels suffered severe damage and were decommissioned after only ~700 h of operation.

As discussed in the earlier chapter, molten chlorides are considered potential TES materials for the next-generation CSP plants. Since the corrosion that occurs in chloride melts is impurity-driven, different inhibitor strategies have been proposed to reduce the oxygen and humidity levels in the melts by, for example, adding elemental Mg to potassium-magnesium chlorides [24, 40, 45] (see Chapter 3). However, based on our findings, and in strong contrast to the behaviour of 253MA that was in direct contact with the $MgCl_2$-KCl melt, magnesium was not the most-active cationic species causing corrosion in the vessel wall exposed to evaporated salt species; instead, it was potassium. This unexpected observation is crucial for the design of the Gen3-CSP storage tank and the applied inhibitor strategy.

As was pointed out in the previous section, the "remaining metal thickness method" is a reliable way to evaluate corrosion in such a case. Nevertheless, additional parameters were considered for the overall corrosion assessment due to the complexity of the corrosion behaviours in these vessels. In Figure 5.9, both measures, remaining metal thickness (left vertical axis) and depth reached by the internal attack (right vertical axis), are plotted.

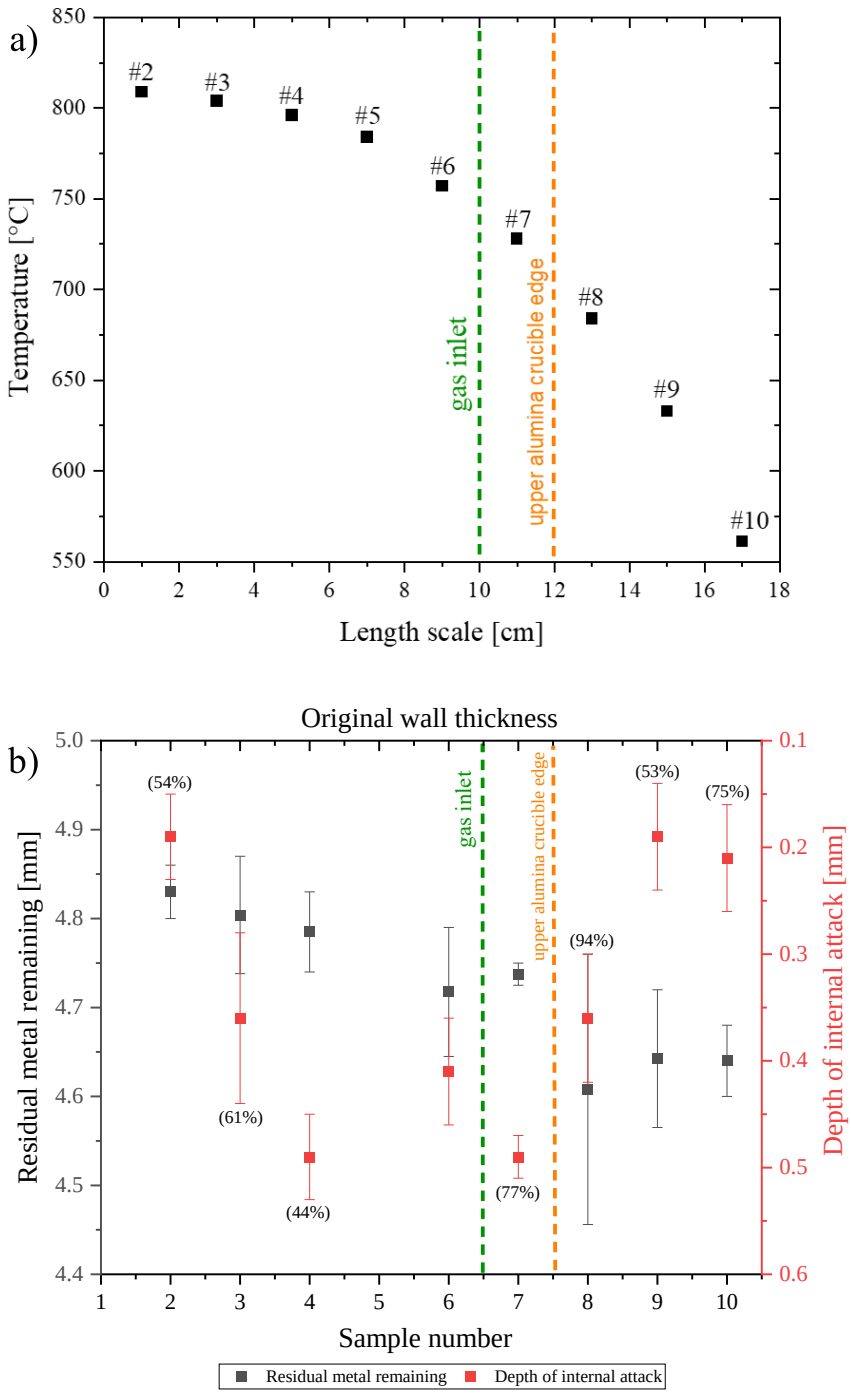


*Figure 5.9 a) Temperature profile within the vessel during operation at 800°C.*
*b) The left y-axis (in black) indicates the average residual metal wall thickness at different heights along the vessel wall, measured after vessel decommissioning. The right y-axis (in red) shows the average depth of the internal attack in each sample. The percentages (%) accompanying the internal attack values represent the accumulated measured area fractions of the cavities and internal oxides.*

Similar to our findings in a previous publication [145], the most-severe attack was not in the hottest zones but in the zones that were exposed to high concentrations of evaporating salt species and that had the highest oxygen impurity levels. Thus, the comparatively high melting point of chlorides compared to carbonates, as described in the former section, results in a larger amount of condensing salt in the colder region of the vessel, as confirmed by the presence of "pure" KCl on the outer oxide scale. Therefore, vessel sections close to the lid, which experience salt condensation and a higher $pO_2$ during vessel openings, are expected to suffer stronger corrosion attacks than other sections. In addition, as described in Chapter 4, evaporated salts condensed on the vessel lid due to the temperature gradient along the vessel wall, occasionally resulting in clogging of the Ar gas exhaust line. Clogging of the outlet line can also accelerate corrosion by preventing the Ar gas from sweeping away the corrosion products formed by $MgCl_2$ hydrolysis, as well as other volatile corrosion products.

Figure 5.10 presents one of the samples that was severely damaged by the evaporated salt species. The samples show different corrosion features, e.g., oxide spallation, pore formation, inter- and intra-granular attack, excess leaching of alloying elements, and enrichment of KCl within the horizontal cracks.

In conclusion, the evaporated alkali species caused significantly more damage to the 253MA vessel material than direct contact with the melt. The high level of corrosion damage observed might be explained by the higher concentrations of gaseous impurities, as well as the evaporating salt species. Finally, the proposed inhibitor strategies exhibit promising corrosion mitigation in such an environment. One needs to consider, however, that the metallic materials exposed to evaporated gaseous species above the level of the melt might not benefit much from such a strategy.

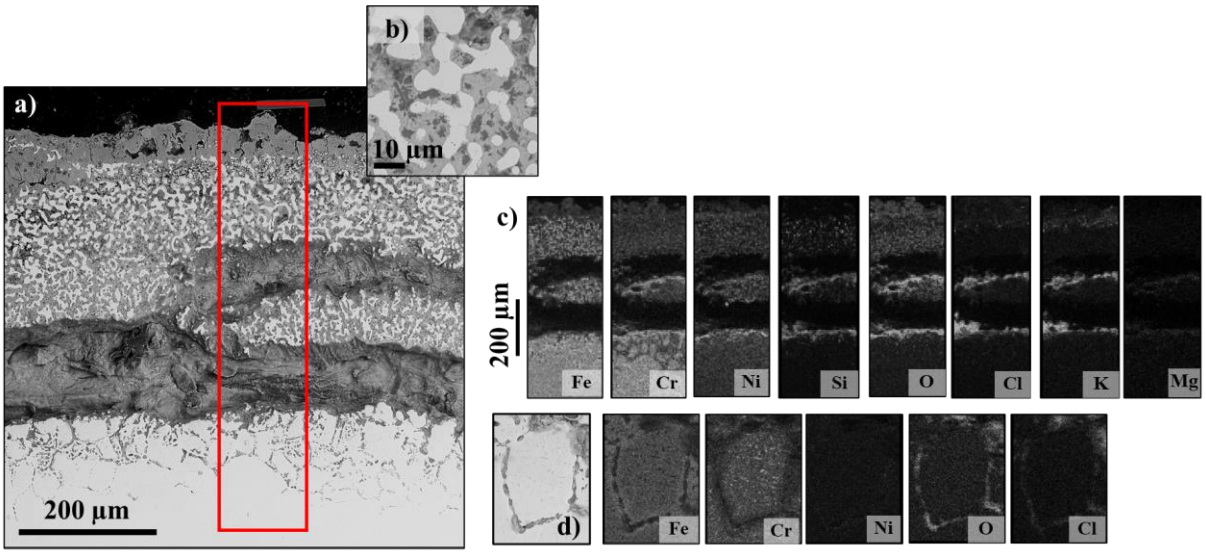


*Figure 5.10 Cross-sectional SEM image of sample #7 exposed to evaporated KCl-$MgCl_2$ melt at ~730°C for ~700 h, showing four distinct corrosion zones. b) High magnification of image (a) showing pores/cavities filled with salts or internally oxidised. c) EDX elemental mapping showing the most-depleted and most-active species in the tested section. d) Higher magnification of an attacked grain boundary showing the inter- and intra-granular precipitates.*

## 5.3 Part III: Comprehensive Analysis of the Microstructural Evolution of Lithium Aluminate Formed on Selected FeCrAl Alloys Immersed in Carbonate Melt

As mentioned in Section 5.1, an interesting α-$LiAlO_2$ to γ-$LiAlO_2$ phase transformation was observed. What is surprising about this is that α-$LiAlO_2$ is not thermodynamically favoured at 800°C [147-149]. However, an α-$LiAlO_2$ scale was observed in all the investigated ferritic FeCrAl alloys. In contrast, the thermodynamically stable γ-$LiAlO_2$ was not detected at exposures performed for <168 h, although it appeared progressively during longer exposures. Therefore, this striking finding is subjected to detailed, thorough microstructural and crystallographic analyses in this section.

In 1978, Evans *et al.* proposed the stress-assisted formation concept for a duplex oxide scale; this duplex oxide scale consisted of tetragonal and monoclinic zirconia polymorphs on zircaloy-1 (zirconium with 2.5% tin) [150]. Evans and colleagues reported that upon oxidation of zircaloy under compressive stress, a stress-stabilised, tetragonal zirconia morphology emerged at the metal/oxide interface, which subsequently relaxed to become a monoclinic lattice.

Similarly, in 1979, Byker *et al*. proposed the transformation of hexagonal crystals of α-$LiAlO_2$ to tetragonal γ-$LiAlO_2$ crystals [151]. As shown in the Temperature–Pressure phase diagram in Figure 5.11 (a), hexagonal α-$LiAlO_2$ is allowed to form at a substantially lower temperature than its ambient pressure phase-transition point, depending on the magnitude of the applied compressive stress. Figure 5.11 (a) depicts a 3D crystal structure visualisation of the two lithium aluminate polymorphs, where it can be seen that α-$LiAlO_2$ has a more-compact and denser structure than γ-$LiAlO_2$ [135, 136].

In our study, we adopted the concept proposed by Evans *et al.* [150], as well as Byker *et al.* [151], whereby a stress-stabilised inner oxide scale forms underneath a different stress-relieved polymorph. In our case, the stress stabilisation could contribute to the otherwise thermodynamically unstable α-$LiAlO_2$ crystal structure at 800°C. We assumed a limiting steady-state thickness of the α-$LiAlO_2$ inner oxide layer based on our belief that the α→γ-$LiAlO_2$ transformation is one of the examples proposed by Evans *et al.* [150]. To date, several studies have investigated and predicted a limiting scale thickness (also known as the "steady-state thickness") [152, 153]. Such detailed investigations are crucial, given their technological importance for various nuclear power applications [152]. It is worth mentioning that the density of γ-$LiAlO_2$ is 25% lower than that of α-$LiAlO_2$.

The schematic illustration in Figure 5.4 (Case I) explores the evolution of lithium aluminate scales and the $\alpha \rightarrow \gamma$-$LiAlO_2$ phase transformation (Case II).

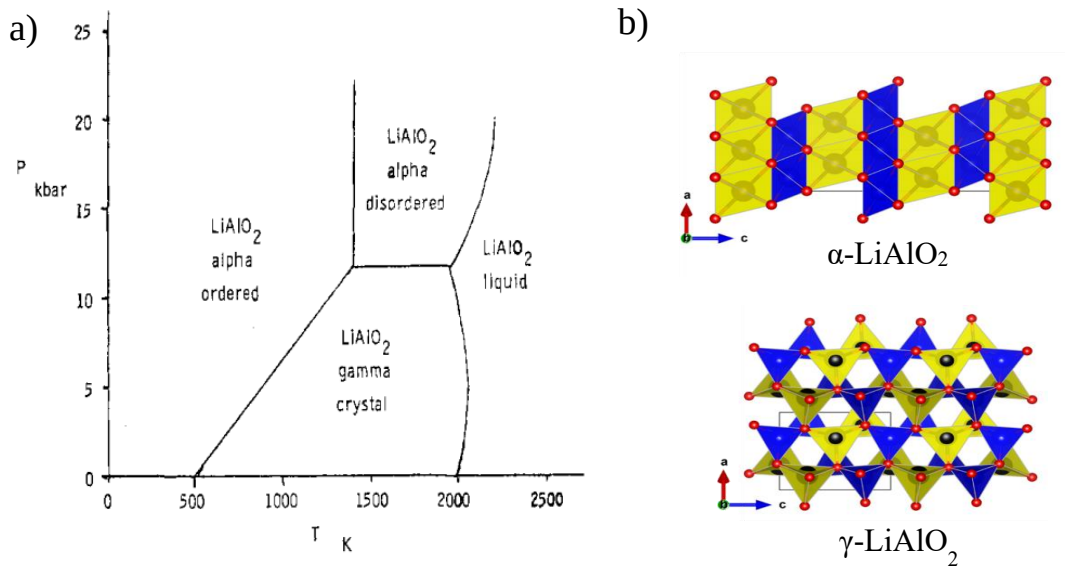


*Figure 5.11 a) Pressure-Temperature phase diagram for lithium aluminate. Source: Byker, H., et al, 1979. Adapted with permission from The Journal of Physical Chemistry A. © (1979) American Chemical Society* [151]. *https://doi.org/10.1021/j100481a009.*
*b) Polyhedral visualisation of α-$LiAlO_2$ and γ-$LiAlO_2$ crystal [135, 136]. Reproduced with permission from Elsevier [154].*

This Part is divided into two sub-sections: Section 5.3.1 thoroughly discusses the formation and transformation of lithium aluminate in five alumina-forming alloys in the absence of pre-oxidation. In comparison, Section 5.3.2 focuses on the effects of pre-oxidation on the formation of a stress-stabilised *α*-$LiAlO_2$ scale and its subsequent relaxation to *γ*-$LiAlO_2$ crystals.

### 5.3.1 Differentiation of Four FeCrAl Alloys and One FeNiCrAl Alloy Immersed in Carbonate Melt in the Absence of Pre-oxidation

In this Section, four ferritic FeCrAl alloys and one austenitic FeNiCrAl alloy were selected to study the evolution of the lithium aluminate formed upon exposure to an alkali carbonate melt at 800°C. Several techniques were utilised to understand better the performances of the alloys in salt melts. Thorough cross-sectional and top-view electron microscopy imaging, as well as XRD Rietveld refinement analysis, were employed to assess the α/γ–$LiAlO_2$ phase fractions. The mass change values were calculated and used as complementary data. As cleaning the samples of salt residues is challenging, these mass change values are difficult to acquire. Combining the results of all these analyses generates a holistic picture of the corrosion behaviours of the selected alloys.

The corrosion performances of the selected alumina-forming alloys can be differentiated into two behavioural categories. The first behaviour is referred to as "normal" $LiAlO_2$ formation without additional cations, e.g., Fe or Cr ions. Transformation of an inner α-$LiAlO_2$ scale growth into a dominating outwards growth of γ-$LiAlO_2$ crystals has been documented. The second behaviour is referred to as the "deviating" formation and transformation of $LiAlO_2$, where the oxidation of Fe(Ni)CrAl alloys involves transient alkali oxide formation and the appearance of pegs that contain ternary cationic species.

#### *a) "Normal" Formation and Transformation of $LiAlO_2$*

As stated earlier, besides aluminium, no other cationic species from the alloy was detected as a scale component. Basically, the $LiAlO_2$ formed was as pure as that obtained from the synthesis route of Lehmann and Hasselbarth [155]. Since the results showed very similar corrosion behaviours for the three "normal"-behaving alloys, the XRD spectra of only one "normal"-behaving alloy are presented. These alloys were Kanthal® APMT, Kanthal® AF and Kanthal® EF101. Interestingly, the XRD phase analysis shown in Figure 5.12 reveals only one crystal structure, α-$LiAlO_2$, after short exposure durations, e.g., 72 h and 168 h. After 168 h, signals for another lithium aluminate crystal structure were noted, and these were attributed to the presence of γ-$LiAlO_2$.

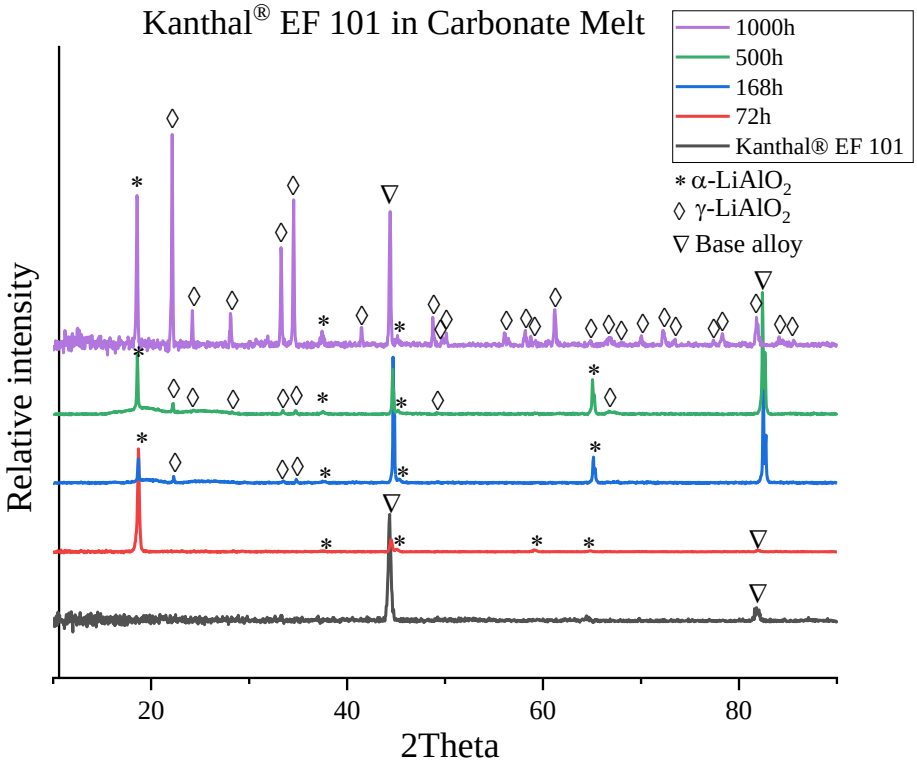


*Figure 5.12 XRD spectra of Kanthal® EF101 after exposure to alkali carbonates in $CO_2$ at 800°C for different exposure times. Reproduced with permission from Elsevier [154].*

The key top-view images of Kanthal® EF101 exposed to a ternary carbonate melt over time are plotted in Figure 5.13. The three "normally"-behaving alloys showed very similar features, where small α-$LiAlO_2$ crystals covered the entire surface after short-term exposures (72 h and 168 h); Case I (Figure 5.4). The larger prismatic γ-$LiAlO_2$ crystals emerged after longer exposure times, such as 500 h and 1,000 h; Case II (Figure 5.4). These findings are in good agreement with the results of the XRD analysis.

Investigations of cross-sectional samples of Kanthal® EF101 showed a distinct double-layer structure composed of a compact inner α-$LiAlO_2$ scale and outer γ-$LiAlO_2$ crystals [see **Paper IV**]. The slight variance in the Z-contrast between the inner and outer layers corresponds to the difference in density between the α- and γ-$LiAlO_2$. Since both forms of $LiAlO_2$ have the same atomic composition, the back-scattered electrons will have a higher probability of scattering back into the detector when interacting with a more densely packed structure [137].

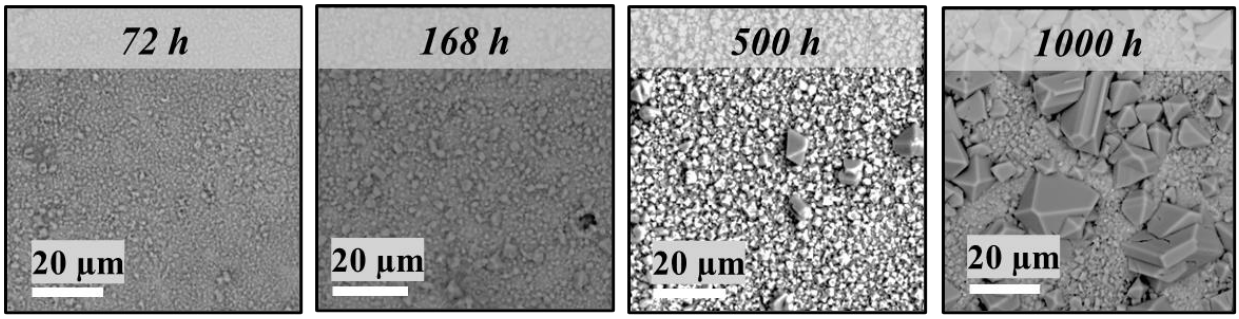


*Figure 5.13 Top-view electron microscopy images of Kanthal® EF 101 showing the "normal" $LiAlO_2$ formation behaviour in the carbonate melt for different exposure times. The large crystals are γ-$LiAlO_2$, and the small crystals are attributed to α-$LiAlO_2$. Reproduced with permission from Elsevier* [154].

To summarise our findings, Figure 5.14 depicts the evolution of the α- and γ-$LiAlO_2$ phases over time for all the tested alloys, as represented by the Rietveld refinement α/γ-phase ratio and the scale thickness. It is noteworthy that the Rietveld-derived α/γ-phase ratio decreases after 500 h of exposure in the cases of Kanthal® APMT and Kanthal® EF101. In contrast, the average thickness continues to increase steadily. Despite the steady increase in average thickness, such a decline in the fraction percentages can be explained by the top-view images in Figure 5.13. Although individual γ-$LiAlO_2$ crystallites continue to grow significantly over time, the number of nucleation sites does not increase concurrently. This random growth and nucleation of γ-$LiAlO_2$ crystallites may have influenced the Rietveld phase fraction curve slope shown in Figure 5.14. The rapid increases in the size and phase fraction of γ-$LiAlO_2$ might be assumed to be caused by the depletion of Al in the alloy. Therefore, all the 1,000 h-exposed samples underwent a line-scan analysis. However, the results revealed the invalidity of this assumption. Furthermore, the growth of the α-$LiAlO_2$ scale was found to decrease over time [see **Paper IV**].

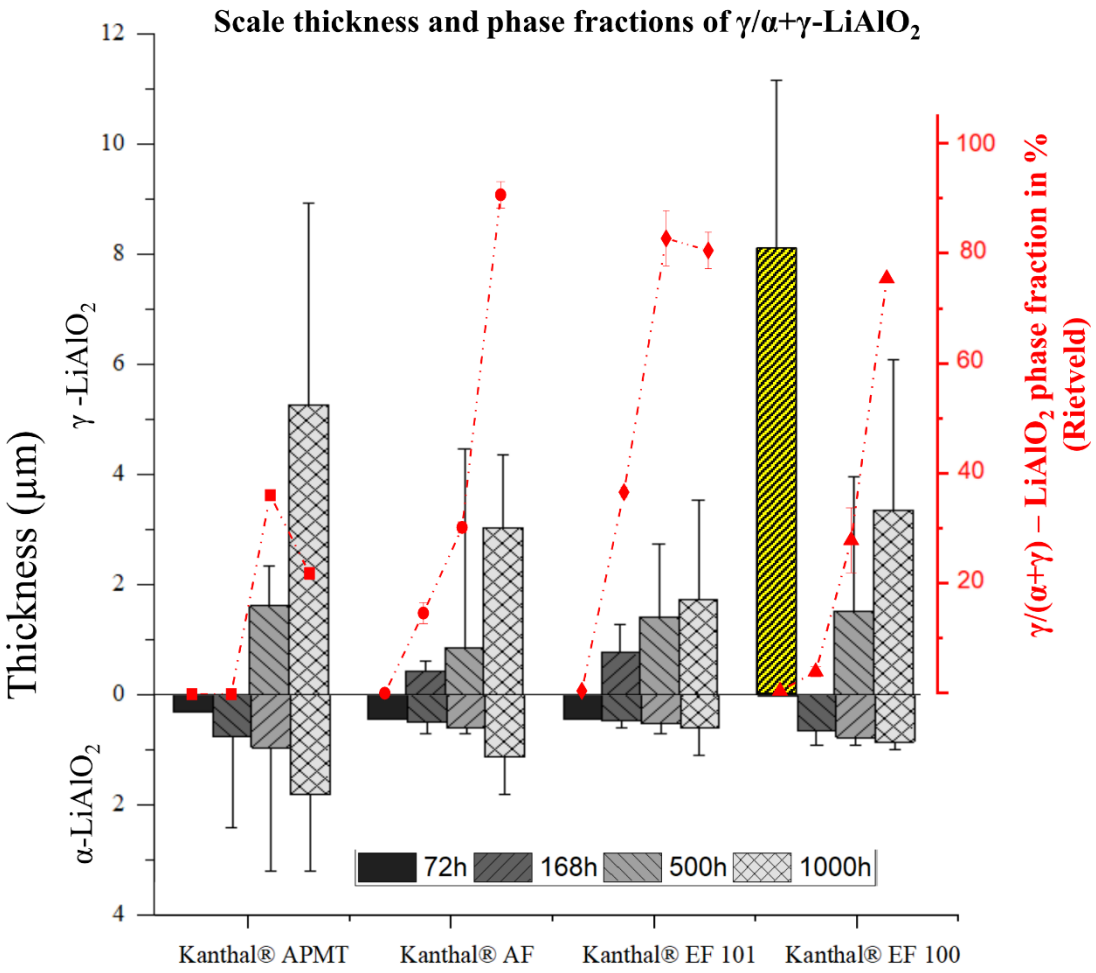


*Figure 5.14 Thicknesses of the α-$LiAlO_2$ and γ-$LiAlO_2$ for the four ferritic FeCrAl alloys and the corresponding results of the Rietveld analysis. Yellow column represents $LiFeO_2$; see Section 5.3 (b). Reproduced with permission from Elsevier* [154].

### *b) "Deviating" Formation and Transformation of $LiAlO_2$*

Unlike the Kanthal® AF, Kanthal® APMT and Kanthal® EF101 alloys, the corrosive behaviours of the Kanthal® EF100 and Nikrothal® PM58 alloys did not follow the "normal" $LiAlO_2$ formation pattern. The so-called "deviating" formation and transformation behaviour was particularly noticeable after short-term exposure. For instance, the Kanthal® EF100 alloy surface was entirely covered with $LiFeO_2$ crystals after 72 h [Figure 5.15 (c)], as confirmed by the XRD analysis [see **Paper IV**]. However, such "deviating" behaviour does not seem to predominate with longer exposure times. In the case of Kanthal® EF100, the $LiFeO_2$ crystals covering the alloy surface disappeared after 168 h of exposure. This is likely due to $LiFeO_2$ dissolution into the carbonate melt. Furthermore, the growth pattern of γ-$LiAlO_2$ crystals followed the "normal" formation behaviour after exposures for 500 h and 1,000 h.

Figure 5.14 demonstrates the obtained Rietveld-derived data and the mean scale thicknesses. Based on these observations, the Kanthal® EF100 alloy was classified as a "normal"-behaving $LiAlO_2$-forming alloy after an initial transient "deviating" state. The long-term behaviour is controlled by γ-$LiAlO_2$ crystallite nucleation onto the slow-growing protective α-$LiAlO_2$ scale.

The initial "deviating" behaviour of Kanthal® EF100 is very similar to the observations made by Asokan *et al.* when comparing the oxidation behaviours of Kanthal® EF100 and Kanthal® EF101 in dry air [156]. Despite their similar chemical compositions, the Si contents of these alloys are significantly different. In the study of Asokan *et al.*, Kanthal® EF101 grew an aluminium oxide scale in dry air, whereas Kanthal® EF100 rapidly grew an iron oxide scale [156].

Si plays a role in forming the protective alumina scale, which can possibly indicate a so-called 'third-element' effect. In this work, when Kanthal® EF101 was immersed in the carbonate melt, the third-element effect of Si contributed to the formation of protective α-$LiAlO_2$. In contrast, Kanthal® EF100, which lacks Si, rapidly grew a covering $LiFeO_2$ scale. Once the scale reached sufficient thickness, the oxygen and lithium activities were low enough to nucleate a slow-growing $LiAlO_2$ layer at the metal/scale interface, thereby significantly decreasing the growth of the scale. $LiFeO_2$ completely dissolved into the melt before 168 h, revealing a pure α-$LiAlO_2$ scale. This $LiAlO_2$ underwent a further $\alpha \rightarrow \gamma$-transformation, as described above for "normal" $LiAlO_2$ formation.

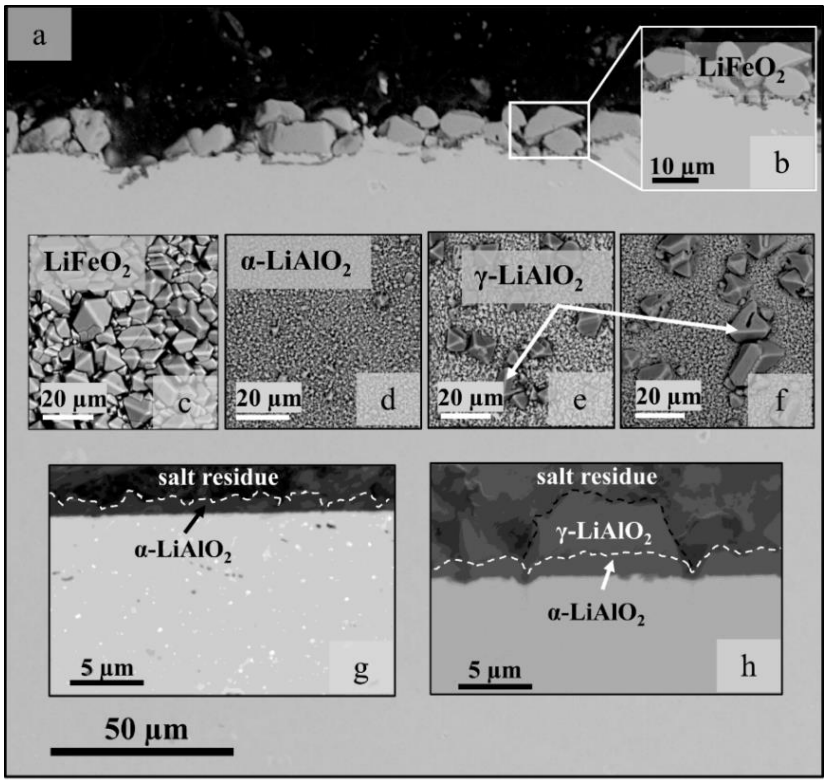


*Figure 5.15 Top-view image of Kanthal® EF100 exposed to alkali carbonate melt at 800ºC, a, b) Cross-sectional image after exposure for 72 h. Top-view images taken after exposure for: c) 72 h, $LiFeO_2$ covers the surface; d) 168 h, only α-$LiAlO_2$ covers the surface; e) 500 h, γ-$LiAlO_2$ crystallites appear; and f) 1,000 h, γ-$LiAlO_2$ crystallite size increased. Cross-sectional images after exposure for: g) 168 h; and h) 1,000 h. Reproduced with permission from Elsevier [154].*

Let us turn now to a rather different "deviating" behaviour, that of Nikrothal® PM58. Interestingly, α-$LiAlO_2$ is commonly formed during exposures at 750ºC [146]. However, at 800°C, the formation of $Li(Cr,Al)O_2$ (instead of the protective α-$LiAlO_2$ scale) was observed. After 1,000 h of exposure to an alkali carbonate melt, Nikrothal® PM58 developed pegs filled mainly with $Li(Cr,Al)O_2$ in the sub-oxide zone, as demonstrated by the XRD and cross-sectional microscopy analyses [see **Paper IV**]. Point analysis of the surface demonstrated the presence of nickel and iron particles at the oxide/melt interface. These transported or overgrown alloy particles can be leached into the alkali carbonate melt. In addition, we noted a zone of aluminium depletion at a depth of approximately 14 µm in the sub-oxide region of the alloy. The aluminium content observed beneath the oxide layer was lower than the nominal composition by 1.2 wt%.

Nikrothal® PM58 exhibits a special "deviating" behaviour that differs from those of the FeCrAl alloys studied. Being an austenitic alloy, the diffusion of aluminium towards the metal/scale interface is slower than is the case for ferritic alloys [157]. The slower aluminium diffusion process is evident in the sub-oxide region [see **Paper IV**]. Even after exposure to alkali carbonates at 800°C, a covering α-$LiAlO_2$ scale failed to form; this is attributed to the fact that a steady-state supply of aluminium to the metal/scale interface is a pre-requisite for maintaining an intact α-$LiAlO_2$ scale. Temperature plays a critical role since the findings obtained at 800°C are strongly discrepant with the results of an earlier study performed in the same

laboratory at 750°C, in which Nikrothal® PM58 formed a slow-growing, protective α-$LiAlO_2$ scale that was sustained for at least 740 h [146].

This observation strongly agrees with the temperature-dependence of the $LiAlO_2$ phase transition studied by Danek *et al.* [147], where the lower temperature limit for γ-$LiAlO_2$ formation was 750°C.

Taken together, the results presented in this section broaden our understanding of lithium aluminate evolution on different alumina-forming alloys. The data also show the effects of the crystal structures and nominal chemical compositions of alloys on their corrosion resistances to alkali carbonate melts at 800°C.

### 5.3.2 Corrosion Behaviours of Four Pre-oxidised FeCrAl alloys in Carbonate Melt

The last section discussed the α/γ-$LiAlO_2$ microstructural evolution of different alumina-forming alloys immersed in $(Li,Na,K)_2CO_3$. This section will demonstrate the consequences of pre-oxidation for lithium aluminate scale development.

Since austenitic Nikrothal® PM58 failed to form an α-$LiAlO_2$ scale at 800°C in the carbonate melt, only the four selected ferritic alloys were subjected to further analysis. Thus, in this section, we go one step further to study the effects of pre-oxidation on lithium aluminate formation and propagation. After pre-oxidising the selected alloys in air at 1,050°C for 8 hours, exciting findings were obtained.

Similar to the classification of alloy performance adopted in Section 5.3.1, alloys will be sorted as "normal" or "deviating" reactions of $Al_2O_3$ in contact with $Li_2CO_3$. The "normal"-behaving alloys react with the pre-formed alumina scale during pre-oxidation to lithium aluminates, while Kanthal® EF100 "deviates" in its reaction pathway.

*a) "Normal" reaction of $Al_2O_3$ scales in contact with $Li_2CO_3$*

Several scenarios were expected regarding the reaction of the formed alumina scale with salt melts. Based on our assumption regarding the stress-stabilised formation of α-$LiAlO_2$, one of the scenarios involved faster growth of γ-$LiAlO_2$ crystals and more nucleation sites; in other words, γ-$LiAlO_2$ was expected to be the predominant phase. Surprisingly, as shown in Figure 5.16, the mass gain obtained for the pre-oxidised alloy was 10-fold lower than that obtained without pre-oxidation in the case of Kanthal® APMT. In addition, comparing the top-view images of exposed pre-oxidised alloys with those taken without pre-oxidation, the large γ-$LiAlO_2$ crystals are scarcely seen. These results reveal a significant change in the α- to γ-$LiAlO_2$ phase transformation.

Figure 5.17 depicts a distinctly different scale development for the Kanthal® APMT exposed to alkali carbonate melt at 800°C. In contrast to the large, emerging γ-$LiAlO_2$ crystals, the cross-sectional SEM image (a) showed significantly smaller crystals. In addition, there was a notable decrease in the alumina scale thickness over time [see **Paper V**]. Since we learned from the last section [18] that the stress-stabilised α-$LiAlO_2$ forms a dense, thin scale before relaxing into γ-$LiAlO_2$ crystals, it can be concluded, in agreement with the XRD results and EDS point analysis, that the three-layered oxide scale seen in Figure 5.18 is composed of γ-$LiAlO_2$ at the alloy/melt interface, with α-$LiAlO_2$ beneath it, and finally, an $Al_2O_3$ scale at the bottom, which was formed upon pre-oxidation.

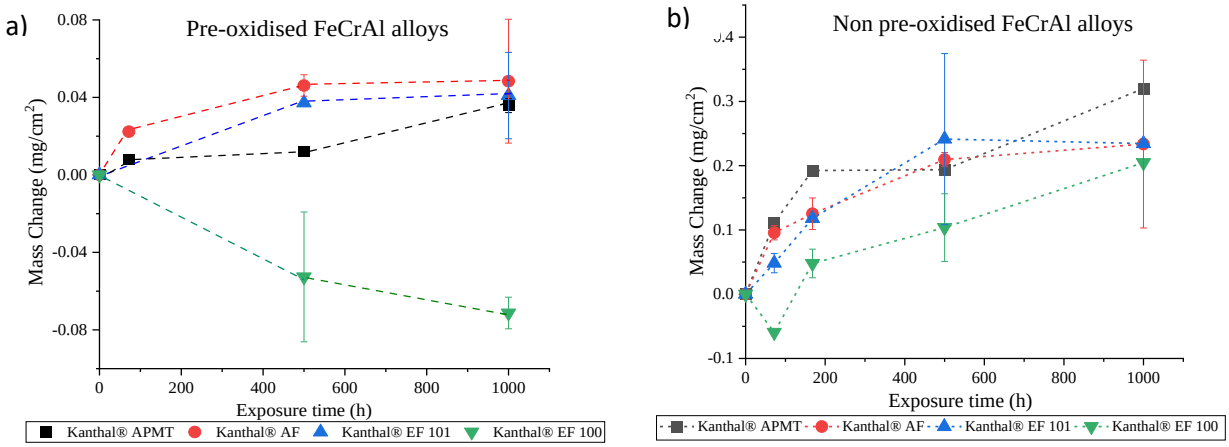


*Figure 5.16 Comparison of the overall mass change behaviours of a) pre-oxidised vs b) non-pre-oxidised alumina-forming alloys immersed in alkali carbonate at 800°C for different exposure times [107]. The mass change values for pre-oxidised samples in (a) are approximately one order of magnitude lower than those for the non-pre-oxidised samples in (b).*

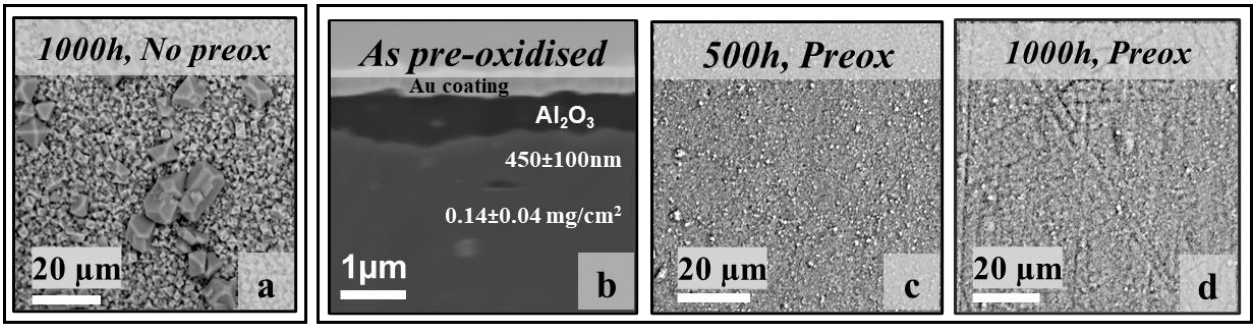


*Figure 5.17 a): SEM back-scattered electron top-view images depicting the surface morphologies of non-pre-oxidised samples exposed to $(Li,Na,K)_2CO_3$-melts at 800°C for 1,000 h [154]. b) SEM back-scattered electron micrographs showing the cross-sections of Kanthal® APMT after pre-oxidation and before the salt exposures. c,d): SEM back-scattered electron micrographs showing the top-view of pre-oxidised "Kanthal® APMT exposed to carbonate melts for 500 h and 1,000 h at 800°C.*

Another interesting finding is the inhomogeneous cloud-like feature (a transition zone) visible in Figure 5.18 (c). This feature looks different in back-scatter electron Z-contrast within the α/γ-$LiAlO_2$ double-layer. An EDS line-scan analysis showed a change in Al at% within these regions. One possible explanation is the presence of different phases upon incomplete reaction with the salt species. In addition, the detection of $LiAl_5O_8$ in the XRD results may support this assumption; for more details, see **Paper V**.

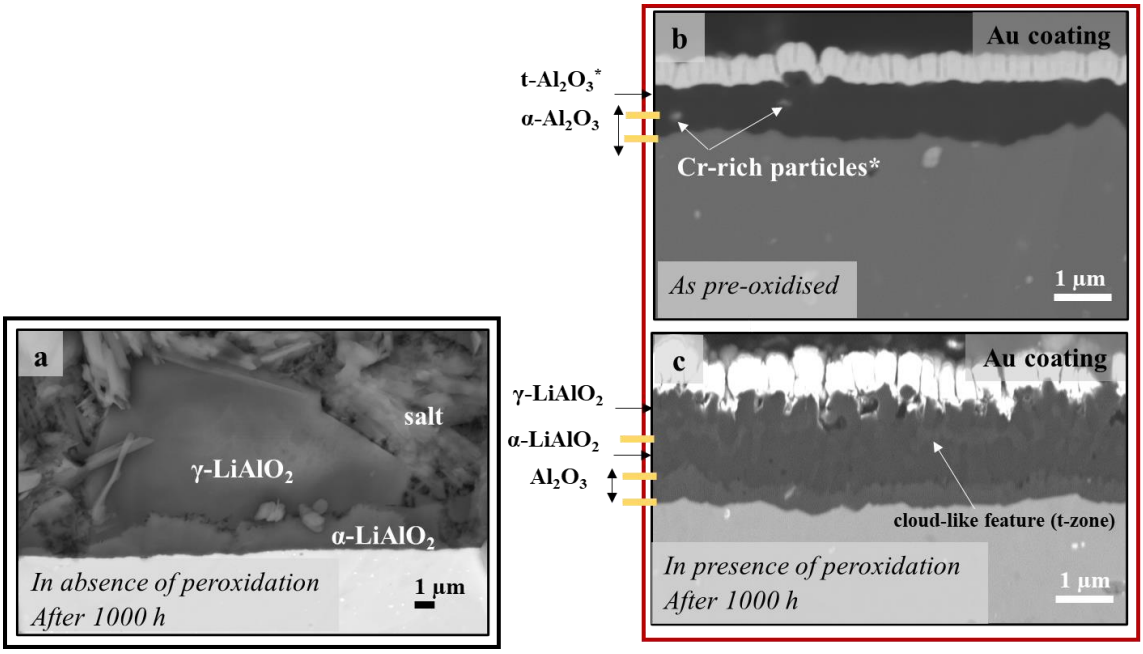


*Figure 5.18 Cross-sectional SEM images of Kanthal® APMT: a) in the absence of pre-oxidation and after 1,000 h of exposure to the alkali carbonate melt; b) after pre-oxidation for 8 h at 1,050°C and before immersion in the carbonate melt; and c) pre-oxidised and after 1,000 h of exposure to the salt melt.*
*An inhomogeneous cloud-like feature (a transition zone) is observed within the α/γ-$LiAlO_2$ double-layer.*
*The SEM image magnification for the pre-oxidised samples in (b) and (c) is approximately three-fold higher than that for the non-pre-oxidised sample (a).*

The evolution of the oxide scales in the pre-oxidised selected ferritic alloys can be explained by the reaction of the alumina scale with $Li_2CO_3$ and the α/γ-$LiAlO_2$ phase transformation. Based on previous studies [158-161], following pre-oxidation of alumina-forming alloys, α-$Al_2O_3$, in addition to other transient phases (t-$Al_2O_3$) such as γ- and θ-aluminas, can be formed.

When a ferritic FeCrAl alloy is exposed to the $(Li,Na,K)_2CO_3$ melt, transient aluminas react with Li- and O-ions from the salt melt. This reaction produces α-$LiAlO_2$, as in Eq. (1). XRD phase analysis of Kanthal® APMT reveals the disappearance of the transient γ- and θ-aluminas after ~500 h of exposure to the alkali carbonate melt, whereas the α-$Al_2O_3$ is still detectable. Therefore, we can assume that the initial rapid low mass gain reflects a 40% mass increase caused by the following reaction:

$$transient\ Al_2O_3 + Li_2O \rightarrow 2\ LiAlO_2 \quad (5.1)$$

As discussed earlier, α-$LiAlO_2$ is a stress-stabilised polymorph that forms a dense inner scale at 800°C on ferritic FeCrAl alloys. In the case of pre-oxidation, upon exposure to the salt melt, the uptake of $Li_2O$ by the transient alumina produces a new source of stress (Pilling-Bedworth effect), as compared to the non-

pre-oxidised case, consequently stabilising the α-$LiAlO_2$. The densely formed α-$LiAlO_2$ acts as a barrier and decreases significantly further transport of ions towards the underlying α-$Al_2O_3$ scale.

Therefore, following pre-oxidisation of Kanthal® APMT, AF, and EF101, a double oxide scale of α-$Al_2O_3$/α-$LiAlO_2$ prevents further oxidation and provides protection that is superior to that conferred by the investigated FeCrAl alloys.

It is worth mentioning that the scenario of transformation of α-$LiAlO_2$ to γ-$LiAlO_2$ or further reaction with lithium carbonate to form higher-lithiated aluminates, e.g., $Li_5AlO_4$, is discussed in [**Paper V**]. Despite the absence of other higher lithiated structures in the XRD spectra, even if we assume complete transformation of the dense α-$LiAlO_2$ to other non-protective forms, the α-$Al_2O_3$ scale would provide a high level of corrosion protection against salt melts.

In summary, pre-oxidation of the alumina-forming Kanthal® AF, APMT and EF101 alloys prior to exposure to the $(Li,Na,K)_2CO_3$ melt provides the best possible protection for the alloy through the formation of an α-$Al_2O_3$/α-$LiAlO_2$ double-scale.

### *b) "Deviating" Reaction of Al-rich oxide scales with $Li_2CO_3$*

Moving on to the "deviating" behaviour of Kanthal® EF100, this alloy exhibits exceptional performance upon exposure to the alkali carbonate melt, even without pre-oxidation. Starting with the pre-oxidation process, Kanthal® EF100 did not develop a pure alumina scale as did the other tested ferritic FeCrAl alloys. Instead, the XRD results revealed the formation of mixed oxides: $(Al_{0.9}Cr_{0.1})_2O_3$, $Cr_{1.4}Fe_{0.6}O_3$, $FeAl_2O_4$, and $Fe_{0.9}Al_{1.1}O_3$; see [**Paper V**].

After exposing the pre-oxidised Kanthal® EF100 to the alkali carbonate melt, the first remarkable finding was the detection of mass loss, which differed from the very low mass gain found in the cases of Kanthal® APMT, Kanthal® AF and Kanthal® EF101 (see Figure 5.16).

Figure 5.19 illustrates the inhomogeneity of the oxides formed during the pre-oxidation of Kanthal® EF100. The cross-sectional SEM analysis in Figure 5.19 (a) shows inward-growing mixed oxides. The upper and medium zones within the oxide layer comprise Fe-Al, Al-Cr and Fe-Cr mixed oxides. The lower zone, with a darker back-scattered electron Z-contrast, is an Al-rich oxide scale. Pegs also developed in the sub-oxide region and were filled with mixed oxides. In addition, Cr inclusions were randomly distributed within the oxide scale.

After 500 h of immersion in the salt melt, Kanthal® EF100 formed a duplex oxide scale with a dense inner scale and an outer porous scale. Interestingly, after 1,000 h, this alloy developed an inner compact, dense and adherent aluminium-rich scale. However, the outer oxide layer, composed of lithiated oxide species, did not adhere to the inner scale. With that, one can speculate that the measured mass loss is partially due to pore formation, into which the melt can leach ions, and partially due to the poor adhesion of the outer oxide layer.

Although it is unclear how the inner aluminium-rich oxide underneath the leached oxide regions can perform during exposures longer than 1,000 h, deceleration of the mass loss seems to be a promising outcome.

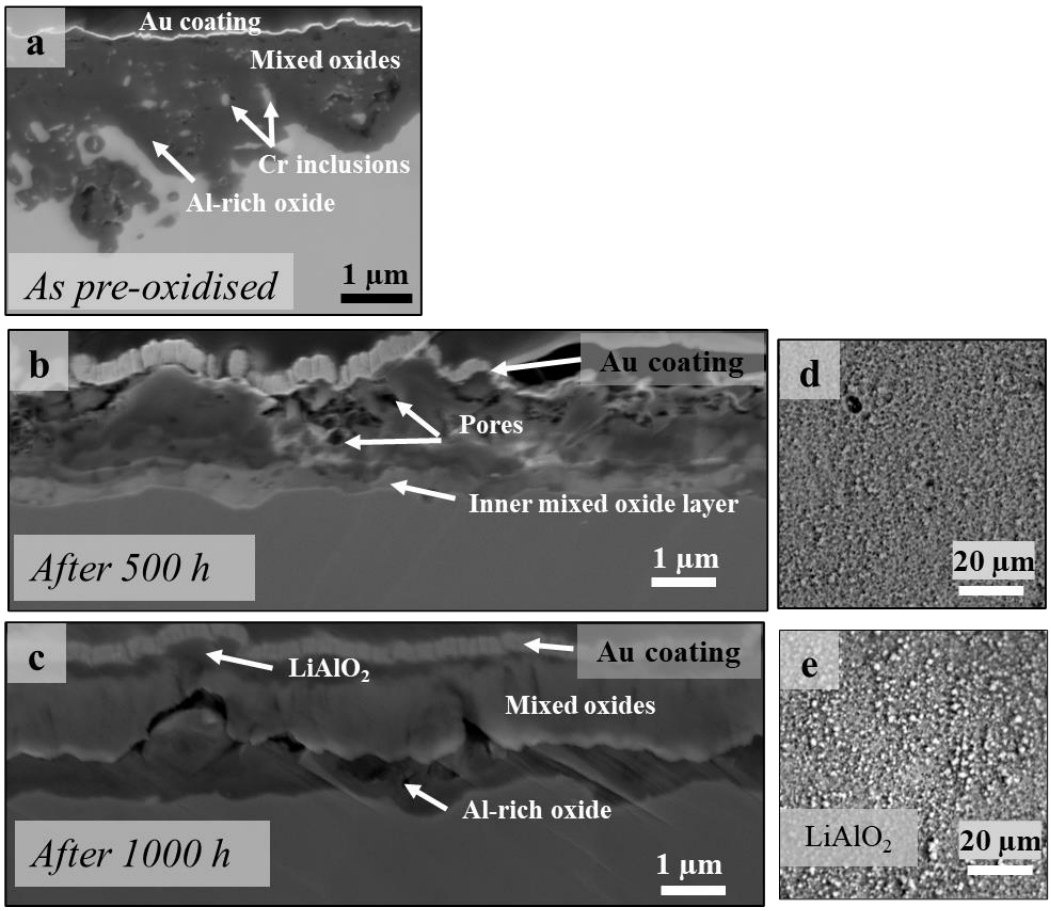


*Figure 5.19* Cross-sectional scanning electron microscopy images of Kanthal® EF100: a) after pre-oxidation for 8 h at 1,050°C; b) after 500 h; and c) after 1,000 h exposure to the salt melt. Top-view scanning electron microscopy images after: d) 500 h; and e) 1,000 h of exposure to the $(Li,Na,K)_2CO_3$ melt.

# 6 Summary

This thesis focuses on the behaviours of metallic materials utilised in the molten salts that are applied in heat storage tanks in CSP plants. The work discussed here is divided into three main parts.

In Part I of the thesis, **Paper I (a)** and **Paper I (b)** compare the corrosion resistances of the currently deployed alloys (FeNiCr) and other promising alternatives (FeCrAl). In addition, the corrosion behaviours of these alloys are studied in three different salt melts, a molten nitrate mixture as the state-of-the-art melt and molten carbonate and chloride mixtures as potential candidates for Gen3-CSP plants. The experiments were conducted at temperatures that exceeded 50–100°C than required in the power plants. The higher exposure temperature was used to accelerate corrosion and ensure the stability levels of the metallic materials in case of heat fluctuations occurring in the hot storage tank, receivers, and piping. Therefore, the exposures were conducted at 650°C for the nitrate melt experiments and 800°C for the carbonate and chloride melts experiments. The corrosion resistance of the chromia-forming alloys 316H/304L and the alumina-forming alloy Kanthal® APMT for the aforementioned salt melts were investigated.

The results show that the nitrate melt is the least corrosive of the three melts tested in our work. Both the chromia-forming and alumina-forming alloys show high corrosion resistance to the nitrate melt, particularly in the case of Kanthal® APMT. Even though the salts internally oxidise 316H, the attack is slow and predictable. It is important to stress that the good corrosion behaviour is partly attributed to the lower operating temperature compared to the molten chloride and carbonate exposures.

In comparison, alloys in contact with carbonate melts show the poorest corrosion performance in our study. The chromia-forming 304L alloy suffers a strong internal attack, with severe carburisation observed throughout the alloy. In stark contrast, Kanthal® APMT shows good corrosion resistance due to the formation of a thin protective layer of α-$LiAlO_2$, which makes it a promising candidate for Gen3-CSP plants. After 168 h of exposure, an interesting phase transition from an α-$LiAlO_2$ to a γ-$LiAlO_2$ oxide scale was observed.

Finally, both 304L and Kanthal® APMT undergo rapid degradation upon exposure to a chloride melt under Ar as the cover gas. The leaching of alloy elements, such as chromium and aluminium, causes the degradation of these materials. Nonetheless, the presence of molybdenum in Kanthal® APMT affects the corrosion process by forming a Laves phase barrier to chromium leaching; however, this does not prevent the rapid leaching of aluminium from the alloy.

The data presented in Part II (**Papers II** and **III**) highlight the difference between the corrosion performances of the 253MA alloy (our experimental vessel material) when in direct and indirect contact with salt melts. The most striking finding in these two papers is that the damage caused to the 253MA vessel by the evaporated salt species from each carbonate and chloride melt exposure is significantly higher than when the alloy is in direct contact with the melt. The high level of corrosion damage can be explained by the higher concentrations of gaseous impurities and the evaporating salt species. Surprisingly, the most-active alkali or alkaline earth salt species participating in the corrosion process differ between direct and

indirect contact with the salt melts. Instead of lithium as the pre-dominating active alkali species in the case of immersion in $(Li,Na,K)_2CO_3$, sodium and potassium take over. Lithium is absent from the indirect exposure experiments. Magnesium is the most-active species in corrosion products when in direct contact with the chloride melt. However, it is almost absent in indirect exposure to salt, and potassium takes over.

Part III (**Papers IV** and **V**) is dedicated to broadening our understanding of the α-$LiAlO_2$ to γ-$LiAlO_2$ phase transition detected in ferritic FeCrAl alloys when immersed in $(Li,Na,K)_2CO_3$ at 800°C. The results presented in **Paper IV** reveal the formation of a duplex oxide scale with an inner dense protective α-$LiAlO_2$ and outer γ-$LiAlO_2$ crystals. The formation of the thermodynamically unfavourable α-$LiAlO_2$, followed by the nucleation and growth of the thermodynamically stable γ-$LiAlO_2$, can be explained by the stress-stabilised concept proposed by Evans *et al.* in 1978. In **Paper V**, the effects of pre-oxidation on α-$LiAlO_2$ scale development were investigated thoroughly. The data show a correlation between the quality of the oxide scale formed during the pre-oxidation step and α-$LiAlO_2$ formation. Transient alumina structures, e.g., γ-$Al_2O_3$ or θ-$Al_2O_3$, can react with $Li_2CO_3$ from the melt to produce dense hexagonal α-$LiAlO_2$, which relaxes further into tetragonal γ-$LiAlO_2$ crystals.

# 7 Outlook

CSP is a promising technology that provides electricity on demand by utilising TES systems. However, the material requirements for implementing Gen3-CSP plants remain a serious challenge.

In this work, we show that the commercially used alkali nitrate melt causes the least amount of corrosion damage compared to the carbonate and chloride melts. Despite the high corrosion resistance of chromia-forming and alumina-forming alloys exposed to nitrate melts, these salts cannot be employed in Gen3-CSP plants due to their limited thermal stability.

One of the promising melts for next-generation CSP plants is $(Li,Na,K)_2CO_3$. Carbonate melts are better candidates than chloride melts in terms of corrosion, although the cost-effectiveness of employing lithium carbonate must be considered.

Carbonate melts severely damage chromia-forming alloys through a deep internal attack in the form of carburisation. Ferritic alumina-forming alloys develop a stress-stabilised, dense, protective $\alpha$-$LiAlO_2$ scale. Besides, superior protection is provided by pre-oxidised FeCrAl alloys against exposure to the eutectic alkali carbonate melt, in that they form a dense $\alpha$-$LiAlO_2$ scale on top of $\alpha$-$Al_2O_3$.

These are very promising results for measures to control corrosion behaviour in melts by utilising FeCrAl alloys. However, different aspects need to be considered. The experimental set-ups used in this work were designed in a simplified form to study the corrosion performances of different alloys under static, controlled conditions. Dynamic corrosion testing is required to simulate the actual conditions in the storage tanks, including erosion-corrosion studies. In addition, we need to consider the costs of the utilised FeCrAl alloys and their availability in the required form and weldability. Another aspect that warrants study is the corrosion behaviours of potential alloys at welded sections.

Chloride melts, which are the other candidates considered for Gen3-CSP plants, are highly corrosive for the metallic components containing them. Since corrosion in such an environment is impurity-driven, further studies are required to investigate salt purification techniques in conjunction with corrosion mitigation strategies, e.g., coatings. However, we must carefully consider applying coatings in the case of defects, such as abrasion or cracking, as this can lead to complete failure of the coating to protect against alloy corrosion.

Another perspective is identifying new metallic materials that can withstand such aggressive environments. This drastic return to the drawing board might be required to enable applications that operate with molten chlorides.

Overall, further research is needed to find solutions to the corrosion challenges faced by metallic materials exposed to potential TES media for Gen3-CSP plants. In this work, guidance is provided in terms of alloy composition, pre-treatments, and salt chemistry to support this ongoing endeavour.

# References


1. Masson-Delmotte, V., et al., *IPCC, 2021: Summary for Policymakers. In: Climate Change 2021: The Physical Science Basis. Contribution of Working Group I to the Sixth Assessment Report of the Intergovernmental Panel on Climate Change*. 2021. p. 4-36.
2. *United Nations Framework Convention on Climate Change (unfccc.int) The Paris Agreement*. 2015 [cited 2021 07-09]; Available from: https://unfccc.int/process-and-meetings/the-paris-agreement/the-paris-agreement.
3. Achkari, O. and A. El Fadar, *Latest developments on TES and CSP technologies – Energy and environmental issues, applications and research trends.* Applied Thermal Engineering, 2020. **167**: p. 114806.
4. Lovegrove, K. and J. Pye, *Fundamental principles of concentrating solar power (CSP) systems*, in *Concentrating Solar Power Technology*. 2012, © Woodhead Publishing Limited. p. 16-67.
5. Köberle, A.C., D.E.H.J. Gernaat, and D.P. van Vuuren, *Assessing current and future techno-economic potential of concentrated solar power and photovoltaic electricity generation.* Energy, 2015. **89**: p. 739-756.
6. Alva, G., et al., *Thermal energy storage materials and systems for solar energy applications.* Renewable and Sustainable Energy Reviews, 2017. **68**: p. 693-706.
7. Zhao, Y., P. Li, and H. Jin, *Heat Transfer Performance Comparisons of Supercritical Carbon Dioxide and NaCl–KCl–ZnCl2 Eutectic Salts for Solar s-CO2 Brayton Cycle.* Energy Procedia, 2017. **142**: p. 680-687.
8. Hoeven, M., *IEA Technology Roadmaps for Solar Electricity*. International Energy Agency, 2014.
9. Bradshaw, R.W. and S.H. Goods, *Corrosion resistance of stainless steels during thermal cycling in alkali nitrate molten salts*. 2001, ; Sandia National Laboratories (SNL), Albuquerque, NM, and Livermore, CA (United States). p. Medium: ED; Size: 39 p.
10. Yin, J.M., et al., *Review of supercritical CO2 power cycles integrated with CSP*. International Journal of Energy Research, 2019. **44**(3): p. 1337-1369.
11. Ho, C.K., et al., *Technoeconomic Analysis of Alternative Solarized s-CO2 Brayton Cycle Configurations.* Journal of Solar Energy Engineering, 2016. **138**(5).
12. Walczak, M., et al., *Materials corrosion for thermal energy storage systems in concentrated solar power plants.* Renewable and Sustainable Energy Reviews, 2018. **86**: p. 22-44.
13. Sarvghad, M., T.A. Steinberg, and G. Will, *Corrosion of stainless steel 316 in eutectic molten salts for thermal energy storage*, in *Solar Energy*. 2018. p. 198-203.
14. *Concentrating Solar Power*. 2010: International Energy Agency
15. Mehos, M., et al., *Concentrating Solar Power Gen3 Demonstration Roadmap.* Nrel/Tp-5500-67464, 2017: p. 1-140.
16. Palacios, A., et al., *Thermal energy storage technologies for concentrated solar power – A review from a materials perspective.* Renewable Energy, 2020. **156**: p. 1244-1265.
17. *US Department of Energy Report: The Year of Concentrating Solar Power*. 2014.
18. Sarvghad, M., et al., *Materials compatibility for the next generation of Concentrated Solar Power plants*, in *Energy Storage Materials*. 2018. p. 179-198.
19. Khare, S., et al., *Selection of materials for high temperature sensible energy storage.* Solar Energy Materials and Solar Cells, 2013. **115**: p. 114-122.

20. Gasia, J., L. Miró, and L.F. Cabeza, *Review on system and materials requirements for high temperature thermal energy storage. Part 1: General requirements.* Renewable and Sustainable Energy Reviews, 2017. **75**: p. 1320-1338.
21. Caraballo, A., et al., *Molten Salts for Sensible Thermal Energy Storage: A Review and an Energy Performance Analysis.* Energies, 2021. **14**(4): p. 1197.
22. Campbell, F.C., *Phase Diagrams - Understanding the Basics*. 2012, ASM International.
23. Palacios, A., et al., *High-temperature corrosion behaviour of metal alloys in commercial molten salts.* Solar Energy, 2020. **201**: p. 437-452.
24. Ding, W. and T. Bauer, *Progress in Research and Development of Molten Chloride Salt Technology for Next Generation Concentrated Solar Power Plants.* Engineering, 2021. **7**(3): p. 334-347.
25. Zhang, X., et al., *Thermodynamic evaluation of phase equilibria in NaNO3-KNO3 system.* Journal of Phase Equilibria, 2003. **24**(5): p. 441-446.
26. Baker, B.A., *1.16 - Types of Environments*, in *Shreir's Corrosion*, B. Cottis, et al., Editors. 2010, Elsevier: Oxford. p. 399-406.
27. Chevalier, S., *1.07 - Mechanisms and Kinetics of Oxidation*, in *Shreir's Corrosion*, B. Cottis, et al., Editors. 2010, Elsevier: Oxford. p. 132-152.
28. Wagner, C., *Beitrag zur theorie des anlaufvorgangs.* Zeitschrift für physikalische Chemie, 1933. **21**(1): p. 25-41.
29. Khanna, A.S., *Chapter 6 - High-Temperature Oxidation*, in *Handbook of Environmental Degradation of Materials (Third Edition)*, M. Kutz, Editor. 2018, William Andrew Publishing. p. 117-132.
30. Gomez-Vidal, J.C., et al., *Corrosion resistance of alumina-forming alloys against molten chlorides for energy production. I: Pre-oxidation treatment and isothermal corrosion tests*, in *Solar Energy Materials and Solar Cells*. 2017. p. 222-233.
31. Gomez-Vidal, J.C., et al., *Corrosion resistance of alumina forming alloys against molten chlorides for energy production. II: Electrochemical impedance spectroscopy under thermal cycling conditions*, in *Solar Energy Materials and Solar Cells*. 2017, Elsevier B.V. p. 234-245.
32. Abu Kassim, S., et al., *High temperature corrosion of Hastelloy C22 in molten alkali salts: The effect of pre-oxidation treatment.* Corrosion Science, 2020. **173**: p. 108761.
33. Ding, W., A. Bonk, and T. Bauer, *Molten chloride salts for next generation CSP plants: Selection of promising chloride salts & study on corrosion of alloys in molten chloride salts.* AIP Conference Proceedings, 2019. **2126**(1): p. 200014.
34. Young, D.J., *Chapter 1 - The Nature of High Temperature Oxidation*, in *High Temperature Oxidation and Corrosion of Metals (Second Edition)*, D.J. Young, Editor. 2016, Elsevier. p. 1-30.
35. Ellingham, H.J.T., *Reducibility of oxides and sulphides in metallurgical processes.* J. Soc. Chem. Ind, 1944. **63**(5): p. 125-160.
36. *Ellingham Richardson-diagram* 2016 [cited 2023 16 March]; Available from: https://commons.wikimedia.org/wiki/File:Ellingham_Richardson-diagram_english.svg.
37. Geers, C. and I. Panas, *Impact of Grain Boundary Density on Oxide Scaling Revisited.* Oxidation of Metals, 2019. **91**(1): p. 55-75.
38. Callister, W.D. and D.G. Rethwisch, *Materials science and engineering: an introduction*. Vol. 7. 2007: John wiley & sons New York.

39. Young, D.J., *Corrosion in Complex Environments*, in *High Temperature Oxidation and Corrosion of Metals*. 2016. p. 603-645.
40. Rahmel, A., *Corrosion*, in *Molten Salt Technology*, D.G. Lovering, Editor. 1982, Springer US: Boston, MA. p. 265-283.
41. Lux, H., *"Säuren" und "Basen" im Schmelzfluss: Die Bestimmung der Sauerstoffionen-Konzentration.* Zeitschrift für Elektrochemie und angewandte physikalische Chemie, 1939. **45**(4): p. 303-309.
42. Flood, H., T. Forland, and K. Motzfeld, *On the oxygen electrode in molten salts.* Acta Chemica Scandinavica, 1952. **6**: p. 257-269.
43. Indacochea, J., et al., *Corrosion performance of ferrous and refractory metals in molten salts under reducing conditions.* Journal of Materials Research, 1999. **14**(5): p. 1990-1995.
44. Lee, H.-Y. and K.-H. Baik, *Comparison of corrosion resistance between Al2O3 and YSZ coatings against high temperature LiCl-Li2O molten salt.* Metals and Materials International, 2009. **15**(5): p. 783.
45. Kruizenga, A.M., *Corrosion mechanisms in chloride and carbonate salts*. 2012, Sandia National Laboratories (SNL), Albuquerque, NM, and Livermore, CA (United States).
46. Ozeryanaya, I.N., *Corrosion of metals by molten salts in heat-treatment processes.* Metal Science and Heat Treatment, 1985. **27**(3): p. 184-188.
47. Li, Y.S. and M. Spiegel, *Models describing the degradation of FeAl and NiAl alloys induced by ZnCl2–KCl melt at 400–450 °C.* Corrosion Science, 2004. **46**(8): p. 2009-2023.
48. Patel, N.S., V. Pavlík, and M. Boča, *High-Temperature Corrosion Behavior of Superalloys in Molten Salts–A Review*, in *Critical Reviews in Solid State and Materials Sciences*. 2017, Taylor & Francis. p. 83-97.
49. Ding, W., A. Bonk, and T. Bauer, *Corrosion behavior of metallic alloys in molten chloride salts for thermal energy storage in concentrated solar power plants: A review*, in *Frontiers of Chemical Science and Engineering*. 2018. p. 564-576.
50. Ding, W., et al., *Hot corrosion behavior of commercial alloys in thermal energy storage material of molten MgCl2/KCl/NaCl under inert atmosphere*, in *Solar Energy Materials and Solar Cells*. 2018, Elsevier B.V. p. 22-30.
51. Mansfeld, F., N. Paton, and W. Robertson, *The high temperature behavior of superalloys exposed to sodium chloride: II. corrosion.* Metallurgical Transactions, 1973. **4**: p. 321-327.
52. Moskowitz, A. and L. Redmerski, *Corrosion of Superalloys at High Temperatures In the Presence of Contaminating Salts.* Corrosion, 1961. **17**(6): p. 305t-312t.
53. Sridharan, K. and T.R. Allen, *Corrosion in Molten Salts*, in *Molten Salts Chemistry*. 2013, Elsevier Inc. p. 241-267.
54. Bell, S., T. Steinberg, and G. Will, *Corrosion mechanisms in molten salt thermal energy storage for concentrating solar power*, in *Renewable and Sustainable Energy Reviews*. 2019, Elsevier Ltd. p. 109328.
55. Ravi Shankar, A., et al., *Corrosion and Microstructure Correlation in Molten LiCl-KCl Medium.* Metallurgical and Materials Transactions A, 2010. **41**(7): p. 1815-1825.
56. Hofmeister, M., et al., *Corrosion behaviour of stainless steels and a single crystal superalloy in a ternary LiCl–KCl–CsCl molten salt.* Corrosion Science, 2015. **90**: p. 46-53.

57. Gomez-Vidal, J.C. and R. Tirawat, *Corrosion of alloys in a chloride molten salt (NaCl-LiCl) for solar thermal technologies.* Solar Energy Materials and Solar Cells, 2016. **157**: p. 234-244.
58. Gomez-Vidal, J.C., et al., *Corrosion resistance of alumina forming alloys against molten chlorides for energy production. II: Electrochemical impedance spectroscopy under thermal cycling conditions.* Solar Energy Materials and Solar Cells, 2017. **166**: p. 234-245.
59. Liu, B., et al., *Corrosion behavior of Ni-based alloys in molten NaCl-CaCl2-MgCl2 eutectic salt for concentrating solar power.* Solar Energy Materials and Solar Cells, 2017. **170**: p. 77-86.
60. Vignarooban, K., et al., *Corrosion resistance of Hastelloys in molten metal-chloride heat-transfer fluids for concentrating solar power applications.* Solar Energy, 2014. **103**: p. 62-69.
61. Vignarooban, K., et al., *Vapor pressure and corrosivity of ternary metal-chloride molten-salt based heat transfer fluids for use in concentrating solar power systems*, in *Applied Energy*. 2015. p. 206-213.
62. Mansfeld, F., N.E. Paton, and W.M. Robertson, *The high temperature behavior of superalloys exposed to sodium chloride: II. corrosion.* Metallurgical Transactions, 1973. **4**(1): p. 321-327.
63. Pillai, R., S.S. Raiman, and B.A. Pint, *First steps toward predicting corrosion behavior of structural materials in molten salts.* Journal of Nuclear Materials, 2021. **546**: p. 152755.
64. Ding, W., A. Bonk, and T. Bauer, *Corrosion behavior of metallic alloys in molten chloride salts for thermal energy storage in concentrated solar power plants: A review.* Frontiers of Chemical Science and Engineering, 2018. **12**(3): p. 564-576.
65. Zhao, Y. and J. Vidal, *Potential scalability of a cost-effective purification method for MgCl2-Containing salts for next-generation concentrating solar power technologies.* Solar Energy Materials and Solar Cells, 2020. **215**.
66. Ding, W., et al., *Molten chloride salts for next generation CSP plants: Electrolytical salt purification for reducing corrosive impurity level.* Solar Energy Materials and Solar Cells, 2019. **199**: p. 8-15.
67. Fernández, A.G. and L.F. Cabeza, *Corrosion evaluation of eutectic chloride molten salt for new generation of CSP plants. Part 1: Thermal treatment assessment*, in *Journal of Energy Storage*. 2020, Elsevier. p. 101125.
68. Kurley, J.M., et al., *Enabling chloride salts for thermal energy storage: implications of salt purity.* RSC Advances, 2019. **9**(44): p. 25602-25608.
69. Li, H., et al., *Effect of Chloride Impurity on Corrosion Kinetics of Stainless Steels in Molten Solar Salt for CSP Application: Experiments and Modeling.* Oxidation of Metals, 2021. **95**(3): p. 311-332.
70. Kipouros, G.J. and D.R. Sadoway, *A thermochemical analysis of the production of anhydrous MgCl2.* Journal of Light Metals, 2001. **1**(2): p. 111-117.
71. Maricle, D.L. and D.N. Hume, *A new method for preparing hydroxide-free alkali chloride melts*. 1959, Massachusetts Inst. of Tech., Cambridge. Lab. for Nuclear Science: United States.
72. Mortazavi, A., et al., *High-temperature corrosion of a nickel-based alloy in a molten chloride environment – The effect of thermal and chemical purifications.* Solar Energy Materials and Solar Cells, 2022. **236**: p. 111542.
73. Klammer, N., et al., *Method To Determine MgO and MgOHCl in Chloride Molten Salts.* Analytical Chemistry, 2020. **92**(5): p. 3598-3604.

74. Fernández, A.G. and L.F. Cabeza, *Anodic Protection Assessment Using Alumina-Forming Alloys in Chloride Molten Salt for CSP Plants.* Coatings, 2020. **10**(2).
75. Ding, W., et al., *Molten chloride salts for next generation concentrated solar power plants: Mitigation strategies against corrosion of structural materials.* Solar Energy Materials and Solar Cells, 2019. **193**: p. 298-313.
76. Gong, Q., et al., *Molten chloride salt technology for next-generation CSP plants: Compatibility of Fe-based alloys with purified molten MgCl2-KCl-NaCl salt at 700 °C.* Applied Energy, 2022. **324**: p. 119708.
77. Hanson, K., et al., *Effect of excess Mg to control corrosion in molten MgCl2 and KCl eutectic salt mixture.* Corrosion Science, 2022. **194**: p. 109914.
78. Keiser, J.R., J.H. DeVan, and E.J. Lawrence, *Compatibility of molten salts with type 316 stainless steel and lithium.* Journal of Nuclear Materials, 1979. **85-86**: p. 295-298.
79. Ding, W., et al., *Molten chloride salts for next generation concentrated solar power plants: Mitigation strategies against corrosion of structural materials*, in *Solar Energy Materials and Solar Cells*. 2019, Elsevier B.V. p. 298-313.
80. Eliaz, N., G. Shemesh, and R.M. Latanision, *Hot corrosion in gas turbine components.* Engineering Failure Analysis, 2002. **9**(1): p. 31-43.
81. Ahmad, Z., *CHAPTER 12 - CONCRETE CORROSION*, in *Principles of Corrosion Engineering and Corrosion Control*, Z. Ahmad, Editor. 2006, Butterworth-Heinemann: Oxford. p. 609-646.
82. Engelberg, D.L., *2.06 - Intergranular Corrosion*, in *Shreir's Corrosion*, B. Cottis, et al., Editors. 2010, Elsevier: Oxford. p. 810-827.
83. Picard, G.S., T.A. Flament, and B.L. Trémillon, *Acidity and Thermochemical Stability of Molten Sodium Nitrate and Nitrite Mixtures.* Journal of The Electrochemical Society, 1985. **132**(4): p. 863-868.
84. Picard, G.S., H.M. Lefebvre, and B.L. Trémillon, *Thermodynamic Study of Corrosion of Iron in NaNO3 - NaNO2 Mixtures.* Journal of The Electrochemical Society, 1987. **134**(1): p. 52-58.
85. S.H. Goods, R.W.B., M. R. Prairie, J. M. Chavez, *Corrosion of Stainless and Carbon Steels in Molten Mixtures of Industrial Nitrates*. 1994: Sandia National Laboratorie.
86. Goods, S.H. and R.W. Bradshaw, *Corrosion of Stainless Steels and Carbon Steel by Molten Mixtures of Commercial Nitrate Salts.* Journal of Materials Engineering and Performance, 2004. **13**(1): p. 78-87.
87. Bradshaw, R.W. and W.M. Clift, *Effect of chloride content of molten nitrate salt on corrosion of A516 carbon steel*. 2010, Sandia National Laboratories: Albuquerque, New Mexico 87185 and Livermore, California 94550. p. 1–27.
88. Grosu, Y., O. Bondarchuk, and A. Faik, *The effect of humidity, impurities and initial state on the corrosion of carbon and stainless steels in molten HitecXL salt for CSP application.* Solar Energy Materials and Solar Cells, 2018. **174**: p. 34-41.
89. Cheng, W.-J., D.-J. Chen, and C.-J. Wang, *High-temperature corrosion of Cr–Mo steel in molten LiNO3–NaNO3–KNO3 eutectic salt for thermal energy storage.* Solar Energy Materials and Solar Cells, 2015. **132**: p. 563-569.
90. Goods, S.H., et al., *Corrosion of stainless and carbon steels in molten mixtures of industrial nitrates*. 1994, ; Sandia National Lab. (SNL-CA), Livermore, CA (United States). p. 37 p.

91. Bradshaw, R.W. and S.H. Goods, *Corrosion of Alloys and Metals by Molten Nitrates*. 2001, Sandia National Laboratories.
92. Fernández, A.G., et al., *Corrosion of stainless steels and low-Cr steel in molten Ca(NO3)2–NaNO3–KNO3 eutectic salt for direct energy storage in CSP plants.* Solar Energy Materials and Solar Cells, 2015. **141**: p. 7-13.
93. Fernández, A.G., M.I. Lasanta, and F.J. Pérez, *Molten Salt Corrosion of Stainless Steels and Low-Cr Steel in CSP Plants.* Oxidation of Metals, 2012. **78**(5-6): p. 329-348.
94. Kruizenga, A. and D. Gill, *Corrosion of Iron Stainless Steels in Molten Nitrate Salt.* Energy Procedia, 2014. **49**: p. 878-887.
95. Fernández, A.G., et al., *Corrosion of alumina-forming austenitic steel in molten nitrate salts by gravimetric analysis and impedance spectroscopy*, in *Materials and Corrosion*. 2014. p. 267-275.
96. Meißner, T.M., et al., *Improving the corrosion resistance of ferritic-martensitic steels at 600 °C in molten solar salt via diffusion coatings.* Solar Energy Materials and Solar Cells, 2021. **227**.
97. Mohan, G., M.B. Venkataraman, and J. Coventry, *Sensible energy storage options for concentrating solar power plants operating above 600 °C.* Renewable and Sustainable Energy Reviews, 2019. **107**: p. 319-337.
98. Hsu, H., J.H. Devan, and M. Howell, *Solubilities of LiFeO2 and ( Li , K ) 2CrO4 in Molten Alkali Carbonates at 650°C.* Journal of The Electrochemical Society, 1987. **134**: p. 2146-2150.
99. Gleeson, B., *1.09 - Thermodynamics and Theory of External and Internal Oxidation of Alloys*, in *Shreir's Corrosion*, B. Cottis, et al., Editors. 2010, Elsevier: Oxford. p. 180-194.
100. Young, D.J., *Chapter 6 - Alloy Oxidation II: Internal Oxidation*, in *High Temperature Oxidation and Corrosion of Metals (Second Edition)*, D.J. Young, Editor. 2016, Elsevier. p. 261-333.
101. Shores, D.A. and P. Singh. *Department of Chemical Engineering and Materials Science*. in *Proceedings of the Symposium on Molten Carbonate Fuel Cell Technology*. 1984. Electrochemical Society.
102. Yuh, C.-Y., et al., *Status of Carbonate Fuel Cell Materials.* ECS Transactions, 2012. **41**: p. 21-33.
103. Ni, C.S., et al., *Electrochemical impedance studies of the initial-stage corrosion of 310S stainless steel beneath thin film of molten (0.62Li,0.38K)2CO3 at 650°C.* Corrosion Science, 2011. **53**(3): p. 1018-1024.
104. de Miguel, M.T., et al., *Corrosion resistance of HR3C to a carbonate molten salt for energy storage applications in CSP plants.* Solar Energy Materials and Solar Cells, 2016. **157**: p. 966-972.
105. Frangini, S. and S. Loreti, *The role of temperature on the corrosion and passivation of type 310S stainless steel in eutectic (Li + K) carbonate melt*, in *Journal of Power Sources*. 2006. p. 800-804.
106. Gomez-Vidal, J.C., J. Noel, and J. Weber, *Corrosion evaluation of alloys and MCrAlX coatings in molten carbonates for thermal solar applications.* Solar Energy Materials and Solar Cells, 2016. **157**: p. 517-525.
107. Hamdy, E., J. Nockert-Olovsjö, and C. Geers, *Perspectives on selected alloys in contact with eutectic melts for thermal storage: Nitrates, carbonates and chlorides.* Solar Energy, 2021. **224**: p. 1210-1221.
108. Frangini, S., *Corrosion Behavior of AISI 316L Stainless Steel and ODS FeAl Aluminide in Eutectic Li2CO3–K2CO3 Molten Carbonates under Flowing CO2–O2 Gas Mixtures.* Oxidation of Metals, 2000. **53**(1): p. 139-156.

109. Randström, S., C. Lagergren, and P. Capobianco, *Corrosion of anode current collectors in molten carbonate fuel cells.* Journal of Power Sources, 2006. **160**(2): p. 782-788.
110. Fernández, A.G., et al., *Corrosion evaluation of alumina-forming alloys in carbonate molten salt for CSP plants.* Renewable Energy, 2019. **140**: p. 227-233.
111. Zeng, C. and Y. Liu, *A comparative study of the corrosion behavior of three stainless steels in an eutectic (Li, Na, K) 2CO3 melt with and without (Na, K) Cl Additives at 973K in Air*. 2011.
112. Prieto, C., et al., *Carbonate molten salt solar thermal pilot facility: Plant design, commissioning and operation up to 700 °C.* Renewable Energy, 2020. **151**: p. 528-541.
113. Spiegel, M., P. Biedenkopf, and H.-J. Grabke, *Corrosion of iron base alloys and high alloy steels in the Li2CO3-K2CO3 eutectic mixture.* Corrosion Science, 1997. **39**(7): p. 1193-1210.
114. Perez, F., et al., *Hot-corrosion studies of separator plates of AISI-310 stainless steels in molten-carbonate fuel cells.* Oxidation of metals, 2000. **53**(3): p. 375-398.
115. Ahn, S., et al., *Electrochemical analysis on the growth of oxide formed on stainless steels in molten carbonate at 650° C.* international journal of hydrogen energy, 2014. **39**(23): p. 12291-12299.
116. Li, C.-j., et al., *Survey of Properties of Key Single and Mixture Halide Salts for Potential Application as High Temperature Heat Transfer Fluids for Concentrated Solar Thermal Power Systems*. 2014. p. 133-157.
117. Vignarooban, K., et al., *Heat transfer fluids for concentrating solar power systems - A review*, in *Applied Energy*. 2015, Elsevier Ltd. p. 383-396.
118. Guillot, S., et al., *Corrosion effects between molten salts and thermal storage material for concentrated solar power plants*, in *Applied Energy*. 2012. p. 174-181.
119. Wu, Y.-t., et al., *Experimental study on optimized composition of mixed carbonate salt for sensible heat storage in solar thermal power plant.* Solar Energy, 2011. **85**(9): p. 1957-1966.
120. Ding, W., A. Bonk, and T. Bauer, *Molten Chloride Salts for Next Generation CSP Plants : Selection of Promising Chloride Salts & Study on Corrosion of Alloys in Molten Chloride Salts.* 2018.
121. Hamdy, E., J. Nockert-Olovsjö, and C. Geers, *Additional data and experimental setups used for the study on alloys in contact to high temperature eutectic melts for thermal storage* Data in Brief, 2021: p. 107446.
122. *Standard Practice for Preparing, Cleaning, and Evaluating Corrosion Test Specimens*, in *Methods for Cleaning After Testing*. 2017, © ASTM International.
123. Ding, W.J., et al., *Molten chloride salts for next generation CSP plants: Electrolytical salt purification for reducing corrosive impurity level.* Solar Energy Materials and Solar Cells, 2019. **199**: p. 8-15.
124. Fähsing, D., et al., *Corrosion testing of diffusion-coated steel in molten salt for concentrated solar power tower systems*, in *Surface and Coatings Technology*. 2018, Elsevier B.V. p. 46-55.
125. Soleimani Dorcheh, A., R.N. Durham, and M.C. Galetz, *Corrosion behavior of stainless and low-chromium steels and IN625 in molten nitrate salts at 600 °c*, in *Solar Energy Materials and Solar Cells*. 2016, Elsevier. p. 109-116.
126. Gomes, A., et al., *High-temperature corrosion performance of austenitic stainless steels type AISI 316L and AISI 321H, in molten Solar Salt*, in *Solar Energy*. 2019, Elsevier. p. 408-419.
127. Encinas-Sánchez, V., et al., *Electrochemical impedance spectroscopy (EIS): An efficient technique for monitoring corrosion processes in molten salt environments in CSP applications*. Solar Energy Materials and Solar Cells, 2019. **191**: p. 157-163.

128. Nguyen, T.D., J. Zhang, and D.J. Young, *Effects of cerium and manganese on corrosion of Fe–Cr and Fe–Cr–Ni alloys in Ar–20CO2 and Ar–20CO2–20H2O gases at 650°C.* Corrosion Science, 2015. **100**: p. 448-465.
129. Xi, X., C. Kong, and J. Zhang, *Effect of Cyclic Reaction on Corrosion Behavior of Chromium-Containing Alloys in CO2 Gas at 650 °C.* Oxidation of Metals, 2020. **93**(1): p. 131-157.
130. Oskay, C., et al., *Scale Formation and Degradation of Diffusion Coatings Deposited on 9% Cr Steel in Molten Solar Salt*, in *Coatings*. 2019. p. 687.
131. Atkins, P.W., *Chemical principles: the quest for insight*, ed. L. Jones. 2000, New York: W.H. Freeman.
132. Epp, J., *X-ray diffraction (XRD) techniques for materials characterization*, in *Materials characterization using nondestructive evaluation (NDE) methods*. 2016, Elsevier. p. 81-124.
133. Bragg, W.H.S., *X-rays and crystal structure* ed. L.S. Bragg. 1915, London: G. Bell and Sons, Ltd.
134. Kniess, C.T., et al., *Quantitative Determination of the Crystalline Phases of the Ceramic Materials Utilizing the Rietveld Method.* Materials Science Forum, 2010. **660-661**: p. 164-169.
135. Momma, K. and F. Izumi, *VESTA 3 for three-dimensional visualization of crystal, volumetric and morphology data.* Journal of Applied Crystallography, 2011. **44**(6): p. 1272-1276.
136. Lejus, A.-M., *Sur la formation à haute température de spinelles non stoechiométriques et de phases dérivées dans plusieurs systèmes d'oxydes à base d'alumine et dans le système alumine-nitrure d'aluminium*. 1964, Masson et Cie: Paris.
137. Joseph Goldstein, et al., *Scanning Electron Microscopy and X-ray Microanalysis*. 3 ed. Scanning. Vol. 27. 2005, Boston, MA: Springer. XIX, 689.
138. Andersson, J.O., et al., *Thermo-Calc and DICTRA, Computational tools for materials science.* Calphad, 2002. **26**: p. 273-312.
139. Bale, C.W., et al., *FactSage Thermochemical Software and Databases - Recent Developments.* Calphad, 2009. **33**: p. 17.
140. Sequeira, C.A.C., *Corrosion in Molten Salts*, in *High Temperature Corrosion*. 2019. p. 296-324.
141. Fernández, A.G., et al., *Corrosion properties of a ternary nitrate/nitrite molten salt inconcentrated solar technology*, in *Renewable Energy*. 2015. p. 177-183.
142. Sah, S.P., E. Tada, and A. Nishikata, *Corrosion behaviour of austenitic stainless steels in carbonate melt at 923 K under controlled CO2-O2 environment*, in *Corrosion Science*. 2018, Elsevier Ltd. p. 310-317.
143. Grosse, M., *9 - High-temperature oxidation in nuclear reactor systems*, in *Nuclear Corrosion Science and Engineering*, D. Féron, Editor. 2012, Woodhead Publishing. p. 265-300.
144. Encinas-Sánchez, V., et al., *Corrosion resistance of Cr/Ni alloy to a molten carbonate salt at various temperatures for the next generation high-temperature CSP plants.* Solar Energy, 2018. **171**: p. 286-292.
145. Hamdy, E., A. Wagné, and C. Geers, *Evaporated Alkali Carbonate Effect on an Aluminum Diffusion Coated 253MA Vessel after 4000 h Discontinuous Operation—Lessons Learned.* Energies, 2022. **15**(9): p. 3241.
146. Landberg, E., et al., *New alumina-forming steels for future energy production with focus on solar power*. 2016: Jernkontoret, Stockholm.

147. Danek, V., M. Tarniowy, and L. Suski, *Kinetics of the α → γ phase transformation in LiAlO2 under various atmospheres within the 1073–1173 K temperatures range.* Journal of Materials Science, 2004. **39** p. 2429– 2435.
148. Heo, S.J., et al., *Role of Exposure Atmospheres on Particle Coarsening and Phase Transformation of LiAlO2.* Journal of The Electrochemical Society, 2017. **164**(8): p. H5086-H5092.
149. Choi, H.J., et al., *Phase and Microstructural Stability of Electrolyte Matrix Materials for Molten Carbonate Fuel Cells.* Fuel Cells, 2010. **10**(4): p. 613-618.
150. Evans, H.E., D.J. Norfolk, and T. Swan, *Perturbation of parabolic kinetics resulting from the accumulation of stress in protective oxide layers.* Journal of the Electrochemical Society, 1978. **125**(7): p. 1180-1185.
151. Byker, H.J., et al., *Calculation of a phase diagram for the lithium oxide-aluminum oxide (LiO0.5-AlO1.5) system.* The Journal of Physical Chemistry, 1979. **83**(18): p. 2349-2355.
152. Harlow, W., et al., *Thickness-dependent stabilization of tetragonal ZrO2 in oxidized zirconium.* Scripta Materialia, 2018: p. 95-98.
153. Spengler, D.J., et al., *Characterization of Zircaloy-4 corrosion films using microbeam synchrotron radiation.* Journal of Nuclear Materials, 2015. **464**(C): p. 107-118.
154. Hamdy, E., et al., *Differentiation in corrosion performance of alumina forming alloys in alkali carbonate melts.* Corrosion Science, 2021: p. 109857.
155. Lehmann, H.-A. and H. Hesselbarth, *Zur Kenntnis der Lithiumaluminate. I. Über eine neue Modifikation des LiAlO2.* Zeitschrift für anorganische und allgemeine Chemie, 1961. **313**(1-2): p. 117-120.
156. Asokan, V., et al., *The influence of Si on the primary protection of lean FeCrAl model alloys in O2 and O2+H2O at 600 °C—A microstructural investigation.* Corrosion Science, 2021. **179**: p. 109155.
157. Young, D.J., *Chapter 5 - Oxidation of Alloys I: Single Phase Scales*, in *High Temperature Oxidation and Corrosion of Metals (Second Edition)*, D.J. Young, Editor. 2016, Elsevier. p. 193-260.
158. Yoneda, S. and S. Hayashi, *Effect of Cr Content on Microstructure and Growth of External Al2O3 Scale Formed on Fe–Cr–Al Alloys.* Oxidation of Metals, 2022. **97**(1): p. 195-208.
159. Liu, F., *Microstructural investigation of high temperature oxidation of Al2O3-forming and Cr2O3-forming steels - The influence of water vapour*, in *Applied Physics, Microscopy and Microanalysis*. 2008, Chalmers University of Technology: Gothenburg.
160. Kovarik, L., M. Bowden, and J. Szanyi, *High temperature transition aluminas in δ-Al2O3/θ-Al2O3 stability range: Review.* Journal of Catalysis, 2021. **393**: p. 357-368.
161. Berthomé, G., et al., *Temperature dependence of metastable alumina formation during thermal oxidation of FeCrAl foils.* Materials and Corrosion, 2005. **56**(6): p. 389-392.